Electron Beam Dynamics in a Proton-driven Plasma Wakefield

Barnaby M. Williamson

MANCHESTER
1824
The University of Manchester

A thesis submitted to the University of Manchester for the degree of Doctor of Philosophy in the Faculty of Science and Engineering

Doctoral Supervisor: Dr. Guoxing Xia

2020

School of Physics and Astronomy

University of Manchester

Oxford Road, Manchester, M13 9PL

Contents

List of Figures

List of Tables

Abstract

The scale of frontier particle physics experiments is expected to go on increasing, precipitated by a physics case that demands ever higher energy collisions of more particles, more frequently. All working colliders in particle physics today operate on the basis of radiofrequency (RF) acceleration in metallic cavities. However, fundamental limits on the achievable accelerating gradient per cavity mean that to obtain higher energy gain requires longer accelerators, and larger and more costly beam facilities.

Electrostatic density waves driven in plasma can accommodate accelerating electric fields that are orders of magnitude greater than those found in metallic cavities, offering a route to lower-cost beam facilities. Experimentally, plasma wakefield accelerators have been demonstrated as a compact source of high energy electrons with features that could be well suited to specific applications. One such scheme is the proton-driven plasma wakefield accelerator, where a highly relativistic proton beam sustains an accelerating field over many metres of plasma, owing to the substantial energy it carries. Because of this property, an accelerated witness beam may reach the energy frontier in a single plasma stage, decreasing the complexity of a plasma-based collider. The reproducibility and quality of the accelerated witness beam are key for the successful operation of any collider, and for the most part these considerations still remain to be addressed for plasma-based accelerators. This thesis makes use of extensive particle-in-cell simulations to investigate those aspects of the

proton-driven scheme on which achievable beam quality depends and gives guidance for future proton-driven plasma wakefield acceleration experiments, which could prove significant for the development of plasma-based electron-positron colliders.

The first simulation study presented in this thesis demonstrates that an LWFA can provide short duration, narrow, and low emittance electron beams at injection, which also have a sufficient energy and charge, to facilitate beam quality preservation during proton-driven plasma wakefield acceleration. Significantly, the required duration and transverse beam size are not readily achievable with conventional RF photoinjectors. The second study characterises the betatron emission from an electron beam accelerated in a proton-driven plasma wakefield under a range of experimental conditions. It demonstrates that a significant quantity of detectable photons are emitted by the accelerated electron beam into high angles away from the proton driver, therefore enabling a non-intercepting emittance measurement. Such a measurement will allow the characterisation of electron beam quality inside the plasma wakefield itself, a unique tool to diagnose the evolution of electron beam emittance within a single accelerating stage. Finally, long-range simulations show the impact of radiation reaction on proton-driven plasma wakefield acceleration, demonstrating the point at which radiative damping of the electron beam emittance becomes significant. Radiative damping of electron beams ultimately defines the long term dynamics of plasma wakefield-accelerated beams, and may be exploited to reach novel luminosity regimes at the interaction point of a plasma-based collider. The emittance preservation of a radiating positron beam, accelerated in a nonlinear electron-driven plasma wakefield, is also shown, which could simplify the design of a plasma-based electron-positron collider.

Declaration

The work contained within this thesis was undertaken between October 2016 and March 2020 at the University of Manchester, while the author was a doctoral student under the supervision of Dr. Guoxing Xia. No portion of the work referred to in the thesis has been submitted in support of an application for another degree or qualification of this or any other university or other institute of learning.

Copyright Statement

i The author of this thesis (including any appendices and/or schedules to this thesis) owns certain copyright or related rights in it (the "Copyright") and s/he has given The University of Manchester certain rights to use such Copyright, including for administrative purposes.

ii Copies of this thesis, either in full or in extracts and whether in hard or electronic copy, may be made only in accordance with the Copyright, Designs and Patents Act 1988 (as amended) and regulations issued under it or, where appropriate, in accordance with licensing agreements which the University has from time to time. This page must form part of any such copies made.

iii The ownership of certain Copyright, patents, designs, trademarks and other intellectual property (the "Intellectual Property") and any reproductions of copyright works in the thesis, for example graphs and tables ("Reproductions"), which may be described in this thesis, may not be owned by the author and may be owned by third parties. Such Intellectual Property and Reproductions cannot and must not be made available for use without the prior written permission of the owner(s) of the relevant Intellectual Property and/or Reproductions.

iv Further information on the conditions under which disclosure, publication and commercialisation of this thesis, the Copyright and any Intellectual

Property and / or Reproductions described in it may take place is available in the University IP Policy, in any relevant Thesis restriction declarations deposited in the University Library, The University Library's regulations and in The University's policy on Presentation of Theses.

Acknowledgements

A PhD is a formative time, not least because you meet so many people along the way. I would like to thank Guoxing Xia for the opportunities and supervision he has given me throughout my studies. In Manchester and the Cockcroft Institute I found a great community of students and mentors, including Mohammad Islam, Yong Ma, Yangmei Li, and Tom Pacey, and I would particularly like to thank Öznur Mete-Apsimon for introducing me to so much in accelerator science. Also at the Cockcroft Institute, I would like to thank my MPhys supervisor Andy Wolski, whose expertise in beam dynamics helped and engaged me well into my graduate studies.

Thanks also goes to Andreas Döpp and Stefan Karsch at LMU Munich for their help and expertise in laser-plasma acceleration, and I would like to thank Edda Gschwendtner, Allen Caldwell, Patric Muggli, and Steffen Döbert for their support, guidance and many great opportunities to work on the AWAKE experiment.

Special thanks goes to Spencer Gessner and Alexey Petrenko, who put up with innumerable queries from me, and from whom I have gained invaluable experience that will stay with me for a long time. I'd also like to thank John Farmer for many helpful discussions, i.e. lessons, in computational physics, as well as Josh Moody, Kevin Pepitone, Marlene Turner, and Alessandro Curcio. AWAKE sits within the broader context of a national laboratory and I was

fortunate to meet people from many parts of it, but from the Beam Instrumentation section especially I would like to thank Stefano Mazzoni and Ishkhan Gorgisyan for their help in pursuing many issues with the pepper-pot. This work would not count without the tireless dedication of both the experimental team and the students at AWAKE, a group of people I feel lucky to have met. So thank you to them, above all for their friendship, during my two years at CERN.

For seeing me through this and many other endeavors, to my parents thank you, always.

Publications and Contributions

- Kim, S.-Y.et al. Commissioning of the electron injector for the awake experiment. *Nuclear Instruments and Methods in Physics Research Section A: Accelerators, Spectrometers, Detectors and Associated Equipment* **953**, 163194 (2020)

- Apsimon, O., Williamson, B. & Xia, G. A numerical approach to designing a versatile pepper-pot mask for emittance measurement. *Nuclear Instruments and Methods in Physics Research Section A: Accelerators,Spectrometers, Detectors and Associated Equipment* **943**, 162485 (2019)

- Gschwendtner, E. et al. Proton-driven plasma wakefield acceleration in awake. *Philosophical Transactions of the Royal Society A: Mathematical,Physical and Engineering Sciences* **377**, 20180418 (2019).

- Turner, M. et al. (The AWAKE Collaboration) Experimental observation of plasma wakefield growth driven by the seeded self-modulation of a proton bunch. *Phys. Rev. Lett.* **122**, 054801 (2019).

- Adli, E.et al. (The AWAKE Collaboration) Experimental observation of proton bunch modulation in a plasma at varying plasma densities. *Phys. Rev. Lett.* **122**, 054802 (2019).

- Jakobsson, O. et al. Tailored plasma-density profiles for enhanced en-

ergy extraction in passive plasma beam dumps. *Plasma Physics and Controlled Fusion* **61**, 124002 (2019)

- Adli, E. et al. (The AWAKE Collaboration) Acceleration of electrons in the plasma wakefield of a proton bunch. *Nature* **561**, 363–367 (2018)

- Williamson, B., Xia, G., Döbert, S., Karsch, S. & Muggli, P. Simulation-study of an lwfa-based electron injector for awake run 2. *Nuclear Instruments and Methods in Physics Research Section A: Accelerators, Spectrometers, Detectors and Associated Equipment* **909**, 126 – 129 (2018).

- Pepitone, K. et al. The electron accelerators for the awake experiment atcern - baseline and future developments. *Nuclear Instruments and Methods in Physics Research Section A: Accelerators, Spectrometers, Detectors and Associated Equipment* **909**, 102 – 106 (2018)

- Muggli, P. et al. AWAKE readiness for the study of the seeded self-modulation of a 400 GeV proton bunch. *Plasma Physics and Controlled Fusion* **60**, 014046 (2017).

- Williamson, B. et al. Betatron Radiation Diagnostics for AWAKE Run 2. *Nuclear Instruments and Methods in Physics Research Section A: Accelerators, Spectrometers, Detectors and Associated Equipment*, **971**, 164076 (2020).

The AWAKE Experiment is made possible by the collaborative efforts of a large number of people. While most of the work presented in this thesis looks to the future applications of proton-driven plasma wakefield acceleration, I am glad for the opportunity to have made contributions to the AWAKE experiment itself. I was personally involved in the installation, commissioning and operation of the pepper-pot emittance diagnostic, and developed a graphical user interface for the online analysis of electron beam emittance.

List of Symbols

Mathematical constants such as π and Euler's number e take their usual values. Values for the fundamental physical constants are taken from the U.S. National Institute of Standards and Technology (NIST).

Table 1: List of Constants

Symbol	Quantity	Value	Unit
e	Elementary charge	1.60×10^{-19}	C
m_e	Electron mass	9.11×10^{-31}	kg
$m_e c^2$	Electron mass energy eq.	0.511	MeV
m_p	Proton mass	1.67×10^{-27}	kg
$m_p c^2$	Proton mass energy eq.	938	MeV
α	Fine–structure constant	7.30×10^{-3}	–
ε_0	Free space permittivity	8.85×10^{-12}	Fm^{-1}
μ_0	Free space permeability	$4\pi \times 10^{-7}$	Hm^{-1}
$\hbar$	Reduced Planck constant	1.05×10^{-34}	J s
c	Vacuum speed of light	$299\,792\,458$	ms^{-1}
k_B	Boltzmann constant	1.38×10^{-23}	JK^{-1}

Table 2: List of Variables

Symbol	Quantity	Unit
q	Electric charge	C
Q	Total charge	C
ρ	Charge density	Cm^{-3}
I	Electric current	A
$\vec{J}$	Current density	Am^{-2}
σ	Conductivity	Sm^{-1}
$\vec{E}$	Electric field	Am^{-2}
$\vec{D}$	Electric displacement	Cm^{-2}
ϕ	Electric scalar potential	V
$\vec{B}$	Magnetic field	T
$\vec{H}$	Magnetic intensity	Am^{-1}
$\vec{A}$	Magnetic vector potential	$\mathrm{T\,m}$
β	Relativistic normalised velocity	–
γ	Relativisitic Lorentz factor	–
λ_D	Debye Length	m
n_e	Electron number density	cm^{-3}
ω_p	Plasma frequency	rads^{-1}
k_p	Plasma wavenumber	m^{-1}
λ_p	Plasma wavelength	m
ω_β	Betatron frequency	rads^{-1}
k_β	Betatron wavenumber	m^{-1}
λ_β	Betatron wavelength	m
K	Ion focusing constant	m^{-3}
α_β	Betatron strength parameter	–
T_e	Plasma electron temperature	K
Z	Atomic number	–

Chapter 1

Introduction

1.1 Changing Accelerating Media

Particle accelerators are widespread scientific tools that drive experimental progress in a broad range of disciplines. They operate at the forefront of high energy physics, for example at the Large Hadron Collider [1] (LHC), and as high brilliance x-ray sources for the radiography of archaeological materials [2]. Functionally, accelerators play an increasingly present role in society with application in industrial processes and scanning. They are invaluable to diagnostic medicine, and provide new possibilities in therapeutic oncology: selective targeting of cancerous tissue with the unique Bragg-peak energy deposition of a proton beam can spare more of the surrounding healthy tissue [3] – a less invasive treatment that provides better outcomes for the people who receive it.

Conventional accelerators use electric fields in conducting metallic cavities to accelerate charged particles. The electric field oscillates at radio frequencies timed such that a passing particle only sees an accelerating field within each cavity and continually gains energy. Radiofrequency (RF) acceleration is a ma-

ture and successful technology that forms the basis of all working accelerators today, including those delivering beams for high energy physics experiments at the European Organisation for Nuclear Research (CERN). These experiments place certain requirements on the accelerator systems that drive them, such as a high beam luminosity to increase the number of particle collisions and the chance of observing rare processes, and accelerators are carefully designed to meet them. Electron-positron (e^-e^+) colliders are attractive experimental machines as leptons are fundamental; most of the collision energy goes into producing new particles, and interactions of interest are more straightforward to analyse. Circular e^-e^+ accelerators, such as the Large Electron-Positron Collider [4] (LEP), suffer from significant synchrotron radiation losses as the beam is carried around the machine. The circumference of LEP meant it became synchrotron radiation dominated and less practical to run above per-beam energies of $\sim100\,\mathrm{GeV}$ [5]. To reach higher energies would require increasing the radius, as the energy loss per turn scales as $\Delta E \propto E^4/R$ where E is the beam energy and R the machine radius. Consequently linear e^-e^+ colliders such as the Compact Linear Collider [6] (CLIC), which do not suffer from synchrotron radiation loss, are a promising option for the next generation of experiments in particle physics.

The maximum electric field gradient in metallic structure accelerators is, however, limited. Ultimately this is due to RF breakdown [7], a rapid discharge of the stored energy in the accelerating electric fields onto the cavity walls that liberates material, and destroys the ultra-high vacuum environment necessary in an accelerator. The gradient at which breakdown occurs is proportional to the RF frequency, and may be raised with shorter wavelength accelerating fields. Ever smaller metallic structures are therefore required, which soon reach the limits of manufacturing tolerance, and as a result only limited gains in accelerating gradient are possible. The threshold for RF breakdown may also be increased by operating with a lower beam current, the quantity of charge

Figure 1.1: The potential locations of CLIC and FCC, with respect to the LHC. The CLIC 3 TeV configuration would be 50 kilometres long. Map produced with Tilemill (https://tilemill-project.github.io/tilemill/)

per unit length of beam, but this must be weighed against the luminosity requirements of the machine. RF breakdown, and in practice other effects such as dark current trapping of electrons, ultimately lead to a maximum accelerating gradient of $\sim 100\,\mathrm{MVm^{-1}}$ for the highest frequency RF cavities, operated in the X-band or up to $12\,\mathrm{GHz}$ range, which have been developed for CLIC. Consequently linear colliders using RF systems and operating with the GeV-TeV beam energies for frontier energy particle physics experiments must be tens of kilometres in extent.

Figure 1.1 gives an indication of the scale of CLIC, with respect to existing beam facilities at CERN. Hadron machines such as the Future Circular Collider [8] (FCC), also foreseen to be built at CERN, suffer significantly less from synchrotron power loss, but are instead limited by the magnetic field strengths necessary to maintain the design orbit. The machine radius R can be increased to relax the requirement on bending dipole field strength, down towards the

technical limits of contemporary magnet design, and thereby raising the maximum attainable beam energy with respect to the LHC. Such a trade-off does however result in a similarly challenging 100 km circumference for the FCC. While capable of producing high quality particle beams that are desirable and well suited to many physics objectives, RF-based metallic cavity accelerators may place prohibitive requirements on the size and cost of high energy particle physics experiments of the future.

A plasma is a state of matter in which enough electrons have been ionised from their parent atoms to result in a gas with quasi-neutral electric charge that consists of electrons, ions and neutral atoms. Under the influence of high intensity electric fields, a charged-separated plasma can sustain extremely high field gradients in electrostatic density waves that propagate close to the speed of light. As such they can be used to accelerate particles to relativistic energies over very short distances. Plasma-based accelerators have the potential to succeed conventional RF-based accelerators in applications where high gradients are advantageous, such as linear colliders.

The principle of accelerating particles in the electromagnetic field of a plasma wave was first described in 1956 [9], but was not realised experimentally until the 1980s. Accelerating structures within plasma are classified by the method used to drive an electrostatic density wave and produce the resulting electromagnetic field or wakefield. A plasma wakefield is driven either by a high intensity laser pulse [10], or high energy particle beam [11], commonly initialised as LWFA and PWFA respectively. However it is formed, a plasma wakefield may trap and accelerate a bunch of witness particles if they lie in the appropriate wakefield phase. Peak accelerating fields of $52\,\mathrm{GVm^{-1}}$ have been demonstrated in a metre-scale plasma [12] and could reach as high as $82\,\mathrm{GVm^{-1}}$ [13] in the beam-driven case. Laser-driven experiments have seen fields in excess of $200\,\mathrm{GVm^{-1}}$ [14], albeit over a limited distance. Experimental

LWFAs have benefited from advances in compact laser technology over the last four decades, which improved significantly with the development of chirped-pulse amplification of laser beams [15]. This has made the study of intense laser-plasma interaction available to many research groups around the world. Conversely, PWFAs often rely on large-scale conventional accelerator facilities to provide high energy particle beam drivers, such as the Stanford Linear Accelerator Center (SLAC). Different particle species have been utilised for PWFA drivers, each with their own set of benefits and challenges in the context of demonstrating a successful plasma wakefield accelerator.

This thesis is concerned with the physics of electron beams accelerated in a proton beam-driven plasma wakefield, introduced in the following section, however the broader landscape of laser and beam-driven concepts is discussed in sections 2.3 and 2.4 to give context to the proton-driven scheme. Because plasma is a medium capable of hosting accelerating gradients that are orders of magnitude greater than those in metallic cavities, it could provide a significant reduction in the size and cost of colliders used for particle physics. Plasma-based e^-e^+ colliders driven by lasers or particle beams have been investigated, but they raise issues of wall-plug-to-beam energy efficiency, of susceptibility to transverse instabilities that can spoil beam quality, and the lack of an equivalent source of high energy positrons [16, 17]. A figure of merit that summarises the importance of beam quality and reproducibility is the achievable luminosity $\mathcal{L}$ of two particle beams colliding head-on, shown in equation (1.1) [18]:

$$\mathcal{L} = \frac{N_1 N_2 \nu n_b}{4\pi \sigma_x \sigma_y}, \tag{1.1}$$

where N_1 and N_2 are the populations of two bi-Gaussian bunches of equal transverse root mean square (r.m.s.) beam size σ_x and σ_y; ν is the circulating frequency and n_b the number of bunches in one beam. The event rate for a particular process is $dR/dt = \mathcal{L}\cdot\sigma_p$, where σ_p is the production cross-section for

that process. Luminosity therefore characterises the total number of collisions per unit area per unit time, with units of $cm^{-2}s^{-1}$. Plasma-accelerated beams typically have µm-scale transverse size, inherited from the scale of plasma wakefield structures, and carry $\sim$10-500 pC of charge. Dense beams accelerated in a plasma wakefield make for high instantaneous luminosity but are often associated with lower beam quality and reproducibility when compared to RF-accelerated beams – qualities that are vital for beam transport and overall collider performance. For example, a modern RF accelerator may produce beams with relative energy spread on the order of 0.1%, while an LWFA electron beam can typically have 10%, or 1% at best [19]. Such differences aside, it is the revolution frequency ν or equivalently the repetition rate of a linear plasma-based accelerator that is in stark contrast with conventional technology. At peak intensity, the LHC delivers a beam to the interaction point every 25 ns, i.e. with a peak circulating frequency $\nu = 40$ MHz; plasma accelerators have a maximum demonstrated beam repetition rate of 10 Hz [20], or 1 kHz [21] with an electron energy ~ 1 MeV, for the beam and laser-driven cases respectively.

Infrequent, highly energetic and high intensity collisions may be sufficient to probe new physics in specific cases [22], but would remain inadequate for general-purpose discovery colliders. Practically, wall-plug efficiency of plasma accelerators is limited both by laser technology and the restricted transfer of energy from driver to witness in the laser and beam-driven cases respectively [16, 23], and these must be addressed in order to reach parity of efficiency with respect to RF-based accelerators. Despite the above challenges, plasma is an accelerating medium that offers a long-term solution for many accelerator applications, and consequently plasma-based acceleration is an active and rapidly developing field of research.

1.2 Proton-driven Plasma Wakefield Acceleration

1.2.1 The AWAKE Experiment Run 1

The advanced proton–driven plasma wakefield acceleration experiment (AWAKE) [24, 25, 26] is a beam-driven plasma wakefield accelerator at CERN (see figure 1.2). It is the world's first to use protons to drive a wakefield in plasma, and has demonstrated the acceleration of an injected bunch of electrons [27].
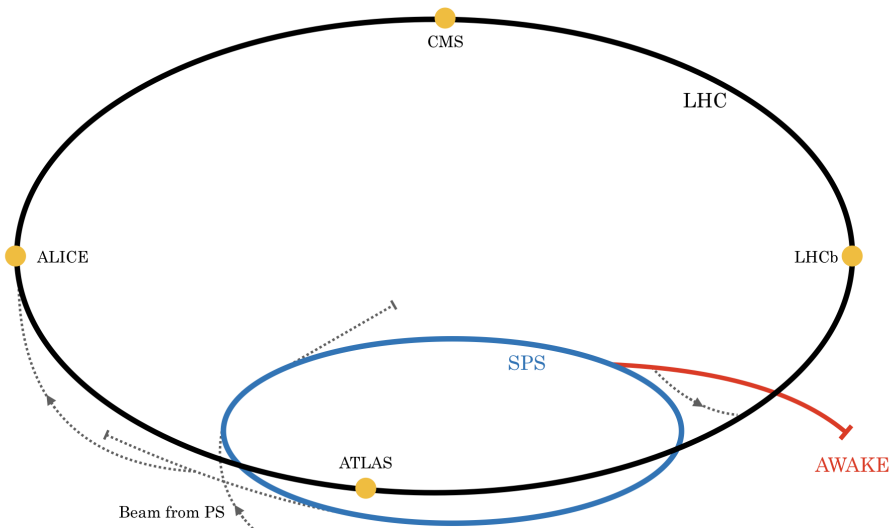
Figure 1.2: The CERN accelerator complex showing the location of the AWAKE experiment, previously occupied by the CNGS experiment, which concluded in 2012.

A proton driver offers significant practical advantages for a plasma-based accelerator used in particle physics experiments. Due to their relatively high mass, protons can propagate for long distances without losing much of their energy to interaction with the plasma and can therefore carry electrons to the energy frontier in a single stage of acceleration [28]. In contrast, an electron-driven PWFA would require staging of multiple plasma cells as the driver energy is depleted more readily. Using the proton-driven scheme the AWAKE

experiment ultimately aims to demonstrate GVm^{-1} acceleration gradients, preserve the beam quality of electron bunches as they are accelerated to higher energies, and inform the design of future plasma-based accelerators [24].

In the experiment, a $400\,GeV$ proton bunch from the CERN Super Proton Synchrotron (SPS), containing $\sim 3 \times 10^{11}$ protons, propagates in a laser–ionised rubidium (Rb) plasma of electron number density $n_e = 7 \times 10^{14}\,cm^{-3}$. The vapour source is comprised of a $10\,m$-long cell with heated flasks at either end to supply Rb vapour up to a maximum density of $n_e = 1 \times 10^{15}\,cm^{-3}$, from which the plasma is generated. A vapour density gradient may be introduced with differential heating in the flasks to produce a linear slope. The gradient was measured to high precision using white light interferometry [29], confirming the high temperature and vapour density uniformity ($< 0.2\,\%$), achieved throughout the cell with a fluid heat exchanger that surrounds it [30].

To resonantly generate a wakefield and maximise the efficiency of energy transfer to the witness bunch, the drive bunch must at least be on the order of a plasma wavelength [28]. This corresponds to around $1.3\,mm$ for $n_e = 7 \times 10^{14}\,cm^{-3}$, whereas proton bunches provided by the SPS have an r.m.s. bunch length of $\sigma_z \sim 7\,cm$. In order to reduce σ_z using currently available longitudinal bunch compression methods would require a greater distance than is available in the transfer line between the SPS and the AWAKE experimental cavern. A method is therefore required to modulate the proton bunch to provide efficient acceleration of witness electrons.

The self-modulation instability [31, 32, 33] (SMI) was proposed to achieve this, and demonstration of this mechanism was one goal of the first phase of the experiment, AWAKE Run 1. A layout is shown in figure 1.3. The $4\,TW$ ionising laser pulse (central wavelength $780\,nm$) [34] is transported from an adjacent laser room and co-propagates with the longitudinal centre of the proton bunch, which corresponds to the maximum intensity of the proton beam.
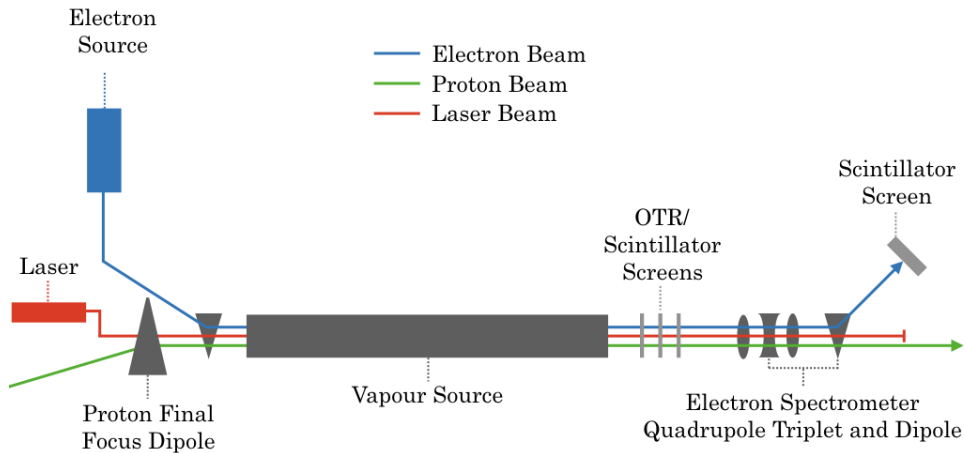
Figure 1.3: AWAKE Run 1. The vapour-ionising laser pulse co-propagates with the proton beam to generate the plasma and seed the SMI. Electrons are externally injected and accelerated in the proton-driven wakefield, and subsequently recorded at the electron energy spectrometer.

As the plasma is created from the Rb vapour at this point newly born plasma electrons observe a sharp rise from zero to the maximum proton beam current, which seeds the SMI. Seeded self-modulation [25] (SSM) of the proton driver and the resulting wakefield growth was successfully observed and characterised [35, 36, 37]. An optical transition radiation (OTR) streak camera is used to measure the structure of the modulated proton beam in space and time [38], and scintillator screens measure the transverse distribution of the proton beam at two locations downstream from the vapour source. The time structure that the proton beam was observed to have on exiting the plasma was shown to be due to axisymmetric periodic defocusing, the strength of which increased with distance from the proton beam centroid, where the plasma is generated; the transverse defocusing wakefield amplitude reached over $300\,\mathrm{MVm^{-1}}$ [36]. Seeding ensures that the proton beam modulates with a stable and reproducible phase [39] and suppresses the Hosing instability [40], which is non-axisymmetric and can compete with the SMI. Seeding may also be achieved

with a short-duration electron beam [41]. Following studies of the SSM mechanism, the remainder of AWAKE Run 1 focused on the acceleration of an externally injected electron beam. To generate and inject the witness electron beam used in Run 1 experiments a separate accelerator system adjacent to the main AWAKE beamline is used, which can be seen in figure 1.4.
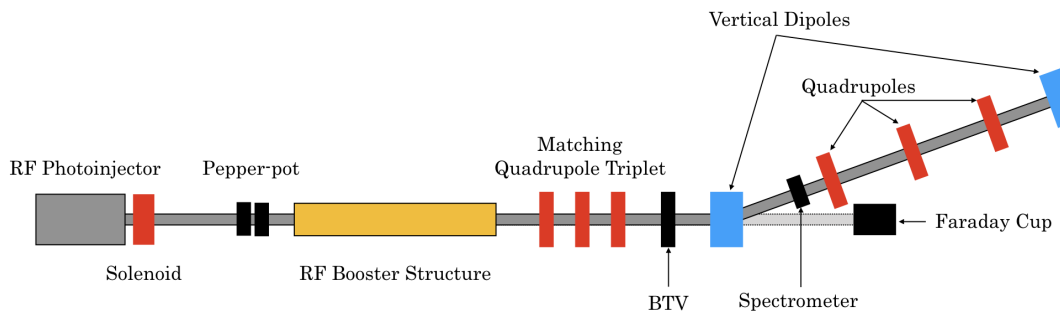
Figure 1.4: AWAKE Run 1 Electron Source, consisting of an S-band RF photoinjector and booster, beam diagnostics and transfer line to the main AWAKE beamline. Only the vertical section of the transfer line is shown.

The electron source [42, 43] consists of an RF photoinjector, beam diagnostics and an RF travelling-wave linear accelerator structure [44]. The photoinjector is comprised of a Cs_2Te cathode ($QE \simeq 1\%$) illuminated by a 262 nm laser (a frequency-tripled derivative of the main ionisation laser), with an optical delay line to produce the desired time structure of the resulting electron beams, and an RF gun which captures and accelerates electrons to 5.5 MeV. The travelling-wave structure serves as an energy booster to achieve a maximum electron beam energy of 20 MeV with an energy spread of 0.5 %. Both RF accelerators are operated at 3 GHz S-band frequency. The diagnosis and control of the electron beam was provided by a number of additional components. A pepper-pot [45] was used to measure the space-charge dominated emittance of the electron beam, and a downstream quadrupole triplet, primarily used to match the electron beam to the transfer line between the electron source and

the rest of the experiment, facilitated quadrupole scans for a second emittance measurement at an imaging screen (BTV) after the booster structure. A description of the pepper-pot emittance measurement technique and the data acquisition software developed for AWAKE is given in the next section. A Faraday cup enabled a measurement of the beam charge, which was used to calibrate the charge for a given photocathode laser aperture size, and a spectrometer measured the energy of the electron beam after acceleration in the booster structure. Typical beam parameters are shown in table 1.1.

Table 1.1: AWAKE Electron Source Beam Parameters in Run 1 [43]

Beam Property	Symbol	Value in Run 1
Beam Energy	E	16-20 MeV
Rel. Energy Spread, r.m.s.	$\Delta E/E$	0.5 %
Bunch Duration, r.m.s.	σ_z	1-4 ps
Bunch Transverse Size, r.m.s.	σ_r	0.25 mm
Normalised Emittance, r.m.s.	ε_n	2 mm mrad
Charge per Bunch	Q	0.14-0.65 nC

A series of vertical and horizontal dipoles transported the electron beam from the electron source to the main proton beamline. Control over the time synchronisation between the ionisation laser, proton driver and witness electron beams enabled some electrons to sample the accelerating phase of the proton-driven wakefield, which were subsequently detected by the electron energy spectrometer [46]. A beam charge of $\sim$650 pC was injected, a fraction of which was captured and accelerated up to a maximum peak energy of 2 GeV in a plasma of density $n_e = 6.6 \times 10^{14}$ cm^{-3} [27].

The peak energy gain could be increased by implementing a plasma density gradient, the slope of which was chosen to maximise the energy gain for a given plasma density. Stable and reliable acceleration to approximately 600 MeV

over nearly 200 events was also demonstrated in a plasma density of $n_e = 1.8 \times 10^{14}\,\mathrm{cm}^{-3}$ with no density gradient [27]. This successful demonstration of electron acceleration in a proton-driven wakefield concluded experiments in Run 1.

1.2.2   The AWAKE Experiment Run 2

The goal of Run 2, which is foreseen to start after LHC long shutdown 2, is to preserve the beam quality throughout the acceleration process. Two important figures of merit for beam quality, absolute energy spread ΔE and normalised emittance ε_n, are minimised and preserved respectively through different mechanisms: the product of bunch charge Q and duration σ_z, the beam current I, must be sufficient to result in a uniform accelerating field along the bunch and a roughly equal energy gain for every constituent electron, thereby keeping $\Delta E \sim$ constant; to preserve ε_n, the beam size must be matched to the plasma density for a given beam energy.

A set of electron beam parameters to meet these criteria and facilitate the optimisation of beam quality over a 10 m acceleration distance have been determined [47], and are summarised in table 1.2. This represents a significant change from Run 1 parameters and beam quality optimisation therefore requires an upgraded electron source, particularly with respect to E, σ_z and σ_r. Meeting these requirements within the space available to the electron injector beamline is challenging [48]. A number of possible solutions are being investigated [49], from X-band RF-accelerators [50] to the use of an LWFA [51].

Modern LWFAs can readily satisfy the bunch length and energy requirements of the Run 2 electron injector system, in a compact design. The plasma source will be modified in Run 2 to consist of separate vapour cells, one for pre-modulating the proton bunch, the other to accelerate an injected elec-

tron bunch, with the possibility for injecting the electron beam between them. Furthermore, new diagnostics after the acceleration stage will be necessary to measure and optimise beam emittance in order to correlate it with the method of injection into the proton-driven wakefield. Betatron radiation spectroscopy is a non-intercepting method to reconstruct the transverse trace space of electron beams in ion channels [52] that could meet the needs for Run 2. The AWAKE experiment aims to inform a future plasma-based linear accelerator for a high energy physics collider. Demonstrating beam quality preservation and understanding beam dynamics in the proton-driven wakefield over long-term acceleration are vital steps in realising this goal [26].

Table 1.2: Possible AWAKE Electron Source Beam Parameters in Run 2 [47]

Beam Property	Symbol	Value in Run 1
Beam Energy	E	$217\,\mathrm{MeV}$
Rel. Energy Spread, r.m.s.	$\Delta E/E$	$1\,\%$
Bunch Duration, r.m.s.	σ_z	$0.2\,\mathrm{ps}$
Bunch Transverse Size, r.m.s.	σ_r	$0.005\,\mathrm{mm}$
Normalised Emittance, r.m.s.	ε_n	$2\,\mathrm{mm\,mrad}$
Charge per Bunch	Q	$0.1\,\mathrm{nC}$

1.2.3 Pepper-pot Emittance Measurement

The pepper-pot was designed [45] prior Run 1 to measure the beam emittance after the electron source RF photoinjector. The pepper-pot camera and screen were used frequently to measure the beam size of the electrons after acceleration in the RF photoinjector, and during general set-up for injection experiments. In this section the motivation and methodology for an emittance measurement using a pepper-pot are explained. The technical components, data acquisition, and data analysis implemented for the pepper-pot system on the AWAKE electron source are described.

A photoinjector generates high charge electron beams at low energy, which are therefore space-charge dominated. Focusing solenoid magnets typically provide space-charge compensation. The transverse r.m.s. beam size σ_r evolves in the paraxial limit ($\sigma' << 1$) according to the envelope equation [53]

$$\sigma_r'' + \sigma_r' \left(\frac{\gamma'}{\beta^2 \gamma} \right) + K_r \sigma_r - \frac{\kappa_s}{\sigma_r \beta^3 \gamma^3} - \frac{\varepsilon_n^2}{\sigma_r^3 \beta^2 \gamma^2} = 0, \qquad (1.2)$$

where γ is the mean beam relativistic Lorentz factor, β is the mean beam velocity normalised to c, K_r is the focusing strength due to an external force, e.g. the solenoid field, κ_s is the beam perveance, proportional to beam current, and superscript prime ($'$) indicates derivatives with respect to time. The divergence of an electron beam emerging from a photoinjector is therefore described by a combination of the space-charge and emittance defocusing terms. In order to suppress the space-charge contribution, and isolate the emittance contribution to be measured, a mask of slits, made of a material with high atomic number Z, can be used to divide an incoming beam into collimated beamlets.

The measured divergence of the beamlets emerging from the mask will then principally be associated with the emittance of the incoming beam, however some space-charge contribution will always remain. Since the total number of particles $N = n_1 + n_2 + ... n_j$ emerging from the mask in j beamlets are a sub-set of the total number of particles in the incoming beam M, i.e. $N < M$, the emittance of the particles that comprise the beamlets is an estimate for the total beam emittance. The one-dimensional geometric emittance of the sub-set N can be calculated from the weighted spot intensity n_j, r.m.s. spot size σ_j, and mean spot position $\langle X_j \rangle$ of each beamlet as measured on a screen, given a drift of length L from a mask slit with position x_j, as shown in figure 1.5.
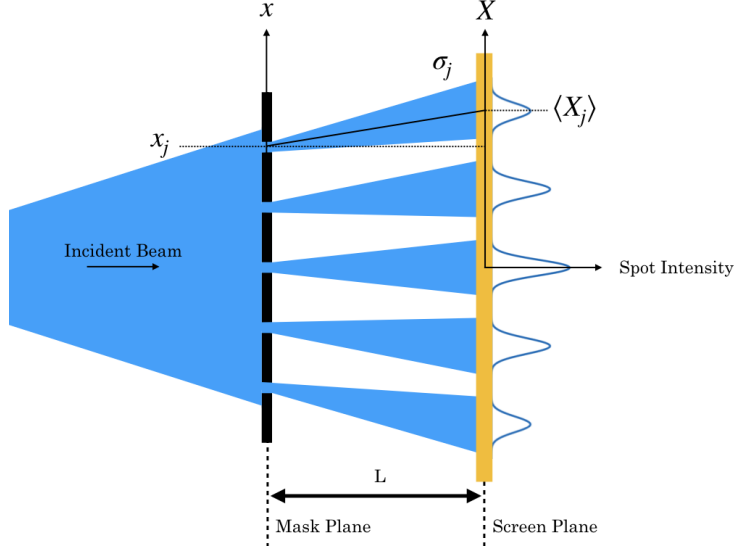
Figure 1.5: A high-Z mask collimates an incoming beam of particles into beamlets. The drift length L must be large enough to provide a good spatial resolution, but remain small enough to avoid re-introducing space-charge defocusing.

The geometric emittance is calculated as $\varepsilon_x = \sqrt{\langle x^2 \rangle \langle x'^2 \rangle - \langle xx' \rangle^2}$ with [54]

$$\langle x^2 \rangle = \frac{1}{N} \sum_{j=1} n_j (x_j - \langle x \rangle)^2, \tag{1.3}$$

$$\langle x'^2 \rangle = \frac{1}{N} \sum_{j=1} \left[n_j \sigma_{x'_j}^2 + n_j (\langle x'_j \rangle - \langle x' \rangle)^2 \right], \tag{1.4}$$

$$\langle xx' \rangle = \frac{1}{N} \left(\sum_{j=1} n_j x_j \langle x'_j \rangle - N \langle x \rangle \langle x' \rangle \right), \tag{1.5}$$

where $\langle x \rangle = 1/N \sum_{j=1} n_j x_j$ is the mean position of all the beamlets, $\langle x' \rangle = 1/N \sum_{j=1} n_j \langle x'_j \rangle$ is the mean divergence of all the beamlets, $\langle x'_j \rangle = (\langle X_j \rangle - x_j)/L$ is the mean divergence of the jth beamlet, and $\sigma_{x'_j} = \sigma_j / L$ is the r.m.s. divergence of the jth beamlet. A pepper-pot is simply a two-dimensional version of the mask of slits, where a mask with a matrix of holes results in a two-dimensional distribution of beamlets; projecting this distribution onto one axis then facilitates a calculation in either of the transverse dimensions via the

above analysis. An independently measured mean beam energy is used to calculate the normalised emittance $\varepsilon_n \sim \langle\gamma\rangle\varepsilon_x$.
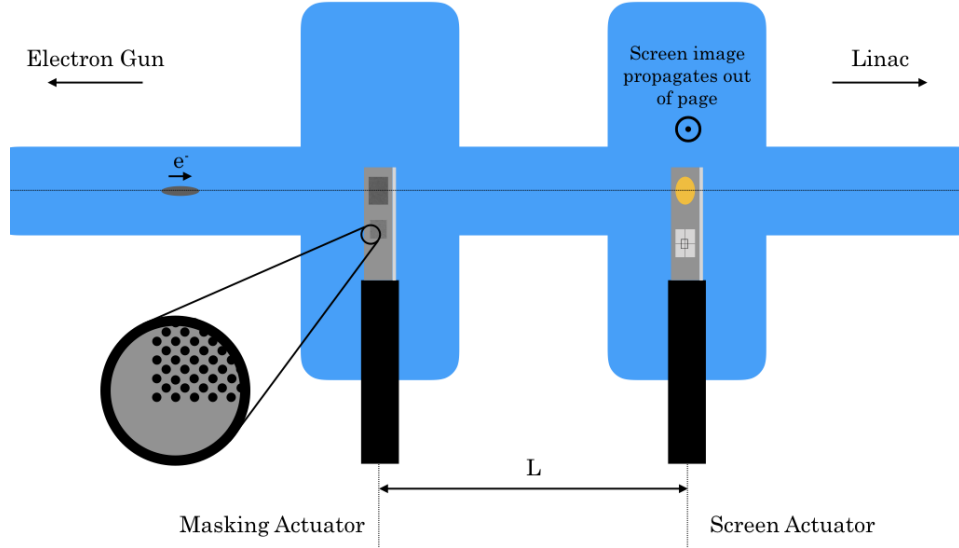
Figure 1.6: The layout of the pepper-pot assembly within the AWAKE electron source beamline, looking down from the topside.

The pepper-pot system is comprised of a Tungsten mask and an array of screens, held on separate actuator arms $L = 160\,\mathrm{mm}$ apart from each other and brought into the beam path downstream from the photoinjector for measurement. A pair of different masks with two hole sizes were available on the masking actuator, while the screen actuator held a yttrium-aluminum-garnet (YAG) scintillator screen, an aluminium foil optical transition radiation (OTR) screen, and a ceramic calibration target to provide a length scale for the resulting images. A layout of the pepper-pot is shown in figure 1.6. The screen actuator is positioned at 45° with respect to the beam axis, to allow perpendicular imaging by a networked charge coupled device (CCD) camera and $f = 100\,\mathrm{mm}$ focal length lens positioned directly above the screen. The camera was suspended from a specially designed gantry in a black-out enclosure to minimise unwanted light signal from the surrounding environment. Despite this, the OTR emission was not discernible above the background noise signal

when imaged with the CCD camera, given the electron beam intensity. For all subsequent measurements the YAG scintillator screen was used. An electron multiplying CCD camera capable of detecting single photons was available but integration into the pepper-pot system was not possible given the time constraints of the experiment. The less sensitive CCD cameras had the advantage that their data were published to an established local network, and were thereby more straightforward to interface with.
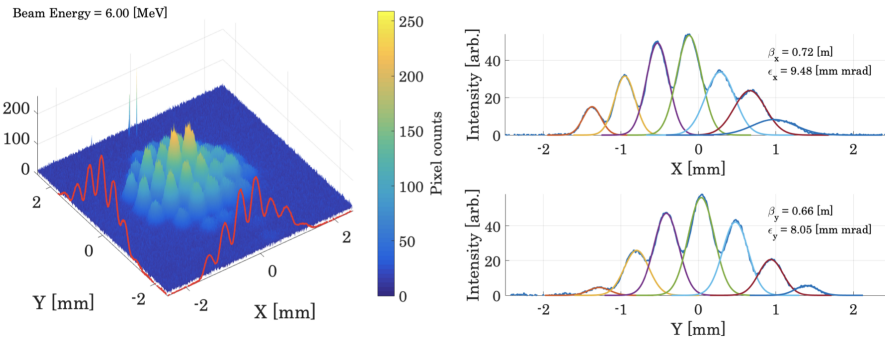
Figure 1.7: Two–dimensional image data from the AWAKE pepper–pot, with corresponding fitted beamlet projections.

An example image with its projections in the x and y axes is shown in figure 1.7. In order to automate image capture and analysis a graphical user interface (GUI) was developed to be run from the experimental control room, using the camera data published on the local network. This was written with the PyQt5 library for Python, and a screenshot is shown in figure 1.8. The GUI subscribes to live camera data from the experiment, which the user selects and crops to highlight the region of interest around the two-dimensional beamlet distribution, as well as entering the beam energy and mask size in use. The GUI displays the beamlet projections in each dimension and the user is prompted to hand pick the beamlet boundaries. Using these boundaries and the image data, the GUI fits Gaussian distributions to each beamlet in both projected dimensions. The GUI instances a separate class which is written to perform the emittance reconstruction with the system of equations (1.3–

1.5), using the fitted distributions and user-entered information to calculate the two-dimensional normalised beam emittance ε_n^* and corresponding Twiss parameters.
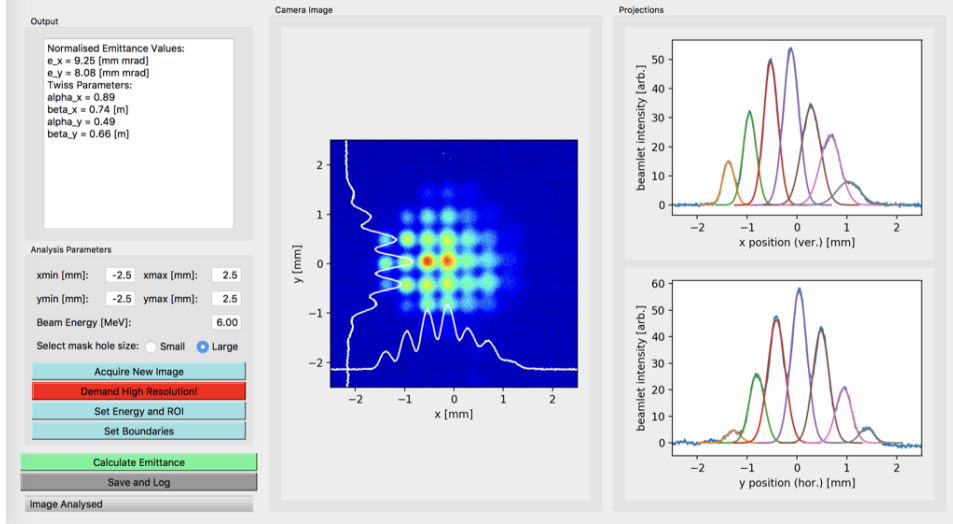
Figure 1.8: A screenshot of the pepper-pot GUI.

Finally, all data are saved to the experimental logbook. In the example shown in figures 1.7 and 1.8, the normalised emittance was calculated in each transverse dimension as $\varepsilon_{x,n} = 9.25\,\mathrm{mm\,mrad}$ and $\varepsilon_{y,n} = 8.08\,\mathrm{mm\,mrad}$. After a series of extensive measurement campaigns an inconsistency was found between the pepper-pot and quadrupole scan emittance measurements, with the pepper-pot typically overestimating normalised beam emittance. It was found to be the case that the pepper-pot algorithm summarised in equations (1.3–1.5) could only provide an accurate estimate when the beam was focused at the plane of the pepper-pot mask, and when the incoming beam was Gaussian. When projected, non-Gaussian beamlets have high intensity tails which erroneously skew the calculated terms of the pepper-pot algorithm and overestimate the final value of emittance [55]. The measured emittance was found to be consistent with the quadrupole scan method for Gaussian electron beams that were well matched to the electron injector beamline and were focused to a waist at the mask, indicating that by design the mask was optimised to

43

one particular beam envelope. Emittance measurements outside of this ideal scenario were required, and because the pepper-pot system was sensitive to incoming beam parameters within their operational range, the measurement was somewhat flawed. Therefore, because different mask geometries are optimised for a particular beam envelope, to improve the operation of the pepper-pot system different mask geometries are required to increase the range of beam parameters the system can accept [55]. However, the pepper-pot still provided a useful alternative to the quadrupole scan measurement and the pepper-pot YAG screen was used frequently to characterise the electron beam size and distribution under a range of focusing conditions [43].

1.3 Thesis Outline

This thesis will use numerical simulations to investigate the generation of an electron beam to be injected into a proton-driven plasma wakefield, determine how its emittance may be measured, and examine how its properties evolve as it is accelerated, in order to address some of the challenges for AWAKE Run 2, outlined in section 1.2.2. The evolution of the electron beam properties over hundreds of metres are also studied. Chapter 2 introduces fundamental accelerator concepts, properties of plasmas, and principles of plasma wakefield acceleration to give theoretical context to the presented simulation studies. Chapter 3 describes the motion of single electrons and electron beams in ion channels, as well as the synchrotron radiation that electrons produce during such motion. Chapter 4 gives an overview of particle-in-cell simulation and the simulation codes used in this thesis. In Chapter 5 an LWFA scheme for the AWAKE Run 2 electron injector system that meets the beam parameter requirements for emittance preservation is identified, a compact focusing triplet is designed, and considerations for the transport of such a beam are defined. Chapter 6 presents a feasibility study for an emittance diagnostic based on be-

tatron radiation spectroscopy, which fully characterises the betatron radiation emission from electron beams in AWAKE Run 2. Chapter 7 investigates the long-term evolution of accelerated electron beam properties in a proton-driven wakefield under the influence of radiation reaction. The conclusions of this thesis and their implications for proton-driven plasma wakefield acceleration are discussed in Chapter 8.

Chapter 2

Plasma Wakefield Acceleration

2.1 Fundamental Accelerator Concepts

The motions of charged particles in an accelerator are controlled with external electromagnetic fields, which are provided by the components of the accelerator beamline. Plasma wakefield acceleration may address the fundamental limitation of RF-based accelerators, namely their maximum achievable accelerating gradient, but it also raises new challenges and new regimes of beam properties: on exiting a plasma wakefield an electron beam is highly divergent, typically on the mrad scale, while it also has the potential to reach unprecedented beam energies. Such electron beams are both more difficult to control, and harder to dump safely without significant radioactivation of the peripheral materials surrounding an accelerator.

Novel accelerator technologies are also being investigated to address these challenges, and may in turn be required to replace each component of the conventional accelerator beamline. High-gradient plasma lenses could replace transverse focusing optics to provide emittance preservation for electron beams exiting plasma wakefields [56], and compact plasma-based beam dumps could

reduce beam energy in a shorter distance, activating less material, while potentially facilitating beam energy recovery [57, 58, 59]. Active feedback systems employing genetic algorithms have been shown to optimise LWFA electron beam parameters by automatically varying the driving laser pulse temporal distribution [60], a brute-force approach well suited to the nonlinear response of laser-plasma interaction. Despite ongoing developments, many fundamental accelerator concepts remain true no matter the accelerating medium used. It is therefore helpful to revise them in order to give sufficient context to the study of electron beam dynamics in a proton-driven plasma wakefield.

2.1.1 Particle beams in phase space

Particle beams used in accelerators typically contain 10^8-10^{11} particles per bunch, and characterising their motion through an accelerator beamline individually is impractical. Therefore, dynamical variables that when taken together describe the properties of the bunch as a whole, such its size, are used. The behaviour of a single particle acted on by a magnetic field $\vec{B} = \nabla \times \vec{A}$ may be described using Hamilton's equations [61]:

$$\frac{dx}{dt} = \frac{dH}{dp_x}, \tag{2.1}$$

$$\frac{dp_x}{dt} = -\frac{dH}{dx}, \tag{2.2}$$

where its transverse horizontal position coordinate x and its relativistic conjugate momentum $p_x = (\gamma m v_x + q A_x)/P_0$ are dynamical variables that may evolve in time t. An individual particle has a rest mass m, Lorentz factor γ, charge q and a transverse velocity v_x; A_x is the horizontal component of the magnetic vector potential $\vec{A}$. The reference momentum P_0 is the nominal or 'design' value of momentum. It is chosen so that most particles within a bunch have a momentum close to P_0 throughout the accelerator beamline.

At a given moment in time, the positions and momenta of an ensemble of particles occupy an area in phase space (x, p_x). The Hamiltonian H is a function of x and p_x that defines the dynamics of such a system of particles. As a single particle travels through an accelerator with coordinates of x and p_x it traces out an ellipse in phase space as its motion is altered by the components in the beamline. The area of an ellipse occupied by the entire ensemble of particles in phase space is proportional to a quantity known as the geometric beam emittance ε_x. For a relativistic beam where all particles have a normalised longitudinal velocity $\beta = v_z/c \sim 1$ the geometric emittance in the transverse horizontal direction is

$$\varepsilon_x = \sqrt{\langle x^2 \rangle \langle p_x^2 \rangle - \langle x p_x \rangle^2}, \tag{2.3}$$

where angle brackets denote an average over the particle ensemble. Equivalent quantities exist in the transverse vertical y and longitudinal z directions, assuming there is no coupling between them. According to Liouville's theorem the area $S = \pi \varepsilon_x$ enclosed by the phase space ellipse, shown in figure 2.1, will be invariant under a symplectic transformation, which is typically a feature of a system in motion that may be described by a Hamiltonian. It should be noted that the phase space of a real beam would not have a sharp boundary as particles always have some distribution in phase space. When Gaussian, the geometric emittance of particle beams in phase space is often quoted as an r.m.s. value, and all values of emittance in this thesis are quoted as such. The shape of the ellipse and its orientation in phase space (x, p_x) are given by the Courant-Snyder or Twiss parameters [61]

$$\alpha_x = -\frac{\langle x p_x \rangle}{\varepsilon_x}, \quad \beta_x = \frac{\langle x^2 \rangle}{\varepsilon_x}, \quad \gamma_x = \frac{\langle p_x^2 \rangle}{\varepsilon_x}. \tag{2.4}$$

A component in an accelerator beamline producing a magnetic field, such
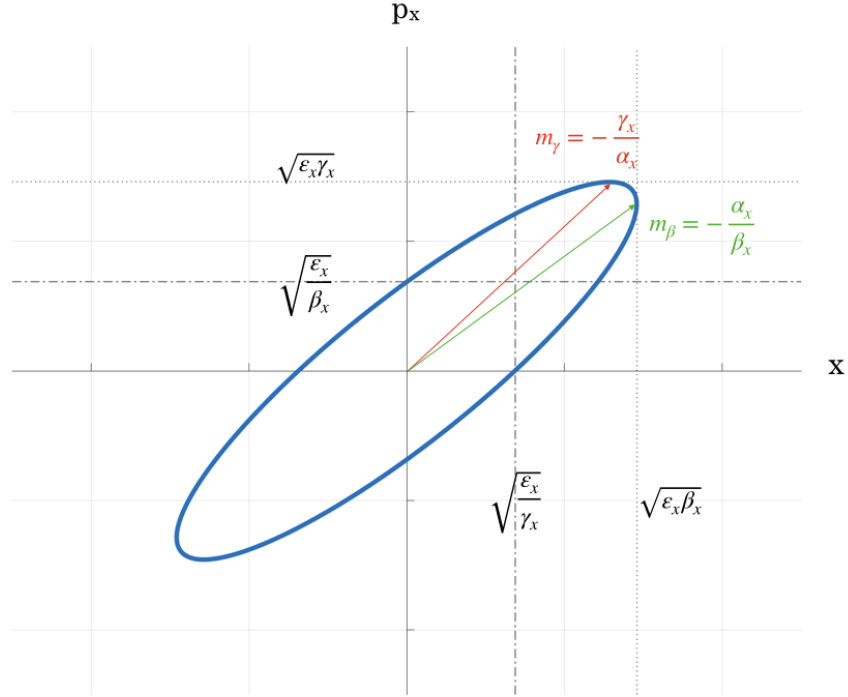
Figure 2.1: The transverse phase space (x, p_x) portrait of a particle beam with area $S = \pi \varepsilon_x$, whose boundary encloses the orbits in phase space of all the constituent particles. The Twiss parameters α_x, β_x and γ_x determine the shape and orientation of the ellipse.

as a quadrupole magnet, acts on an ensemble of particles, mapping each from one position before the quadrupole to another after the particle has transited through its magnetic field. The Twiss parameters make up the elements of a symplectic transfer matrix that defines such a map. As a particle ensemble or bunch propagates through a series of components, each with their own transfer matrix, the bunch size will vary within the boundaries of a fixed envelope.

The Twiss parameters therefore give the local variation in the bunch size, while the geometric emittance ε_x represents an invariant size. Figure 2.2 shows a beam in phase space (x, p_x) at three different points z_1, z_2, and z_3. Having passed through a quadrupole that focuses in the horizontal direction x, the

beam converges up until z_2, where $\alpha_x = 0$ and the beam reaches its minimum transverse size, known as the beam waist. After this point the beam begins to diverge. The Twiss parameter β_x expresses the rate at which the the beam size changes with z. For the bunch size to be preserved during transport through a beamline of accelerator components, the Twiss parameters of the beamline must be matched to the Twiss parameters of the distribution of particles within the bunch.
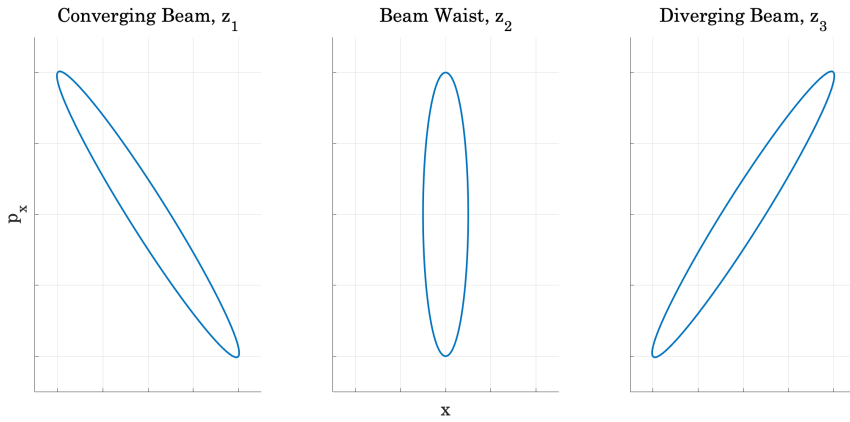
Figure 2.2: The evolving transverse phase space (x, p_x) portrait of a particle beam in a field-free drift, after being focused in the x direction. At three different longitudinal positions z_1, z_2 and z_3 the beam is converging, at a waist and diverging respectively. At the beam waist α_x, and therefore the gradient given by both m_γ and m_β of the ellipse with respect to the momentum axis, is zero.

The complete set of dynamical variables for a particle in an accelerator may be extended to the vertical and longitudinal directions y and z, and also includes the deviation δ in energy

$$\delta = \frac{E}{P_0 c} - \frac{1}{\beta_0} \tag{2.5}$$

from a reference momentum P_0, where $E = \gamma m c^2$ is the particle energy and β_0 is the velocity of a particle moving with momentum P_0 normalised to

the speed of light in vacuum c. To meet the conditions of symplecticity and therefore preserve the geometric emittance of a particle bunch under transport it is assumed that P_0 is constant, and that energy deviations δ are small. In the case of a particle gaining energy through acceleration the former condition is not true. Therefore a new quantity that remains invariant under acceleration is required. From the expression for p_x and equation (2.3) it is apparent that following acceleration, a new reference momentum P_0' will result in a new geometric emittance [61]:

$$\varepsilon_x' = \frac{P_0}{P_0'}\varepsilon_x; \tag{2.6}$$

$$P_0'\varepsilon_x' = P_0\varepsilon_x, \tag{2.7}$$

and by expanding P_0

$$\beta_0'\gamma_0'\varepsilon_x' = \beta_0\gamma_0\varepsilon_x; \tag{2.8}$$

$$\varepsilon_{x,n} = \beta_0\gamma_0\varepsilon_x. \tag{2.9}$$

The normalised emittance $\varepsilon_{x,n}$ is invariant under a change of reference momentum. The normalised emittance of an electron beam accelerated in a plasma wakefield has a further dependence on the divergence and energy deviation of the particle bunch [62], which may be orders of magnitude greater than beams accelerated in metallic structures. This will be discussed in section 2.3. Because the geometric emittance ε_x scales inversely with the reference momentum, the size of a particle bunch will decrease as it is accelerated for a fixed beta function β_x. This mechanism is known as adiabatic damping, and is discussed in the context of proton-driven plasma wakefield acceleration in Chapter 3.

2.1.2 Metallic structure wakefields

Charged particles are themselves sources of electromagnetic fields and when bunched will interact with one another, affecting the dynamics of the bunch as a whole, known as collective effects. The mutual repulsion of a bunch of like charges modelled as a uniform distribution of charge and current density is known as the space-charge effect. The force $\vec{F}$ seen by an individual particle in the resultant electromagnetic field is given by the Lorentz force equation:

$$\vec{F} = q(\vec{E} + \vec{v} \times \vec{B}), \tag{2.10}$$

where q is the particle charge and $\vec{v}$ its velocity. Space-charge effects alter the distribution of charge within a bunch, leading to a growth in beam size and spread of relative particle momenta. As discussed, these parameters form the emittance of a particle beam. Space-charge effects can therefore result in emittance growth of the beam irrespective of its surroundings and during propagation in free space. With the presence of a metallic cavity that encloses the trajectory of a particle bunch, the fields it generates interact with the cavity to produce a distinct electromagnetic field that acts back on the beam and perturbs its motion. This is known as a wakefield [63] and its existence relies on some boundary to the self-fields of the particle bunch.

At high energies, where the velocities of particles become relativistic, wakefields dominate the collective dynamics of charged particles in accelerators over other mechanisms such as the space-charge effect [61]. Wakefields can have detrimental consequences for a particle beam such as emittance growth and distortion of bunch distribution, or even lead to unstable motion and beam loss. Wakefields are induced by the electric field around a particle bunch, which can be modelled as a point charge. Consider a point charge q moving in a direction z with a constant velocity v with respect to a stationary frame of reference

S, and zero velocity with respect to a co-moving frame S', both of which are non-accelerating. The Lorentz transformation between the coordinate systems of the two frames is given by

$$x' = x, \tag{2.11}$$

$$y' = y, \tag{2.12}$$

$$z' = \gamma(z - vt), \tag{2.13}$$

$$\gamma = \frac{1}{\sqrt{1 - v^2/c^2}}. \tag{2.14}$$

The electric field $\vec{E'}$ generated by q in its rest frame, S', is isotropic (see figure 2.3):

$$\vec{E'} = \frac{q\vec{r'}}{4\pi\varepsilon_0 r'^3}, \tag{2.15}$$

$$\vec{r'} = \sqrt{x'^2 + y'^2 + z'^2}. \tag{2.16}$$

Therefore the components of $\vec{E'}$ are

$$E'_x = \frac{qx'}{4\pi\varepsilon_0 (x'^2 + y'^2 + z'^2)^{3/2}}, \tag{2.17}$$

$$E'_y = \frac{qy'}{4\pi\varepsilon_0 (x'^2 + y'^2 + z'^2)^{3/2}}, \tag{2.18}$$

$$E'_z = \frac{qz'}{4\pi\varepsilon_0 (x'^2 + y'^2 + z'^2)^{3/2}}. \tag{2.19}$$

With the coordinate transforms in equations (2.11-2.14) and electric field transforms $E_x = \gamma E'_x$, $E_y = \gamma E'_y$, and $E_z = E'_z$ [64] the electric field around the point charge with respect to a stationary observer in frame S may be found:

$$E_x = \frac{q\gamma x}{4\pi\varepsilon_0 [x^2 + y^2 + \gamma^2(z - vt)^2]^{3/2}}, \tag{2.20}$$

$$E_y = \frac{q\gamma y}{4\pi\varepsilon_0 [x^2 + y^2 + \gamma^2(z - vt)^2]^{3/2}}, \tag{2.21}$$

$$E_z = \frac{q\gamma(z - vt)}{4\pi\varepsilon_0 [x^2 + y^2 + \gamma^2(z - vt)^2]^{3/2}}. \tag{2.22}$$

The dependence of z on γ in these equations show that with increasing velocity in the direction of motion z the electric field is compressed. This contributes to a flattening of the electric field around a relativistic point charge into a plane perpendicular to its motion, as shown in figure 2.3. In the limit $v \to c$ the electric field is entirely perpendicular to the charge. It is for this reason that space-charge effects are negligible for highly relativistic particle beams.
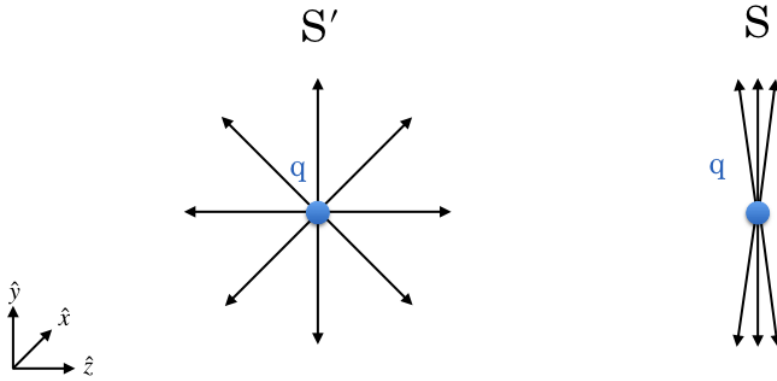
Figure 2.3: The electric field around a point charge, isotropic in its comoving rest frame S', and flattened into a plane perpendicular to the direction of motion z in the case of a relativistic velocity with respect to an observer in a stationary frame S

Examples of wakefield excitation in an accelerator beamline can be observed both inside a resonant cavity, and within the metallic surfaces enclosing the beam. In the first an electric field with a form given by equations (2.20-2.22) is generated by a particle entering the cavity and spreads out as it is diffracted at the entrance aperture. The field is reflected by the opposing cavity wall, resulting in wakefields that undergo resonant oscillations depending on

boundary conditions set by the cavity geometry, and therefore have specific frequencies. Generally, wakefields excited due to the varying size and shape of beamline components are known as geometric wakefields. They are observed by and influence particles passing through the cavity at later times. The rate at which a particular resonant frequency or mode of oscillation of the wakefield decays is given by the quality factor Q_m:

$$Q_m = 2\pi \frac{E_m}{U},\tag{2.23}$$

where E_m is the energy stored in the cavity for the particular mode and U is the energy lost per oscillation [65]. For $Q_m >> 1$:

$$E_m(t) = E_m(0)\,e^{-\frac{\omega t}{Q_m}},\tag{2.24}$$

where ω is the frequency of oscillation in time t. Wakefield modes induced in RF accelerating cavities can have large Q_m factors and therefore by equation (2.24) take many oscillations to dissipate. Higher-order modes (HOMs) can lead to beam instabilities and are selectively damped by actively lowering their Q_m factor. A second example of wakefield excitation is seen when a particle bunch passes through a straight vacuum chamber. For a perfectly conducting material with conductivity $\sigma \sim \infty$ an image charge is induced in the vacuum chamber wall that follows the particle bunch, remaining parallel to it. As $v \to c$ the image charge is completely perpendicular to the bunch and the two do not interact. In the case that the chamber walls have a finite conductivity σ, losses through ohmic heating mean that the particle bunch and image charge are no longer parallel, giving rise to a wakefield that will perturb the motion of witness particles arriving later – known as a resistive wall wakefield.

Typically geometric wakefields described in the first example have a greater effect on beam dynamics than those generated by the finite conductivity of the

vacuum chamber walls. The wakefields generated by a particle bunch with a distribution of charges will act on a point charge q, arriving at a later time than the leading bunch, via the Lorentz force, i.e. equation (2.10). It is possible to model this force with a set of equations that depend on the distance z between charge distribution and witness particle, therefore making use of the relative positions of particles, which is more convenient in the study of beam dynamics. Such equations are known as wake functions and they describe the forces on particles resulting from wakefields in the time domain; the Fourier transform of a wake function yields an impedance, which describes the forces due to wakefields in the frequency domain. Each component of the accelerator beamline contributes towards its total impedance. The wake function $W_m(z)$ and multipole moment of the particle bunch I_m, which characterises its charge distribution and therefore the wakefields it excites (where m is the mode number; $m = 0$ for monopole, $m = 1$ for dipole etc.), both contribute to a wake potential $\vec{V} = [\vec{f}]_z$. This is an integral of a quantity f, such as an electromagnetic field component, over the path taken by the witness particle through the wakefield, with fixed distance z from the charge distribution. The wake potential is seen by the witness particle and for a given direction the resulting force on the particle may be derived from it.

Components of the wake potential in the transverse (r, θ) and longitudinal (s) directions are given by [61]

$$V_r = -qI_mW_m(z)mr^{m-1}cos(m\theta), \qquad (2.25)$$

$$V_\theta = qI_mW_m(z)mr^m sin(m\theta), \qquad (2.26)$$

$$V_s = -qI_mW'_m(z)r^m cos(m\theta), \qquad (2.27)$$

where $W'_m(z) = dW_m(z)/dz$. Collecting the transverse wake potentials into a quantity $\vec{V}_\perp$:

$$\vec{V}_\perp = V_r \hat{r} + V_\theta \hat{\theta}, \tag{2.28}$$

and taking the gradient of longitudinal component V_s with operator $\nabla_\perp = (\partial/\partial r, \partial/\partial \theta)$

$$\nabla_\perp V_s = \left(\frac{\partial V_s}{\partial r}, \frac{\partial V_s}{\partial \theta} \right), \tag{2.29}$$

$$= -q I_m W_m'(z) m r^{m-1} cos(m\theta) \hat{r} + q I_m W_m'(z) m r^m sin(m\theta) \hat{\theta}, \tag{2.30}$$

$$= \frac{\partial}{\partial z} [-q I_m W_m(z) m r^{m-1} cos(m\theta) \hat{r} + q I_m W_m(z) m r^m sin(m\theta) \hat{\theta}], \tag{2.31}$$

$$= \frac{\partial}{\partial z} (V_r \hat{r} + V_\theta \hat{\theta}), \tag{2.32}$$

it can be seen that

$$\nabla_\perp V_s = \frac{\partial}{\partial z} \vec{V}_\perp. \tag{2.33}$$

Therefore the longitudinal and transverse wakefield excited in a vacuum chamber by a passing particle bunch are related, given by equation (2.33), which is known as the Panofsky-Wenzel theorem [66]. The causality imposed by the speed of light in vacuum c means that a relativistic particle cannot interact with a wakefield behind it. Consequently, for a bunch of particles, those at the head see nothing of the wakefield generated by the other charges, whereas those at the rear see the wakefield generated by the entire population of charges in the bunch. Therefore on average the charges of a bunch with velocity $v \simeq c$ see a wakefield of half its actual size, which is known as the fundamental theorem of beam loading [67].

An example of the detrimental effects of wakefields on accelerator operation is the beam breakup instability (BBU) that was first observed at the SLAC linear accelerator in the 1960s [68]. For a beam centred in a vacuum chamber pipe the transverse wakefield excited is symmetrical and is therefore self-cancelling. With some transverse offset, potentially arising from the betatron motion of

particles in the beam, the isotropy of the transverse fields is broken. A dipole wakefield generated by the head of a particle bunch will deflect those at the rear. The betatron motion of particles in the rear is resonantly driven by the oscillating wake and their amplitude grows linearly with propagation distance. Eventually this leads to beam losses and break-up. Mitigating BBU requires tight focusing of the beam to suppress betatron oscillation, injection close to the vacuum chamber axis, and rapid acceleration to relativistic energies where the beam is less susceptible to wake forces [63]. A more specific technique employed to address BBU is Balakin-Novokhatsky-Smirnov (BNS) damping [69]. It relies on the head of a particle bunch having a different betatron frequency than the tail, which receives slightly stronger focusing, facilitated by a variable strength quadrupole magnet. This takes the head-generated wake and bunch tail out of resonance and compensates for the deflection of the transverse dipole wakefield.

Conventional wakefield concepts such as the Panofsky-Wenzel theorem remain true in a plasma wakefield, and while wakefields are often seen as detrimental to the intended operation of metallic structure-based accelerators, they are fundamental to the operation of plasma-based accelerators. Nevertheless, parallels do exist between unwanted instabilities, such as the BBU and Hosing instabilities [40], the latter of which is discussed in the study of betatron radiation spectroscopy presented in Chapter 6. Conceptually, combined drive and witness beam accelerators using RF fields already exist, e.g. CLIC [6], which convert the energy of a drive beam, through a metallic transformer, and on to a witness beam. Plasma can be thought of as a new transformer material that hosts a wakefield, which due to its nature can sustain accelerating electric fields that are many times stronger, and from which charged particle beams may gain energy.

2.2 Properties of Plasmas

2.2.1 Debye length

A plasma may be defined as a quasi-neutral gas of electrons, ions and neutral atoms, which exhibit collective behaviour. A test charge q inserted into a plasma generates an electrostatic potential $\phi(r)$, with an associated electric field $\vec{E}$, that acts on the plasma particles [70]:

$$\phi(r) = \frac{q}{4\pi\varepsilon_0 r}e^{-\frac{r}{\lambda_D}}, \tag{2.34}$$

where ε_0 is the permittivity of free space and r is the distance from the charge q. In the limit for which the electrostatic potential $\phi(r)$ goes to zero, the test charge is screened out and the quasi-neutral equilibrium condition of the plasma is recovered. For a plasma with electron number density n_e and temperature T_e, charge screening occurs over a range known as the Debye length λ_D,

$$\lambda_D = \sqrt{\frac{\varepsilon_0 k_B T_e}{e^2 n_e}}, \tag{2.35}$$

and therefore the test particle acts only on those particles within a sphere of radius $r \leq \lambda_D$, known as the Debye sphere. Here, k_B is the Boltzmann constant and e is the electron charge. Collective effects dominate the behaviour of a plasma if there are many particles within the Debye sphere. One collective effect is a plasma oscillation. A driving force that displaces plasma electrons from their equilibrium position will leave the heavier plasma ions unaffected, generating a charge imbalance. The stationary ions exert a strong electrostatic force that works to re-establish charge neutrality against the electron momentum, initiating oscillations of the plasma electrons about an equilibrium position at a characteristic frequency, ω_p.

2.2.2 Plasma frequency

Consider a thin slab of electrons of mass m_e with surface area S and number density n_e given an displacement Δx against a background of stationary ions (see figure 2.4). The resulting electric field arising from the charge imbalance provides a restoring force that opposes the displacement:

$$F_x = m_\Delta \frac{d^2 \Delta x}{dt^2} = -Q_\Delta E_x, \tag{2.36}$$

where $m_\Delta = m_e n_e S \Delta x$ is the mass of the slab, E_x is the restoring electric field, and $Q_\Delta = -e n_e S \Delta x$ the total displaced charge. From Gauss' law and the net charge density $\rho = e(n_i - n_e)$, where n_i is the ion number density

$$\nabla \cdot \vec{E} = \frac{\rho}{\varepsilon_0} = \frac{e(n_i - n_e)}{\varepsilon_0}, \tag{2.37}$$

and with the integral form of Gauss' law

$$\int_V \nabla \cdot \vec{E} d\vec{V} = \oint_S \vec{E} \cdot d\vec{S}, \tag{2.38}$$

$$\oint_S \vec{E} \cdot d\vec{S} = \int_V \frac{\rho}{\varepsilon_0} d\vec{V}, \tag{2.39}$$

where $d\vec{S}$ is a surface element of S, the electric field generated by a volume $V = S \Delta x$ of displaced electrons (where $n_i = 0$) is

$$E_x = -\frac{e n_e \Delta x}{\varepsilon_0}. \tag{2.40}$$

By substituting equation (2.40) into (2.36), an equation of motion for the electron oscillation is obtained:

$$\frac{d^2 \Delta x}{dt^2} = -\frac{n_e e^2}{m_e \varepsilon_0} \Delta x, \tag{2.41}$$

60
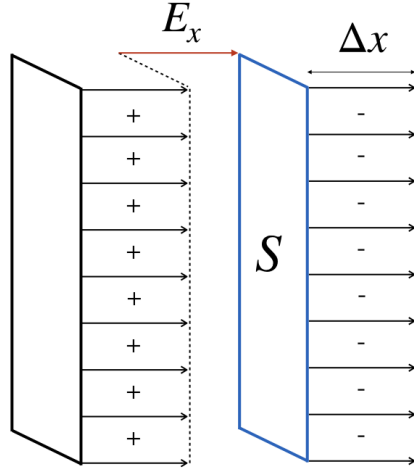
Figure 2.4: The separation Δx of a thin slab of plasma electrons with area S from an ion background leaves two regions, one with an excess of positive charge, the other with an excess of negative charge. The electrostatic potential generated between them results in an electric field E_x that opposes the charge separation.

$$\frac{d^2\Delta x}{dt^2} + \omega_p^2 \Delta x = 0, \tag{2.42}$$

where the displacement has a characteristic frequency of oscillation, known as the plasma frequency ω_p:

$$\omega_p = \left(\frac{n_e e^2}{m_e \varepsilon_0}\right)^{\frac{1}{2}}. \tag{2.43}$$

2.2.3 Driven electrostatic waves in plasmas

The electric field of a high-intensity laser or charged particle beam drives plasma oscillations at ω_p, generating an electric field of alternating accelerating and decelerating phases with a wavelength of $\lambda_p = 2\pi c/\omega_p$ in the longitudinal direction. Focusing and defocusing fields normal to the propagation axis are also excited, and this wave structure follows the driving laser or particle beam at a phase velocity equal to the laser pulse group velocity $v_{g,las}$ or particle

beam velocity v_z respectively. Electrons injected into the accelerating phase of the field may gain energy. An electric field may be expressed as the gradient of an electrostatic potential:

$$\vec{E} = -\nabla\phi. \tag{2.44}$$

From Gauss' law,

$$\nabla \cdot \vec{E} = \frac{\rho}{\varepsilon_0} = \frac{e(n_i - n_e)}{\varepsilon_0}, \tag{2.45}$$

where n_i and n_e are the plasma ion and electron densities respectively. By substituting $\vec{E}$ for the electrostatic potential, the Poisson equation is obtained:

$$-\nabla^2\phi = \frac{e(n_i - n_e)}{\varepsilon_0}. \tag{2.46}$$

In other words, a density change $\delta n = n_i - n_e$ gives rise to an electrostatic potential via the Poisson equation, which has an associated electric field. Assuming a stationary ion background the density change for a period oscillation of plasma electron density in a direction z is given by:

$$\delta n = \delta n_e sin(k_p z - \omega_p t), \tag{2.47}$$

where ω_p is the angular frequency of the plasma wave, $k_p = 2\pi/\lambda_p$ is the associated wavenumber and it is assumed that the maximum possible perturbation corresponds to $100\,\%$ of the plasma electron density. This gives rise to a changing electric field, via the Poisson equation:

$$\nabla \cdot \delta\vec{E} = -\frac{e\delta n}{\varepsilon_0}, \tag{2.48}$$

$$\nabla \cdot \delta\vec{E} = -\frac{e\delta n_e}{\varepsilon_0} sin(k_p z - \omega_p t). \tag{2.49}$$

Solving for $\vec{E}(z, t)$

$$\nabla \cdot \left(\frac{e\delta n_e}{k_p \varepsilon_0} cos(k_p z - \omega_p t) \right) = 0\vec{e}_x - 0\vec{e}_y - \frac{e\delta n_e}{\varepsilon_0} sin(k_p z - \omega_p t)\vec{e}_z, \qquad (2.50)$$

$$\delta \vec{E}(z,t) = \frac{e\delta n_e}{k_p \varepsilon_0} cos(k_p z - \omega_p t)\vec{e}_z. \qquad (2.51)$$

Using the derived expression for the plasma frequency, $\omega_p = (n_e e^2/m_e \varepsilon_0)^{1/2}$, ε_0 can be eliminated from equation (2.51):

$$\delta \vec{E}(z,t) = \frac{e\delta n_e m_e \omega_p^2}{k_p n_e e^2} cos(k_p z - \omega_p t)\vec{e}_z. \qquad (2.52)$$

Finally, by substituting for the phase velocity $v_\phi = \omega_p/k_p$, an expression for the time varying, longitudinal, and therefore accelerating, electric field associated with an electrostatic plasma density wave (see figure 2.5) is obtained [71]:

$$\delta \vec{E}(z,t) = \frac{m_e \omega_p v_\phi}{e} \frac{\delta n_e}{n_e} cos(k_p z - \omega_p t)\vec{e}_z, \qquad (2.53)$$

$$= E_0 \frac{\delta n_e}{n_e} cos(k_p z - \omega_p t)\vec{e}_z, \qquad (2.54)$$

where

$$E_0 = \frac{m_e \omega_p v_\phi}{e} \qquad (2.55)$$

is the electric field amplitude. This amplitude is known as the cold plasma non-relativistic wavebreaking limit. It represents the largest electric field that can be sustained in a plasma, before the wave 'breaks' and electron motion overlaps adjacent wave periods. Assuming a relativistic wave with $v_\phi \sim c$ this field is $96\,\mathrm{GVm}^{-1}$ for a plasma with density $1 \times 10^{18}\,\mathrm{cm}^{-3}$, three orders of magnitude greater than the maximum electric field that can be operated in a metallic-structure based accelerator of around $100\,\mathrm{MVm}^{-1}$.
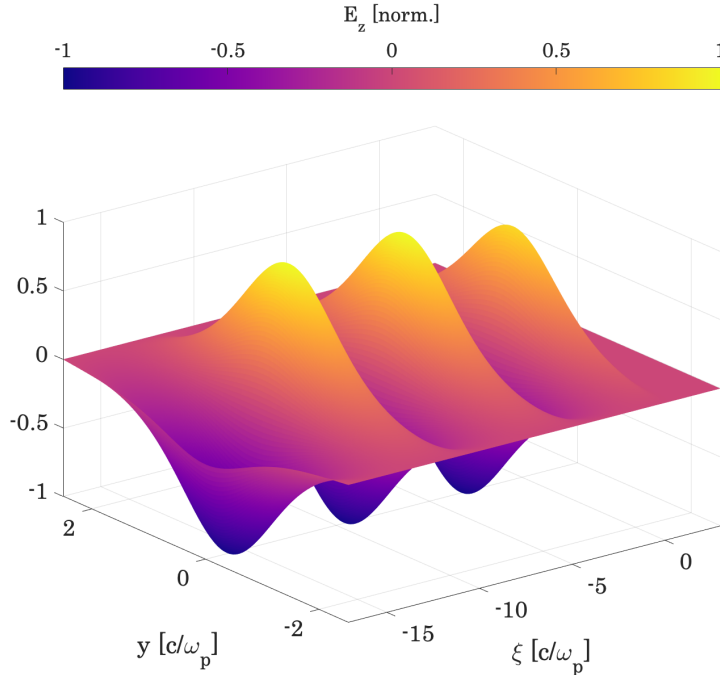
Figure 2.5: The simulated longitudinal electric field $\delta\vec{E}(z,t)$ of a linear sinusoidal plasma wave driven by a charged particle beam, produced with the particle-in-cell code QV3D [72]. The wakefield phase velocity is orientated in the positive ξ direction, a coordinate co-moving with the driving beam. E_z is normalised to 1.

To excite and maintain a plasma wakefield at or near to the wavebreaking limit the driving laser pulse or particle beam must meet specific criteria, which are discussed in the following sections. The wavebreaking limit is in fact modified under different conditions. The limit is raised in the case of a relativistic phase velocity v_ϕ of the plasma wave [73],

$$E_0 = \frac{m_e c \omega_p}{e} \sqrt{2}(\gamma_\phi - 1)^{\frac{1}{2}}, \tag{2.56}$$

where $\gamma_\phi = (1 - v_\phi^2/c^2)^{-1/2}$. Conversely, the limit is reduced by electron thermal motion in the warm plasma non-relativistic case, as this may make a sufficient contribution towards the energy required for an electron to escape and subsequently become trapped in an adjacent period [73]:

$$E_0 = \left(1 - \frac{8}{3}\beta_T^{\frac{1}{4}} + 2\beta_T^{\frac{1}{2}} - \frac{\beta_T}{3}\right)^{\frac{1}{2}}, \tag{2.57}$$

where $\beta_T = 3k_p T_e / m_e v_\phi^2$.

The one-dimensional electron quiver velocity v_E is the motion of plasma electrons under the influence of an electric field, and is distinct from the thermal velocity v_T, which itself arises from the kinetic motion of plasma electrons with temperature T_e:

$$v_E = \frac{eE_0}{m_e \omega_p}, \tag{2.58}$$

$$v_T = \sqrt{\frac{k_B T_e}{m_e}}. \tag{2.59}$$
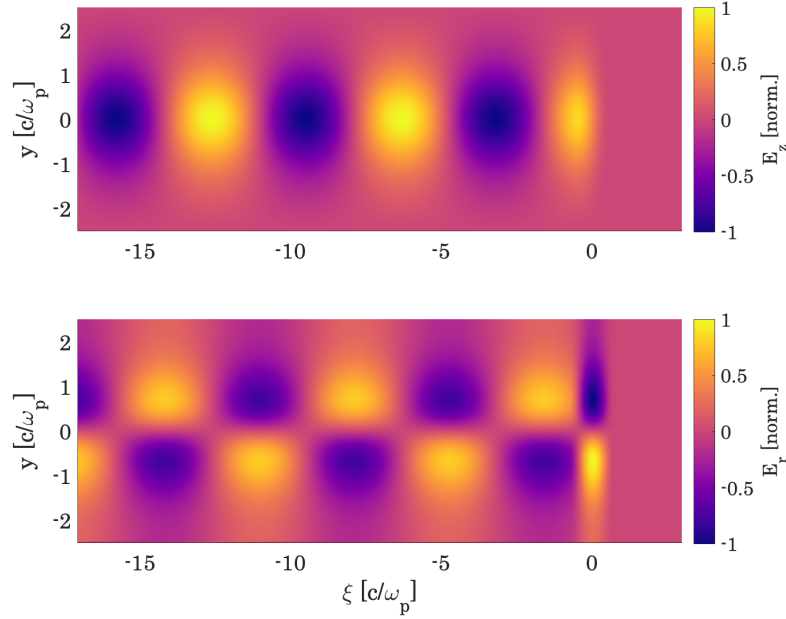
Figure 2.6: The simulated longitudinal electric field $\delta\vec{E}(z,t)$ (top) and transverse electric field $\delta\vec{E}(r,t)$ (bottom) of a linear sinusoidal plasma wave driven by a charged particle beam, produced with the particle-in-cell code QV3D [72].

By solving equation the Poisson equation (2.46) for the transverse component of an electrostatic density wave, the transverse field $\delta\vec{E}(r,t)$, shown in figure 2.6, is found. It has alternating focusing and defocusing phases and a $\pi/2$ phase shift with respect to the longitudinal field $\delta\vec{E}(z,t)$. The electric field phase velocity is orientated in the positive ξ direction, a coordinate co-moving with the driving beam. Both E_z and E_r are normalised to 1.

2.3 Principles of Laser-driven Plasma Wakefield Acceleration

2.3.1 High-intensity laser pulses in plasma

For an electromagnetic wave propagating in a cold, collisionless plasma its angular frequency ω is modified as $\omega^2 = \omega_p^2 + c^2 k^2$. The phase and group velocity of the wave are $v_\phi = \omega/k$ and $v_g = d\omega/dk$ respectively. An overdense plasma is one that has a frequency $\omega_p > \omega$. In this case the wave function has a complex component that results in a decaying amplitude within the plasma; it therefore cannot propagate and is reflected from the surface of the plasma. In an underdense plasma the opposite is true ($\omega_p < \omega$) and the electromagnetic wave propagates freely. The electromagnetic field of a laser pulse may be written [74]

$$\vec{E} = -\nabla\phi - \frac{\delta\vec{A}}{\delta ct}, \tag{2.60}$$

$$\vec{B} = \nabla \times \vec{A}, \tag{2.61}$$

where $\vec{A} = A_0 \cos(kz - \omega t)\vec{e}_\perp$ is the magnetic vector potential, ϕ is the electric scalar potential and ω is the angular frequency of the laser. The normalised vector potential of the laser $\vec{a}$ and its peak value a_0, the laser

66

strength parameter, is a convenient quantity that characterises the nonlinear response of the plasma, given the laser intensity:

$$\vec{a} = \left(\frac{e\vec{A}}{m_e c^2} \right), \tag{2.62}$$

$$a_0 \simeq 0.85 \times 10^{-9} \lambda[\mu m] (I[\text{Wcm}^{-2}])^{\frac{1}{2}}, \tag{2.63}$$

where λ is the laser pulse wavelength in units of micrometers and I is the intensity, in units of Wcm^{-2} [74]. Laser pulses with an intensity on the order of 10^{18} Wcm^{-2}, with $a_0 > 1$, are needed to reach and exceed the cold plasma non-relativistic wake breaking limit, in order to excite a large amplitude plasma wakefield. It is the ponderomotive force of the laser pulse F_p that drives electron density waves in plasma, which is time averaged and proportional to the laser intensity gradient i.e. the rise time of the pulse. In the case of a one-dimensional nonlinear plasma wave, where $a_0 >> 1$, the ponderomotive force of the laser pulse is [74]

$$F_{p,z} = -\frac{m_e c^2}{2\gamma} \frac{\partial a_\perp^2}{\partial z}. \tag{2.64}$$

Such a regime of laser-plasma interaction represents a departure from the linear theory presented in section 2.2.3; the features of a nonlinear wakefield are discussed in section 2.3.3. Figure 2.7 shows the longitudinal electric field $E(t)$ and intensity $I(t)$ of a Gaussian laser pulse in arbitrary units. The two are related as $I(t) \propto |E(t)|^2$. In this thesis the laser pulse duration τ is defined as the full-width at half-maximum (FWHM) of the intensity envelope, shown in figure 2.7 to be $\tau = 22$ fs. Transversely, a Gaussian laser pulse has a spot size w, which in this thesis is taken to be the half width of the pulse's electric field envelope at $1/e$ of its maximum height.
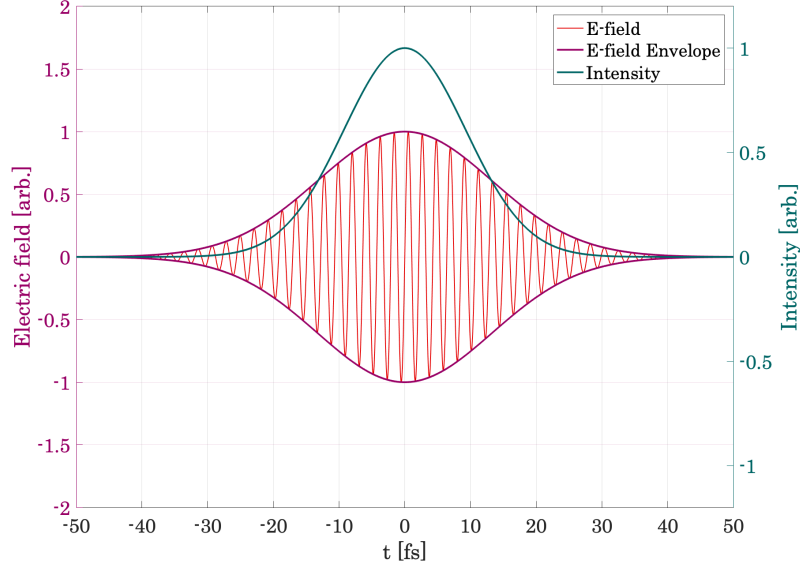
Figure 2.7: The varying electric field and intensity envelope of a Gaussian laser pulse with respect to time

A plasma wakefield driven by a laser pulse propagates with a phase velocity equal to the group velocity of the laser, $v_\phi = v_{g,las} < c$. The high intensities delivered by laser pulses with $a_0^2 >> 1$ mean that relativistic effects must be considered, and results in the electron quiver velocity v_E, i.e. equation (2.58), approaching c and an increase in electron mass by the relativistic Lorentz factor γ. The laser pulse has a Gaussian transverse profile such that the intensity, and therefore the relativistic electron mass, will be maximum at the propagation axis and minimum at the wings. Via the modified refractive index in equation (2.65) the plasma wave phase velocity $v_\phi = c/\eta$ will be at a minimum on axis and maximised at the wings [75]:

$$\eta_\gamma = \left(1 - \frac{\omega_p^2}{\gamma\omega^2}\right)^{\frac{1}{2}} \tag{2.65}$$

As wavefronts at the edge of the pulse are able to catch those at the centre, it is effectively focused. This is known as relativistic self-focusing, first described

theoretically in 1987 by Sprangle et al. [75], which opposes the natural growth in laser spot size due to diffraction in the plasma. The two mechanisms balance at a critical laser power:

$$P_c[\text{GW}] = 17.4\frac{\omega^2}{\omega_p^2}. \tag{2.66}$$

The stable self-guiding, i.e. minimal envelope oscillations over the interaction distance, of an intense laser pulse with $a_0^2 >> 1$ requires that the intensity a_0 and spot size w_0 be matched to the plasma via the relation

$$k_p w_0 = 2\sqrt{a_0} \quad [76]. \tag{2.67}$$

2.3.2 Energy gain

The energy gain of an electron in the accelerating phase of a wakefield is given simply by $W = eE_z \cdot z$ where E_z is the accelerating electric field of the wakefield, and z is the distance over which acceleration is maintained. In a laser-driven wakefield three main mechanisms provide a limit to this distance: defocusing of the laser pulse, dephasing of injected electron with respect to the accelerating phase and energy depletion of the laser driver. As a laser pulse with a Gaussian envelope of wavelength λ propagates along a direction z in the plasma it will diffract, leading to a growth in the spot size w beyond the focal point:

$$w(z) = w_0 \left(1 + \frac{z^2}{Z_R^2}\right)^{\frac{1}{2}}, \tag{2.68}$$

where w_0 is the minimum spot size at the focal point $z = 0$. $Z_R = \pi w_0^2/\lambda$ is the Rayleigh range, the distance taken for the spot size to double with respect to its value at the focal point. As the spot size evolves, growing as the pulse is diffracted, the intensity will be reduced as it is inversely proportional

69

to the pulse cross section. Defocusing will reduce the intensity below that required to maintain the accelerating structure after only a few Rayleigh ranges. Laser systems used in LWFA experiments commonly have $\lambda = 800\,\text{nm}$ and a spot size of 10s of micrometres, so a Rayleigh range may only be between a few hundred micrometres and a millimetre. However, in reality relativistic self-focusing extends the length over which a sufficiently powerful laser pulse remains focused.

Many LWFA experiments use de Laval nozzle gas jets as a plasma source [77], which are ionised by the incident laser pulse. Gas jets are a robust target, but offer no additional control over a single laser pulse. Maintaining laser focus can be achieved by propagating the pulse in a pre-formed plasma that guides over multiple Rayleigh ranges [78]. This can be facilitated by an initial laser pulse that ionises the gas target, creating a radial plasma density profile. Since the refractive index of a plasma depends on its density, there will be a corresponding refractive index profile that effectively focuses the main pulse, in a similar manner to an optical fibre. A pre-plasma may also be formed with high voltage discharges: capillary discharge waveguides [79, 80], which make use of temperature gradients to produce a radial plasma density and refractive index profile, are a successful and widely used method to obtain the very highest LWFA beam energies.

Optical guiding is also possible with hydrodynamic optical-field-ionised (HOFI) channels [81], which, because of their isolation from any physical structure, are resistant to damage from the incident laser pulse – a limiting factor for the operational repetition rate of capillary discharge waveguides. Therefore, HOFI channel-guided LWFAs provide reproducible electron beams at high repetition rates, useful for many applications. Dephasing of injected electrons occurs since as they are accelerated $v_z \to c$, and as a result electrons outrun the accelerating phase of the plasma wakefield, which propagates at

$v_\phi = v_{g,las} < c$. For an electron with $v_z \sim c$ the condition for it to slip by half a plasma wave period is $(1 - v_\phi/c)L_d = \lambda_p/2$ where L_d is the dephasing length. The distance over which the energy of the laser driver with duration τ is depleted, known as the pump depletion length L_{pd}, is found by comparing the laser pulse energy E_L with that expended in exciting the accelerating field E_z: $E_z^2 L_{pd} \simeq E_L^2 \tau$. In the case $a_0 >> 1$ [74]:

$$L_d \simeq \frac{\lambda_p^3 \sqrt{2} a_0}{2\lambda^2 \pi N_p}, \tag{2.69}$$

$$L_{pd} \simeq \frac{\lambda_p^3 \sqrt{2} a_0}{\lambda^2 \pi}, \tag{2.70}$$

where N_p is the number of plasma periods behind the driving pulse. As L_d and L_{pd} are proportional to the plasma wavelength, LWFAs can achieve higher final beam energies by operating at lower plasma density. This must be weighed against the accelerating gradient, since $E_0 \propto \sqrt{n_e}$.

2.3.3 Regimes of laser-plasma interaction

A laser pulse will resonantly drive a plasma wave, producing a maximum wave amplitude when $\tau \simeq \lambda_p/2$. For a plasma with an electron number density $n_e = 10^{18}\,\text{cm}^{-3}$ this requires a laser pulse with a duration of 55 fs. With the available laser technology of the 1980s, when high intensity laser-plasma interaction experiments began, it was challenging to produce a single pulse with this duration [82]. A solution was to use two co-propagating laser pulses of a longer duration that would interfere to produce a new profile consisting of multiple pulses, each with a duration short enough to allow resonant excitation of a plasma wave. This optical beatwave mechanism was originally studied as a method for plasma heating in laboratory fusion devices [83], but in the context of particle accelerators became known as the plasma beat-wave accelerator

(PBWA) [84]. It requires that the frequencies ω_1 and ω_2 of the two interacting laser pulses satisfy the resonance condition $\omega_2 - \omega_1 = \Delta\omega = \omega_p$. In PBWA experiments a maximum longitudinal electric field of $1\,\mathrm{GVm}^{-1}$ was measured in a plasma with a density of around $\sim 10^{17}\,\mathrm{cm}^{-3}$. Using a PBWA externally injected electrons from a conventional accelerator were accelerated to at least $9.1\,\mathrm{MeV}$, having been subjected to an average gradient of $0.7\,\mathrm{GVm}^{-1}$ [85]. However, the bunch length of such an injected electron beam extends over multiple wakefield phases and consequently electron beams produced with the beat-wave scheme were found to have a thermal distribution of energies [84, 85]. Furthermore, the achievable electric field amplitude is limited: with increasing plasma wave amplitude the electron quiver motion becomes relativistic and their mass increases by a factor γ; a falling plasma frequency results in the beat-wave pulse profile being taken out of the resonance condition.

With advances in the available intensity of laser pulses, a new scheme could be considered where the envelope of a laser pulse would become automatically modulated into a train of shorter pulses, each with a length on the order of λ_p. This occurs due to the pulse's interaction with underdense plasma, and is known as the self-modulated LWFA (SM–LWFA) [86]. The advantage of this scheme was that greater electric field amplitudes could be reached and the wavebreaking limit E_0 exceeded, enabling a new mechanism that self-injected electrons from the background plasma into the accelerating wakefield. Conditions for SM–LWFA are a pulse length L only a few times longer than λ_p, or $L \geq c/\omega_p$, and for it to deliver a power to the plasma greater than the critical value for self-focusing in equation (2.66). Envelope modulation of a laser pulse (ω) is both the result of alternate focusing and defocusing forces in the plasma wave it excites (ω_p), and the beating between the laser pulse and two Raman forward scattered waves; they are comprised of a Stokes $(\omega - \omega_p)$ and anti-Stokes $(\omega + \omega_p)$ wave, into which the laser pulse partly decays. A feedback mechanism then increases the laser envelope modulation and amplitude of the

excited plasma wave.

Experiments using 25 TW, 0.8 ps duration laser pulses, focused to an intensity of 6×10^{18} Wcm^{-2}, reached the SM-LWFA regime [87] and electrons injected into the accelerating electric fields via wavebreaking were left with a spectrum of energies that ranged up to 44 MeV. This maximum electron energy corresponds to a peak electric field of over 100 GVm^{-1}. Further experiments throughout the 1990s demonstrated electron acceleration with SM-LWFA [88, 89, 90], and ultimately accelerating gradients over 200 GVm^{-1} and beam energies of 94 MeV and were achieved [14], although with a very broad distribution of energies – in contrast to conventionally accelerated electron bunches that typically had per cent level energy spread [91].

LWFA using a single pulse with an unmodulated Gaussian envelope was made possible with the adoption of chirped-pulse-amplification (CPA) [15] in laser systems. With a laser intensity of $a_0 > 1$ the quiver motion of electrons becomes relativistic. As the laser has a Gaussian transverse profile the intensity and therefore relativistic electron mass varies across the pulse profile; the plasma wavelength is longest on-axis and shortest towards the wings of the laser pulse. Nonlinear plasma waves with curved and steepened wavefronts are therefore formed, resulting in an ion cavity behind the laser pulse with very low or zero electron density. This form of laser-plasma interaction is called the nonlinear bubble or blow-out regime [92] and results in a wakefield that is ostensibly ideal for electron acceleration. In the high intensity limit $a_0^2 >> 1$, the blow-out regime requires an laser spot size $w_0 \leq (2/k_p)\sqrt{a_0}$. Assuming a fully blown-out ion cavity with a relativistic phase velocity and maximum radius R follows a driving laser pulse, the longitudinal E_z (accelerating) and transverse E_r (focusing) electric fields are given by [74]

$$E_z \simeq \frac{k_p \xi}{2} E_0, \tag{2.71}$$

73

$$E_r \simeq \frac{k_p r}{4} E_0, \tag{2.72}$$

where k_p is the wave vector associated with the plasma wavelength λ_p, $\xi = z - ct$ is the co-moving coordinate with respect to the laser pulse, and r is the radial coordinate. E_0 is the wavebreaking field. The maximum value of E_z is reached for $\xi = R$. Because the focusing field E_r is linear as a function of radius r, and does not vary longitudinally within the ion cavity, it enables the preservation of the emittance of an electron beam trapped within it. The accelerating field increases as a function of distance behind the laser driver, which introduces an energy chirp for an electron bunch of finite length. The energy spread may be compensated by modifying the longitudinal electron bunch distribution, thereby beam loading the accelerating field [93]. Bunches with a triangular longitudinal shape may exactly cancel the longitudinal variation in accelerating field E_z, resulting in a completely uniform accelerating field that would impart no additional absolute energy spread. Short-duration particle bunches can result in poor beam loading and large energy spreads, while Gaussian beams can approximately load an accelerating field without excessive increase energy spread, although not as well as a triangular bunch.

Figure 2.8 shows a particle-in-cell simulation of an LWFA in the blow-out regime, with a trapped electron beam of sufficiently high beam current to drive a local plasma wave and therefore alter the accelerating wakefield driven by the laser pulse. Because this bunch has a short duration and therefore a high beam current it overloads the accelerating field, which would result in a large energy spread. In 2004 three groups demonstrated the first experimental demonstration of the nonlinear bubble regime simultaneously [95, 96, 97], which all produced electron beams with a significantly smaller energy spread than prior LWFA experiments. These results were an important milestone in demonstrating the potential of plasma accelerators, however they also high-
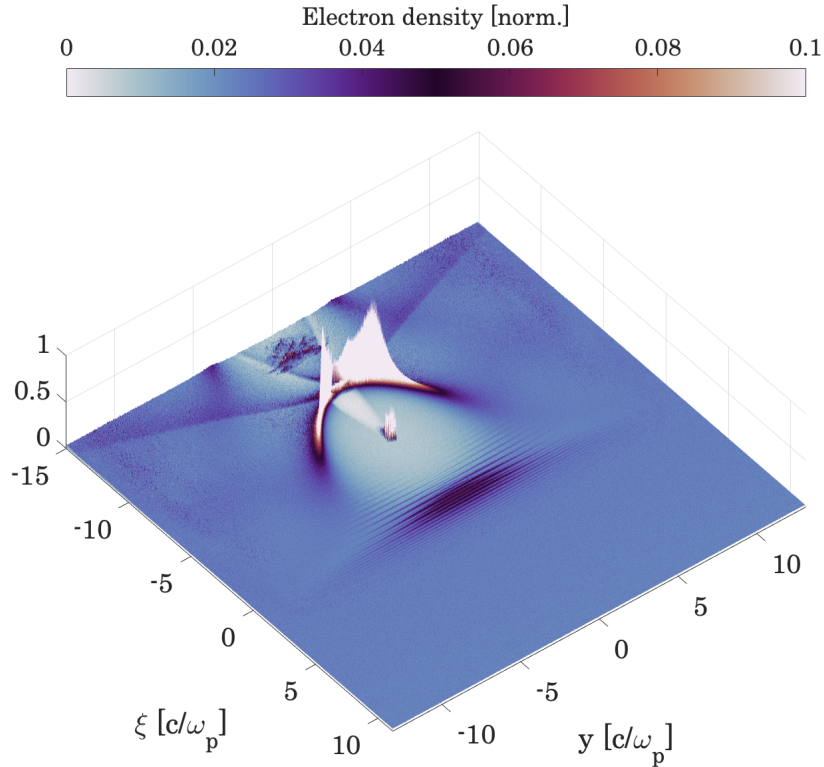
Figure 2.8: A particle-in-cell simulation, produced with the code EPOCH [94], show-ing a laser pulse ($a_0 \sim 2$) driving a high-amplitude, nonlinear plasma wave. The coordinate $\xi = z - ct$ is co-moving with the peak intensity of the laser pulse. The plasma electron number density is normalised to 1, and the colourmap has been trun-cated at 0.1 in order to highlight lower density features.

lighted the progress that was still to be made towards beam properties com-parable with conventional accelerators. Mangles et al. (2004) [95] observed a 70 MeV, 22 pC electron bunch with $\pm 3\%$ relative energy spread, an electron beam of unprecedented high quality for LWFA, but one that was challenging to produce reliably. Most LWFAs are now operated with a single short duration and high intensity laser pulse, however the method of charge injection into the accelerating wakefield varies widely and this has a definitive impact on final beam properties.

2.3.4 Injection methods

When a nonlinear plasma wave exceeds the wavebreaking limit E_0 large quantities of electrons can enter the wakefield and gain energy. However, the wakefield will not persist if the limit is greatly exceeded and the wakefield structure is destroyed during the process of wavebreaking. If the wavebreaking limit is approached with carefully selected laser parameters charge may be injected without the break up of the plasma wave [98]. The controlled used of wavebreaking for charge injection is known as self-injection, which can produce quasimonoenergetic electron beams, such as those seen by Mangles et al. [95].

Because it relies on a nonlinear regime of laser-plasma interaction, the threshold at which self-injection is observed becomes difficult to quantify or control and is vulnerable to fluctuations in the laser driver. This can result in widely varying beam parameters, particularly the amount of charge in the accelerated electron beam and its peak energy. Despite this self-injection remains an attractive method since experiments have produced prominently peaked GeV-scale electron spectra with up to hundreds of pC in charge [99] or sub-mrad divergence [100], using technically straightforward plasma sources. This is in relative contrast to other LWFA injection methods, which may require synchronisation of multiple laser pulses, or the use of specifically tailored gas jets.

Plasma sources for laser wakefield accelerators use a neutral gas with a low atomic number Z, such that the ionisation potential is low, allowing a laser pulse to fully ionise the gas. For example, the ionisation potential of Hydrogen is $15.43\,\text{eV}$ [101] and would be fully ionised well before the peak intensity of a high intensity laser pulse. Electrons occupying core states in atoms of a higher Z gas have ionisation potentials much greater than that of Hydrogen, and if one is chosen that corresponds to the laser peak intensity, plasma electrons can be generated near to the accelerating phase and will become directly trapped,

known as ionisation injection. In this way a region of 99% Hydrogen doped with 1% of a high Z gas, such as Nitrogen, that sits within an otherwise pure Hydrogen gas will trigger a localised ionisation injection. Originally this method was conceived [102] with two separate laser pulses: a pump pulse to pre-ionise the low Z background and drive plasma waves, and an injection pulse to ionise the high Z dopant and inject the liberated electrons into the accelerating phase of the wakefield. The concentration of the high Z dopant and the length of the doped region determines the amount of trapped charge, as injection begins and ends at its boundaries. This prescriptive condition for injection leads to highly reproducible beam charge. Since electrons injected at the start of the region will be accelerated for a longer distance than those at the end, the region must be short to limit energy spread [103]. Ionisation induced injection was shown to significantly increase the charge trapped and accelerated compared with a pure gas plasma source [104], although the energy spectra were relatively continuous due to the length of the doped region. More recently ionisation injection has successfully been demonstrated with a reduced energy spread, when used in combination with an additional injection technique [105], a tailored plasma source [106] or with initially unmatched laser pulses, known as self-truncated ionisation injection [107, 108].

Separating the roles of plasma wave excitation and electron injection between multiple lasers pulses enables more control over the injection process. One method [109], relies on two orthogonally propagating laser pulses. A pump pulse drives a wakefield in the plasma that is intersected at a right angle and a later time by a second injection pulse, with a spot size and duration less than the plasma wavelength. The ponderomotive force of the injection pulse will pre-accelerate a number of bulk plasma electrons so they can become trapped in the plasma wakefield. Because of the relatively small dimensions of the injection pulse, trapping is localised in the accelerating phase, minimising energy spread as the trapped electrons continue to propagate and are accelerated by

the pump pulse. Another optical injection scheme using a pump pulse and the beatwave of two pulses colliding in the wakefield accelerating phase was investigated but never experimentally demonstrated [110, 111]. Optical injection with the collision of two counter-propagating laser pulses with the same frequency was suggested as an alternative [112] and using this method, acceleration of a high quality electron beam was seen in experiment [113]. The relative timing between the pump and injection pulse provided control over the final beam energy, whereas the amount of charge injected was determined by the relative polarisation of the laser pulses. A promising optical technique is the plasma photocathode injection scheme [114, 115], which theoretically features ultra-low transverse emittance due to the fact that injected electrons are tunnel-ionised directly within a pre-existing wakefield with very low transverse momenta, before rapid acceleration to relativistic energies. In the future such a technique could surpass the six-dimensional brightness of conventional light sources. As with all optical injection schemes precise timing of multiple laser pulses is fundamental to the success of a plasma photocathode injector.

Introducing a density gradient in the plasma source also provides a method of controlled injection [116]. The plasma wavelength λ_p is increased as the plasma density is reduced. This means the phase velocity of the wakefield falls, and consequently the velocity required for electrons to become trapped is lowered, triggering injection. Control of this injection threshold is therefore achieved with the density profile of the plasma source. Experimentally, bunches with parameter stability over hundreds of shots are generated [117]. Significantly the normalised emittance was found to be 0.63-1.3 mm mrad, an order of magnitude improvement over LWFA electron beam emittances seen up to that point. A rapid downward density transition has also been successfully implemented as a source of stable LWFA electron beams with tuneable energy [118, 119], which is studied in Chapter 5 as a novel electron injector for AWAKE Run 2.

2.3.5 Current state-of-the-art

Table 2.1: Best reported LWFA beam parameters. Adapted from Downer et al. [120] (superscript ∗ indicates bi-dimensional transverse emittance that assumes radial symmetry)

Bunch Property	Best Reported	Citation
Q (nC)	0.5	Couperus et al. 2017 [121]
E (GeV)	7.8	Gonsalves et al. 2019 [122]
$\Delta E/\langle E \rangle$ (FWHM)	0.01	Rechatin et al. 2009 [19]
ε_n^* (mm mrad)	0.1	Plateau et al. 2012 [123]
σ_z (µm)	0.48	Lundh et al. 2011 [124]
Rep. Rate (kHz)	1	Salehi et al. 2017 [21]

State-of-the-art LWFA beam properties achieved to date are shown in table 2.1. Each value was from an independent experiment. Achieving all simultaneously is an extant challenge, although progress is rapid and LWFAs are now transitioning from proof-of-principle experiments that demonstrate electron acceleration to those aimed at producing a high quality, and usable, electron beam.

2.4 Principles of Beam-driven Plasma Wakefield Acceleration

2.4.1 Regimes of beam-plasma interaction

A beam of charged particles can also be used to excite plasma waves for particle acceleration, however the mechanism that drives charge separation between plasma species originates in the space-charge force of the particle beam, rather than the ponderomotive force of a laser pulse. This is known as the plasma wakefield accelerator (PWFA), proposed by a group at UCLA and SLAC [11],

and experimentally demonstrated [125] with the Advanced Accelerator Test Facility at Argonne National Laboratory (ANL) in the late 1980s. A bunch of electrons propagating in plasma drive plasma oscillations at a frequency ω_p, producing a wakefield structure consisting of accelerating (decelerating) and focusing (defocusing) electric fields that are $\pi/2$ out of phase with each other, as discussed in section 2.2.3.

An important figure of merit for PWFA is the transformer ratio: this quantity is the ratio of peak accelerating gradient in the wakefield to the peak decelerating gradient felt by the driver, i.e. the efficiency of energy transfer between the driver and the plasma wave. It is ideally large to maximise energy gain of the witness bunch for a given driver energy. Originally this was investigated in the context of an electron driven linear accelerator [126], a progenitor to the CLIC scheme using wakefields in metallic cavities to accelerate witness particle bunches. The transformer ratio was found not exceed a value of two for Gaussian driver and witness bunches. Beyond this value the peak particle energy stops increasing since the particle distribution is altered as maximally decelerated particles begin to be lost from the beam. For an accelerating structure with multiple electric field modes the maximum transformer ratio may be increased beyond two if the accelerating potentials of each mode are superimposed coherently behind the driving bunch. The transformer ratio can also be increased in a single mode structure, such as a plasma, by modifying the profile of the drive bunch: a triangular longitudinal profile with a larger population at the peak decelerating field that falls to a constant value will allow beam loading of the wakefield, flattening it and making the decelerating potential uniform across the bunch [127].

Because of the high momentum of a relativistic driving bunch the principle energy limit in PWFA is driver depletion, where no more energy can be extracted by the witness bunch. Consequently the transformer ratio is an im-

portant consideration for PWFA energy gain. From the linear two-dimensional theory of PWFA the longitudinal accelerating electric field generated by a drive bunch of N_b electrons with an r.m.s. length and width of σ_z and σ_r respectively is approximately [128]:

$$E_z[\text{MVm}^{-1}] = 244 \frac{N_b}{2 \times 10^{10}} \left(\frac{600}{\sigma_z[\text{\textmu m}]} \right)^2 \qquad (2.73)$$

Such an electric field is generated assuming $\sigma_r/\lambda_p \ll 1/2\pi$ and when $\sigma_z/\lambda_p \simeq 1/\sqrt{2}\pi$. The ratio of bunch to plasma density is analogous to the peak normalised vector potential a_0 in LWFA, i.e. it characterises the plasma's threshold of nonlinear response. The linear equation above is only valid when $n_b/n_e \ll 1$. To increase E_z further requires a reduction of σ_z or an increased N_b, which implies a higher bunch density. In this case $n_b/n_e \gg 1$ and plasma electrons are completely expelled from the propagation axis, leaving an ion cavity behind the drive bunch. This is the PWFA nonlinear blowout regime [129], in which multi GVm^{-1} accelerating gradients are possible. The nonlinear blow-out regime in PWFA requires that $n_b/n_e \gg 1$, $k_p\sigma_z < 1$, and $k_p\sigma_r < 1$, and produces the same transverse and longitudinal electric fields as discussed in section 2.3.3 that permit emittance preservation and uniform acceleration with beam loading.

2.4.2 PWFA experiments

Owing to the parameter constraints on the drive beam, needed to excite non-linear plasma waves and obtain the highest accelerating gradients in PWFA, namely high energy and charge, small beam size, and short duration, beam-driven plasma acceleration experiments have been focused at national laboratories with a large and well established accelerator infrastructure. Early demonstrations of PWFA conducted at ANL used an electron driver in both the linear [125] and nonlinear regimes [130], fielding longitudinal wakefield am-

plitudes up to $5.3\,\mathrm{MVm^{-1}}$. Throughout the 1990s work focused on optimising the nonlinear regime of operation [131], as well as the stable propagation of the driver [132, 133]. These developments were important to the operation of PWFAs over longer distances, enabling higher peak energies and preservation of witness beam quality. A series of PWFA experiments at the Stanford Linear Accelerator Centre (SLAC) began with E-157 [134], with the goal to generate a $\mathrm{GVm^{-1}}$ accelerating gradient in a metre scale plasma cell. A single $30\,\mathrm{GeV}$ electron bunch was used to drive a wakefield in a $1.4\,\mathrm{m}$ long plasma cell with density $2 \times 10^{14}\,\mathrm{cm^{-3}}$ [135]. In this scheme the head of the bunch excites the plasma wave and loses energy, while the tail witnesses the wakefields and is accelerated. This, along with E-162, a similar experiment using a single positron bunch, observed accelerating fields of $150\,\mathrm{MVm^{-1}}$. Due to their opposite charge, positrons excite a plasma wave in a fundamentally different way with respect to an electron beam, with plasma electrons instead streaming toward the driving positron bunch before oscillating about an equilibrium position.

A third generation PWFA experiment at SLAC, E-164, was conducted in 2003 [136]. With a smaller spot size at the plasma cell a higher density driver was able to increase the energy of witness electrons by $2.7\,\mathrm{GeV}$ in a $10\,\mathrm{cm}$ plasma cell [137], however the absolute energy spread ΔE of the accelerated electron beam was increased from $\sim 1\,\mathrm{GeV}$ to $\sim 7.5\,\mathrm{GeV}$. Later experiments showed energy doubling of some $42\,\mathrm{GeV}$ electrons [12], implying a large gradient of $52\,\mathrm{GVm^{-1}}$. However, as the witness electrons originate from within the driving beam, the quantity of accelerated charge is relatively low and has a broad distribution of energies. Following single bunch PWFA, a new group of experiments at the Facility for Advanced aCcelerator Experimental Tests (FACET) at SLAC made use of independent witness and driver bunches, produced by physically cleaving one bunch into two. If the witness bunch is left at the correct phase of the wakefield, and with enough charge to load it, an

efficient and large energy gain results. At FACET a $74\,\mathrm{pC}$ bunch accelerated by $1.6\,\mathrm{GeV}$ was found to have an average energy spread of $4\,\%$, having gained this energy from the plasma wake with an efficiency of $30\,\%$ [23]. This quasi-monoenergetic acceleration was an important step towards the application of PWFA for a linear e^-e^+ collider – firstly because efficiency is an important consideration for the operational cost and repetition rate of such a machine, and secondly because large energy gains in a single stage imply fewer are needed, reducing the complexity of the design. Another consideration for a PWFA-based e^-e^+ collider is an equally viable source of positrons.

High-gradient positron acceleration has been demonstrated [138] using a single bunch that loads its own wakefield with a self-generated and distinct witness bunch originating in the tail. This bunch had a charge of $210\,\mathrm{pC}$ and gained $5\,\mathrm{GeV}$ in $1.3\,\mathrm{m}$, with an efficiency of $34\,\%$, and had percent level energy spread. The energy gain varied between shots however, from $3\text{-}10\,\mathrm{GeV}$. Due to the asymmetric response of plasma electrons to electron and positron drivers, strong nonlinear transverse fields can lead to unwanted deterioration of the positron beam emittance. Positron-driven PWFA in a hollow plasma channel, also demonstrated at FACET [139], could well be a solution: the annular plasma results in zero transverse fields within the channel, thereby removing their adverse effect on positron beam emittance.

2.4.3   Current state-of-the-art

State-of-the-art electron and positron-driven PWFA beam properties that have been achieved to date are shown in table 2.2. Significant outstanding issues towards the application of PWFA in a plasma-based collider are optimising the transformer ratio to enable larger per-stage energy gains and improve overall efficiency, demonstrate preservation of beam emittance throughout acceleration over multiple plasma stages, and, crucially for an e^-e^+ collider, demonstrate

83

Table 2.2: Best reported e^- and e^+-driven PWFA beam parameters from the FACET experiments. Adapted from a talk given by Mark Hogan, ANAR2017 Workshop

Bunch Property	Electrons	Positrons
Q (nC)	0.074	0.21
Energy gain (GeV)	9	4.4
$\Delta E / \langle E \rangle$ (r.m.s.)	0.04	0.02
Peak gradient (GVm^{-1})	6.9	3.4
Efficiency of energy gain %	30	34
$\varepsilon_{x,n}$ (mm mrad)	32	n/a
$\varepsilon_{y,n}$ (mm mrad)	n/a	n/a
Rep. Rate (Hz)	10	10

an equivalent source of high quality and high energy positrons. The beam emittance marked n/a in table 2.2 are not included as they were either not preserved or increased during the acceleration process.

2.5 Summary

In this chapter, a review of conventional and novel accelerator concepts has been used to lay out the context in which the rest of this thesis is presented. The capabilities of different LWFA systems, i.e. different driving laser and plasma source configurations, have been summarised via recent experimental results, and are used to select an appropriate LWFA system that can satisfy the requirements of the AWAKE Run 2 electron injector in Chapter 5. In the next chapter, a framework for the motion of electron beams in ion channels is established, which will be used in Chapter 6 and Chapter 7 to provide an analytical description of synchrotron radiation emission and the electron beam dynamics during acceleration in a plasma wakefield.

Chapter 3

Electron Orbits in Ion Channels

3.1 Single-electron Motion

If a particle or laser beam driver fully evacuates the electrons from the plasma cavity that it creates, the electric field in the cavity may be modelled with a pure ion channel surrounded by a bulk plasma. Electrons in ion channels are accelerated by a longitudinal electric field E_z, and oscillate in a direction perpendicular to the axis of acceleration as a focusing force E_r works against their finite transverse momenta. The sign of E_z is such that a negatively charged electron gains energy. The longitudinal equation of motion for a single electron is then

$$\frac{dp_z}{dt} = \frac{d\gamma m_e v_z}{dt} = eE_z, \qquad (3.1)$$

$$\frac{d\gamma}{dt} = \frac{eE_z}{m_e v_z}. \qquad (3.2)$$

For an ultra-relativistic electron ($v_z \sim c$) the energy evolution may be expressed as

$$\frac{d\gamma}{dt} = \omega_p \frac{E_z}{E_0}, \tag{3.3}$$

where $E_0 = m_e \omega_p c/e$, i.e. equation (2.55), in the ultra-relativistic case. The radial focusing electric field E_r in the case of a fully blown-out ion channel may be found by considering the channel as an arbitrarily long, infinitesimally thin cylinder of charge that encloses only plasma ions, and outside of which lays both plasma electrons and ions. With the integral form of Gauss' law

$$\oint_S \vec{E} \cdot d\vec{S} = \int_V \frac{\rho}{\varepsilon_0} d\vec{V}, \tag{3.4}$$

where $\vec{E}$ is the electric field within the cylinder, $d\vec{S}$ is a surface element of its total area S, $d\vec{V}$ is a volume element of its total volume V, and $\rho = en_e$ is the charge density on the surface for a plasma with electron number density n_e. Since $\vec{E}$ and $d\vec{S}$ point in the same direction, and $\vec{E}$ is isotropic, the radial electric field is

$$E_r 2\pi r L = \frac{\rho}{\varepsilon_0} \pi r^2 L, \tag{3.5}$$

$$E_r = \frac{en_e}{2\varepsilon_0} r, \tag{3.6}$$

for a cylinder of surface area $S = 2\pi r L$ and volume $V = \pi r^2 L$, as shown in figure 3.1. By symmetry the horizontal transverse field in an ion channel is $E_x = (en_e/2\varepsilon_0)x$, and the equation of motion in the horizontal plane for an electron within the ion channel is

$$\frac{dp_x}{dt} = -eE_x. \tag{3.7}$$

Expanding in terms of the horizontal coordinate x:
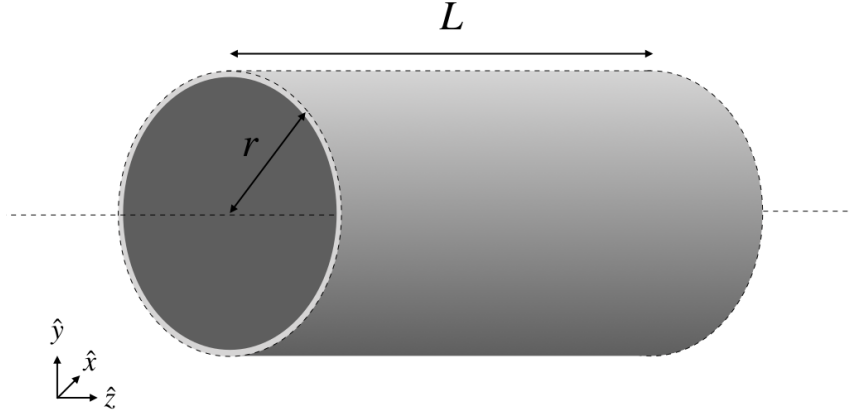
Figure 3.1: *An ion channel in a plasma represented as a cylinder of charge.*

$$\frac{d\gamma v_x}{dt} = -\frac{e^2 n_e}{2 m_e \varepsilon_0} x, \tag{3.8}$$

$$\frac{d^2 x}{dt^2} + \frac{1}{\gamma}\frac{d\gamma}{dt}\frac{dx}{dt} + \frac{\omega_p^2}{2\gamma} x = 0, \tag{3.9}$$

with $v_x = dx/dt$ and $\omega_p = \sqrt{n_e e^2 / m_e \varepsilon_0}$ from equation (2.43). In the case of zero acceleration $(d\gamma/dt = 0)$, the solution is sinusoidal oscillatory motion $x(t) = x_{\beta_0} cos(\omega_\beta t)$ with an amplitude x_{β_0} and frequency $\omega_\beta = \omega_p/\sqrt{2\gamma}$ known as the betatron frequency. Conversely, if the energy is increasing, as in the case of acceleration, the betatron frequency will evolve as it is a function of $\gamma(t)$. Furthermore during acceleration the ratio p_x/p_z becomes smaller leading to adiabatic damping of the betatron amplitude, as we have seen for the case of a beam in section 2.1.1. Because the time t' of a betatron oscillation is fast compared to the time t during which the frequency and amplitude of the oscillation changes, a solution to equation (3.9) may be found with the WKB approximation [140]

$$x(t) = x_{\beta_0} \sqrt{\omega_\beta(t)} \cos\left(\int_0^t \omega_{\beta(t')} dt'\right). \tag{3.10}$$

The amplitude $x_\beta(t) = x_{\beta_0}\sqrt{\omega_\beta(t)}$ and frequency ω_β of betatron motion

therefore scale as $\gamma^{-1/4}$ and $\gamma^{-1/2}$ respectively. Figure 3.2 shows the transverse motion of an electron both in an accelerating field $E_z = 0$ and $E_z/E_0 = 0.46$, within a plasma of density $n_e = 1 \times 10^{18}\,\mathrm{cm}^{-3}$. It has an initial position $x_{\beta_0} = 1.325\,\mu\mathrm{m}$, $\gamma_0 = 100$, and propagates for 10 betatron periods $\lambda_{\beta_0} = 2\pi c/\omega_{\beta_0}$ with respect to the initial energy.
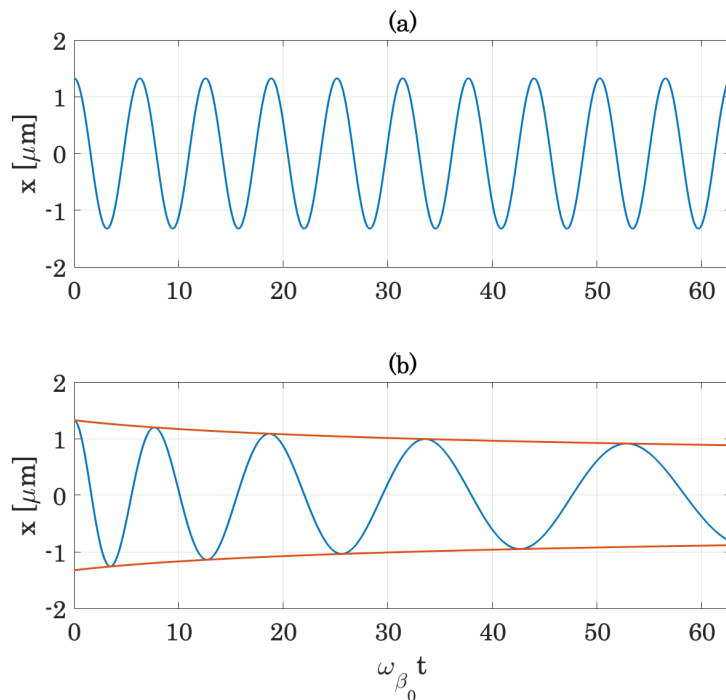
Figure 3.2: The transverse motion of an electron in an ion channel, shown both in the case $E_z = 0$ (a) and $E_z > 0$ (b).

The strength of transverse oscillation of an electron is characterised by the dimensionless parameter [141]

$$\alpha_\beta = \gamma k_\beta x_\beta, \tag{3.11}$$

where γ is the Lorentz factor of the electron, $k_\beta = k_p/\sqrt{2\gamma}$ is the betatron wavenumber, and x_β is the betatron amplitude. The parameter α_β is analogous to the wiggler strength parameter α of insertion devices. For an insertion

device α is determined solely by the external magnetic field and has the same value for all electrons, whereas in an ion channel each electron has a different α_β that depends on its energy through γ and initial transverse position x_0. Furthermore, in a plasma wakefield electrons may gain or lose energy. This results in a range of α_β values for a beam with finite energy spread and a distribution of betatron amplitudes.

3.2 Beam Motion

For an electron beam with a Gaussian transverse profile the ensemble average betatron amplitude $\langle x_\beta \rangle$ is proportional to the r.m.s. beam size in the transverse horizontal direction σ_x, within which most electron trajectories are contained. Single electron orbits are then confined within boundary of a beam size σ_x that evolves through a wakefield, known as the beam envelope. Assuming no external forces other than the focusing field E_r, an electron beam size σ_x in a fully blown-out ion channel evolves according to the envelope equation [142]

$$\frac{d^2\sigma_x}{dz^2} + \frac{k_p^2}{2\gamma}\sigma_x - \frac{\varepsilon_n^2}{\gamma^2\sigma_x^3} = 0. \tag{3.12}$$

The second and third terms account for focusing due to the ion column and outward pressure of the beam emittance respectively. The two balance when the condition $(d\sigma_x/dz)_{z=0} = 0$ is met, which is satisfied for a beam size

$$\sigma_{x,m}^2 = \left(\frac{2\varepsilon_n^2}{\gamma k_p^2}\right)^{\frac{1}{2}}, \tag{3.13}$$

known as the matched size. Electron beams injected into a plasma ion channel undergo envelope oscillations between the initial and matched beam radii. If injected with the matched value a beam will continue to propagate at this

size in the absence of additional extra or intra-beam forces, e.g. acceleration or radiation reaction. In the case of acceleration the beam size will be adiabatically damped, but if the beam is initially matched the normalised emittance ε_n will be preserved throughout acceleration; the effects of radiation reaction on the evolution of beam parameters are discussed in Chapter 7.

3.3   Synchrotron Radiation from Ion Channels

Electron beams in ion focusing channels emit synchrotron radiation whose spectral characteristics are determined by the distribution of single-electron orbits within the beam envelope [143, 141], known experimentally as betatron radiation. A general expression for the radiation emitted by an electron oscillating in an ion channel is found by substituting its trajectory, such as those described in section 3.1, into the Liénard-Wiechert fields [144]. The energy emitted into a direction $\vec{n}$ by an electron, as a function of its position, velocity, and acceleration along its trajectory, is then given by [145]

$$\frac{d^2 I}{d\omega d\Omega} = \frac{e^2}{16\pi^3 \varepsilon_0 c} \times \left| \int_{-\infty}^{+\infty} e^{i\omega[t-\vec{n}\cdot\vec{r}(t)/c]} \frac{\vec{n} \times [(\vec{n} - \vec{\beta}) \times \dot{\vec{\beta}}]}{(1 - \vec{\beta} \cdot \vec{n})^2} dt \right|^2 , \qquad (3.14)$$

where the energy is emitted within a spectral bandwidth $d\omega$ about a frequency ω, into a solid angle $d\Omega$ about the direction $\vec{n}$. The electron position at time t, and velocity normalised to the speed of light in vacuum c, are $\vec{r}(t)$ and $\vec{\beta}$ respectively. Equation (3.14) assumes observation in the far field, such that the direction of observation $\vec{n}$ may be considered constant for the entirety of the electron's trajectory.

3.3.1 Spectral Characteristics

The fundamental frequency $\omega = 2\pi c/\lambda$ of the radiation described by equation (3.14) is derived from the betatron wavelength λ_β, which is both Lorentz contracted in the laboratory frame due to the emitting electron's energy by a factor γ^2, and Doppler shifted with respect to a polar observation angle θ from the axis of acceleration [145]:

$$\lambda \simeq \frac{\lambda_\beta}{2\gamma^2}\left(1 + \frac{\alpha_\beta^2}{2} + \gamma^2\theta^2\right) \tag{3.15}$$

For $\alpha_\beta \ll 1$, the emission is comprised of a few low-order harmonics of λ_1. In this case particle motion is in the undulator regime: the electron radiates in the same direction at all times during its orbit. Spatially, the emission is collimated along the propagation axis, falling within an angle $\theta \sim 1/\gamma$. As α_β increases above unity the electron begins to emit in the wiggler regime, i.e. in different directions at different times in its orbit, which contributes an increasing number of finite-width harmonics of λ that fall in a broader angle $\theta \sim \alpha_\beta/\gamma$. For $\alpha_\beta \gg 1$, the presence of many high-order harmonics result in a total spectrum that becomes synchrotron-like, such as the emission from a particle beam that has passed through a dipole magnet, with a shape that can be approximated by the universal function [141]

$$S(x) = x\int_x^\infty K_{5/3}(\xi)d\xi, \tag{3.16}$$

where $K_{5/3}$ is a modified Bessel function of the second kind. Such a spectrum falls exponentially after a critical frequency ω_c, which divides the spectrum into two equal components and, for a relativistic electron in a pure ion channel, may be expressed as [141]

$$\omega_c = \frac{3}{2}\gamma^3 c x_\beta k_\beta^2. \tag{3.17}$$

Electron motion in plasma wakefield accelerators generally results in strong transverse motion where the assumption that $\alpha_\beta >> 1$ is valid. Some acceleration schemes, such as the AWAKE experiment, result in quasi-undulator motion ($\alpha_\beta \sim 1$), which is discussed in Chapter 6.

3.3.2 Radiated Power

The total power radiated by a relativistic electron is found from the Larmor formula [144]

$$P_\gamma = \frac{2e^2}{3c}\gamma^2\left[\left(\frac{d\vec{u}}{dt}\right)^2 - \left(\frac{d\gamma}{dt}\right)^2\right], \tag{3.18}$$

where $\vec{u} = \vec{p}/m_e c$ is the normalised momentum. For the sinusoidal motion described by equations (3.7–3.9) with constant energy ($d\gamma/dt = 0$) the average power radiated over a betatron period is [143]

$$\langle P_\gamma \rangle \simeq \frac{r_e m_e c^3 \gamma^2 k_\beta^2 \alpha_\beta^2}{3} = \frac{r_e m_e c^3 \gamma^4 k_\beta^4 x_\beta^2}{3}, \tag{3.19}$$

where $r_e = e^2/m_e c^2$ is the classical electron radius in c.g.s. units. The energy loss rate per unit distance s for a radiating electron is therefore

$$\frac{dW_{loss}}{ds} = \frac{\langle P_\gamma \rangle}{c} = \frac{r_e m_e c^2 \gamma^2 k_\beta^2 \alpha_\beta^2}{3}, \tag{3.20}$$

and the total energy lost over a number N_β of betatron periods $\lambda_\beta = 2\pi/k_\beta$ is

$$W_{loss} = \frac{\langle P_\gamma \rangle}{c}\lambda_\beta N_\beta = \frac{2\pi}{3}r_e m_e c^2 \gamma^2 k_\beta \alpha_\beta^2 N_\beta. \tag{3.21}$$

Subsequently dividing equation (3.21) by the average photon energy in a synchrotron spectrum $\hbar\langle\omega\rangle = (8/15\sqrt{3})\hbar\omega_c$, and substituting for equation (3.17),

92

the number of photons emitted per electron, per betatron period N_β, and integrated over all angles is [145]:

$$\langle N_\gamma \rangle = \frac{5\sqrt{3}\pi}{6} \frac{r_e m_e c \alpha_\beta^2}{\hbar \gamma x_\beta k_\beta} = \frac{5\sqrt{3}\pi}{6} \alpha \alpha_\beta, \tag{3.22}$$

where $\alpha = e^2/\hbar c$ is the fine structure constant in c.g.s. units.

3.3.3 Quantum Radiation Regime

The classical treatment for synchrotron radiation, presented so far, does not remain valid in all regimes of electron acceleration. If interacting with a sufficiently intense electromagnetic field, quantum effects must be considered. In the classical picture an electron oscillating in an electromagnetic field $(\vec{E}, \vec{B})$ absorbs energy and momentum from it, which can be emitted as synchrotron radiation, known as multiphoton Thompson scattering; in a field of sufficient strength, where quantum effects such as photon recoil influence the radiation mechanism, the process is known as multiphoton Compton scattering. The transition between the two regimes of emission is characterised by the quantum electrodynamics (QED) parameter χ [146]:

$$\chi = \frac{\gamma\sqrt{\left(\vec{E} + \vec{u} \times \vec{B}\right)^2 - \left(\vec{u} \cdot \vec{E}\right)^2}}{E_s} \simeq \frac{\gamma F_\perp}{e E_s} = \frac{\gamma E_r}{E_s} \tag{3.23}$$

where $\vec{u} = \vec{p}/mc$ is the normalised momentum of the electron, γ is its relativistic Lorentz factor, and $E_s = 1.32 \times 10^{18}\,\mathrm{Vm^{-1}}$ is the Schwinger or QED critical field. The classical treatment of radiation reaction is valid when $\chi << 1$, while a quantum radiation model is required for $\chi \geq 1$. Evidence of radiation reaction that conforms to aspects of a quantum model of emission has been shown in all-optical inverse Compton scattering experiments, where an LWFA-generated electron beam collides with a secondary laser pulse [147].

3.4 Summary

All radiating systems presented in this thesis are within the classical radiation regime; the closest to the Quantum regime being the case of a $51\,\mathrm{GeV}$ ($\gamma = 1 \times 10^5$) electron beam accelerated in a plasma of density $n_e = 1 \times 10^{18}\,\mathrm{cm}^{-3}$ where the wavebreaking field $E_0 = 96\,\mathrm{GVm}^{-1}$, shown in section 7.2.1. In this case $E_r \sim 0.1 E_0 = 9.6 \times 10^9\,\mathrm{Vm}^{-1}$ and $\chi \simeq 1 \times 10^{-3}$. This chapter has established the framework for transverse electron motion in a plasma wakefield used throughout this thesis. The next chapter describes numerical methods that are used simulate the interaction of high intensity laser and particle beams with plasma. Numerical simulation is now a fundamental tool in the novel accelerator research community, which complements and extends the experimental and theoretical study of plasma wakefield acceleration.

Chapter 4

Simulation of Plasma Wakefield Acceleration

4.1 The Particle-in-cell Method

Numerical methods may be used when analytical solutions for the equations describing a physical system cannot be obtained, such as in the nonlinear interaction of a high intensity laser pulse with plasma. A plasma contains many particles that have a large and continuous distribution of velocities at different locations. The function $f = f(\vec{r}, \vec{p}, t)$ describes this distribution for a given particle species of the plasma by defining the region in six-dimensional phase space $(\hat{x}, \hat{y}, \hat{z}, \hat{p_x}, \hat{p_y}, \hat{p_z})$ that it occupies. It can be thought of as a probability density, where integrating $f(\vec{r}, \vec{p}, t)$ over a volume of phase space gives the probability of finding a particle within the volume around location $\vec{r}$ with momenta close to $\vec{p}$ at a particular time t. The distribution function evolves according to the Boltzmann equation, taking into account particle collisions or interaction with fields [148]:

$$\frac{\partial f}{\partial t} + \frac{\vec{p}}{\gamma m} \cdot \nabla_r f + \vec{F} \cdot \nabla_p f = C(f) + S(f). \tag{4.1}$$

$\vec{F} = q(\vec{E} + \vec{v} \times \vec{B})$ is the Lorentz force acting particles due to fields, $C(f)$ is the contribution to $f(\vec{r}, \vec{p}, t)$ from particle collisions, and $S(f)$ is a source term to account for ionisation and recombination processes within the plasma that could alter the species population. In the case of a laser-ionised plasma $C(f)$ may be neglected because the time between electron-ion collisions in a plasma is typically longer than the time scale of laser-plasma interaction. The source term $S(f)$ can also be ignored as most lasers have an intensity orders of magnitude greater than the ionisation potential of the neutral gas, and a fully ionised plasma can be assumed. Therefore with $C(f) = 0$ and $S(f) = 0$ the Boltzmann equation reduces to

$$\frac{\partial f}{\partial t} + \frac{\vec{p}}{\gamma m} \cdot \nabla_r f + \vec{F} \cdot \nabla_p f = 0, \tag{4.2}$$

which is known as the Vlasov equation. Using the relevant Maxwell equations:

$$\nabla \times \vec{E} = -\frac{\partial \vec{B}}{\partial t}, \tag{4.3}$$

$$\nabla \times \vec{H} = \vec{J} + \frac{\partial \vec{D}}{\partial t}, \tag{4.4}$$

where $\vec{J}$ is the current density, $\vec{H} = \vec{B}/\mu_r \mu_0$ is the magnetic intensity, and $\vec{D} = \varepsilon_r \varepsilon_0 \vec{E}$ is the electric displacement with the relative magnetic permeability and electric permittivity μ_r and ε_0 respectively. Equation (4.2) and the Lorentz force therefore provide a closed system of equations that govern the behaviour of a given particle species in a collisionless, fully ionised plasma. Differential equations may be solved approximately by exchanging a derivative for a finite difference. By representing the distribution function f with a fixed Eulerian

mesh of points and finite differencing equation (4.2) with respect to time, the evolution of a plasma species over a series of timesteps may be simulated. Such Vlasov simulation codes [149] provide a comprehensive description of a plasma system but in most cases their computational memory requirements are significant. A mesh of just $N = 100$ points along each of the six dimensions in phase space would result in 10^{12} variables, each of which are commonly allocated a 32-bit double precision floating point number, and therefore a significant amount of memory is required to store all the variables. Furthermore, given that the plasma particles of interest occupy a limited region in phase space, and that all the remaining 'empty' points in the numerical arrays making up the distribution function f must still be processed, multi-dimensional Vlasov codes can be highly inefficient with computing resources.

The memory requirements of such a simulation may be reduced by grouping real plasma particles into local clusters of 'macroparticles', each representing many real particles that occupy a finite volume and move together with the same velocity. In this case equation (4.2) may be approximated by a set of finite phase-fluid elements, whose centres follow the familiar equations of motion for a relativistic particle [72]. This is known as the particle-in-cell (PIC) method. It has the advantage that only the region of interest in phase space, i.e. only those fluid elements representing the plasma particles of interest, are tracked in the simulation. A static mesh is still required to solve equations (4.3) and (4.4) but this has only three dimensions in contrast to the full six-dimensional mesh inherent to Vlasov codes. Therefore a PIC code stores the position and momenta of the macroparticles as continuous coordinates, whereas the resultant electromagnetic fields they generate are confined to discrete positions on a fixed Eulerian mesh. Macroparticles are 'pushed' by the electromagnetic fields to new locations with modified momenta, who in turn generate new fields. The particle coordinates and field values are advanced in timesteps from initial conditions using an algorithm, summarised in the flowchart in figure 4.1.
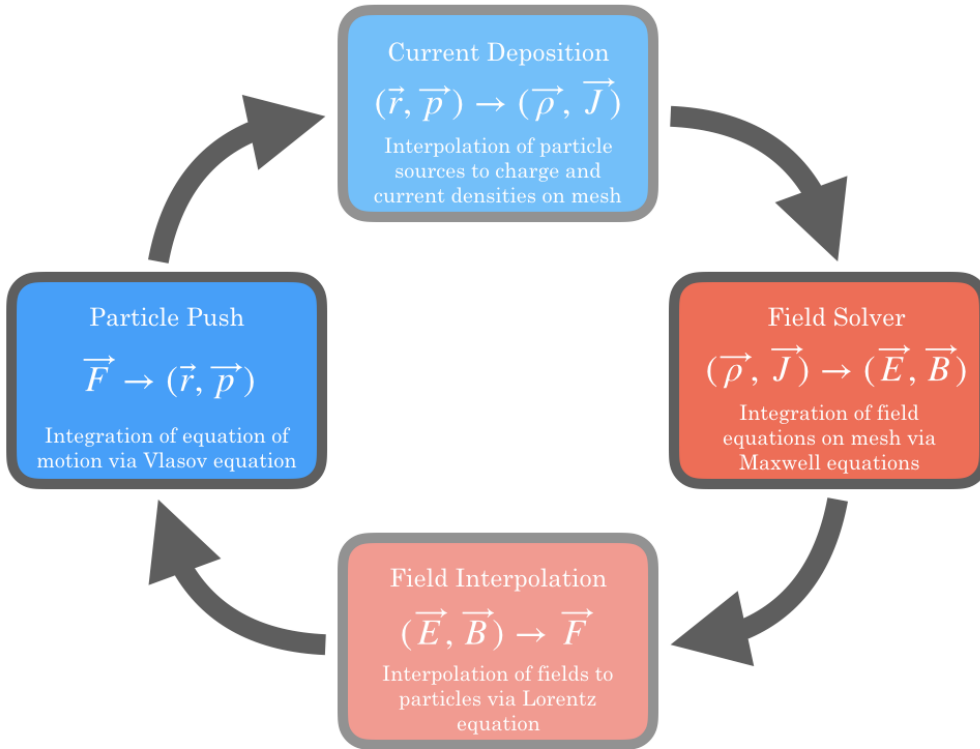
Figure 4.1: A single timestep of the PIC cycle.

4.2   Numerical Stability

Numerical stability is an important consideration for PIC simulations. An unstable simulation can see errors propagate and grow over many timesteps, leading to unphysical results. A fundamental requirement for stability is that the timestep Δt used in the finite-difference solver is shorter than the travel time of light across the width of a mesh cell, such that information is only communicated between adjoining cells. For a mesh cell with three-dimensional size $\Delta x \times \Delta y \times \Delta z$ the timestep must satisfy

$$\Delta t < \sqrt{\Delta x^2 + \Delta y^2 + \Delta z^2}/c, \tag{4.5}$$

which is known as the Courant condition [150]. Electromagnetic waves propagate in vacuum at the speed of light c, where there is no dispersion. However

when the finite-difference method is used to solve the Maxwell equations (4.3) and (4.4) with a discrete cell size numerical dispersion can be introduced. This leads to the numerical Cherenkov instability [151] where particles travel faster than the speed of light in the simulation mesh, placing further constraints on the simulation timestep in order to maintain stability. This effect can be mitigated by smoothing the particle current density that gives rise to the fields, in either time or space [151].

4.3   The Quasi-static Approximation

The operation of plasma accelerators concerns a wide variety of length scales, from the laser wavelength of hundreds of nanometres to metre-scale plasma over which acceleration takes place in PWFA. Future plasma-based colliders could maintain acceleration over multiple kilometres. These disparate scales provide a significant challenge for simulation, but approximations are employed to decrease the computational time without loss of physical accuracy. Particularly relevant for this thesis is the quasi-static approximation. Such an approach decouples the relatively fast timescale of driver evolution from the relatively slow duration of acceleration: it assumes that a driving laser pulse or particle beam does not evolve significantly in a time corresponding to its own length and so the simulation can be advanced in larger timesteps [72]. Since a new wakefield configuration must be calculated for every timestep during which the driver may have evolved, reducing timestep frequency offers a significant increase in simulation speed. Radiation is not included self-consistently in the quasi-static approximation and as such a driving laser pulse envelope must be included analytically via the ponderomotive force, shown in equation (2.64). The quasi-static approximation is used for the simulation studies presented in Chapter 6 and Chapter 7 of this thesis to greatly reduce computational time for long-term acceleration over many metres.

4.4 Simulation Codes

4.4.1 EPOCH

EPOCH is an MPI parallelised, explicit, second-order, relativistic PIC code developed at the University of Warwick for laser-plasma interaction [94]. The code is fully three-dimensional and capable of modelling ionisation processes. It is also possible to implement bespoke density profiles for the plasma electron species. This enabled the introduction of a hydrodynamic shock model used in the simulation study presented in Chapter 5. Version 4.9.0 of EPOCH was used in all presented studies.

4.4.2 QV3D

The 3-dimensional quasi-static PIC code QV3D [72] is built on the framework of Virtual Laser Plasma Laboratory (VLPL) [152], a longstanding code used widely for the simulation of plasma wakefield acceleration. Most PIC simulations do not explicitly model synchrotron-like emission, as the short-wavelength emission cannot be resolved by the simulation mesh. In QV3D the photon energies are calculated from the macroparticle trajectories directly and this is done self-consistently during the particle push, i.e. from the new particle positions. Each macroparticle emits a synchrotron spectrum with a shape given by equation (3.16) along its trajectory, from which the transverse momentum change of the electron is calculated. This change in momentum determines how many photons of that spectrum are emitted in one timestep. Macroparticle momenta are subsequently updated for the following timestep according to the radiated photon energy. The raw spectrum from the code is saved as a critical photon spectrum $N(\omega_c)$; the total betatron spectrum $N(\omega)$ is reconstructed by convolving equation (3.16) with $N(\omega_c)$:

$$N(\omega) = \int_0^\infty S\left(\frac{\omega}{\omega_c}\right) N(\omega_c) d\omega_c. \tag{4.6}$$

Effectively, each energy $\omega_{c,i}$ in the critical spectrum generates its own synchrotron spectrum. By distributing the photons at each $\omega_{c,i}$ across a synchrotron spectrum whose shape is given by equation (3.16), repeating the process for all $\omega_{c,i}$ and summing the resulting spectra together, the convolution is complete and the total betatron spectrum is recovered. The distribution of the emitted critical photons are also saved in polar angle θ and azimuthal angle ϕ with respect to the beam axis, therefore allowing reconstruction of the emission's spatial photon distribution. Version 1.3.0 of QV3D was used for all presented studies.

4.5   Computing Architectures

The simulation studies presented in the following chapters used high performance computing (HPC) clusters, owing to the computational demands of PIC simulations. The study presented in Chapter 5 used EPOCH running on the science and technologies facilities council (STFC) SCARF cluster, based at RAL. EPOCH typically required simulations on 200 to 500 central processing units (CPUs) running for 8 hours. For the studies in Chapters 6 and 7 the CERN computing service HTCondor cluster was used to run QV3D simulations. Due to the quasi-static approximation fewer CPUs are required, even when running over many betatron periods, and a maximum of 24 were used in this case, typically running for up to 12 hours. However, the single computing node of which the CPUs were a part had access to up to 1TB of random access memory (RAM) making high resolution three-dimensional simulations possible.

4.6 Summary

Particle-in-cell simulations are used in this thesis to study a variety of plasma wakefield accelerator concepts. This chapter has outlined the theoretical underpinning for their operation, and explained some of the potential drawbacks in their use. In the following three chapters PIC simulations are deployed in different configurations and on different computing architectures in order to best suit the physical systems that they approximate. Nevertheless, limitations will always remain and numerical simulations should ideally be accompanied with comparison to experimental or analytical results. The simulations presented in this thesis are reproducible in that when initialised under the same conditions, and propagated for the same amount of time, they will produce the same results. Therefore error calculations have not been included when stating values derived from the simulations. It is possible to introduce random noise in the initial conditions of a PIC simulation, but this was not done in this case.

Chapter 5

LWFA Injector for AWAKE Run 2

This chapter is an adapted and extended version of the published paper entitled 'Simulation study of an LWFA-based electron injector for AWAKE Run 2', Williamson et al., NIMA, **909**, 126-129 (2018) [153].

5.1   Electron Source Requirements

AWAKE Run 2 aims to limit the relative energy spread and preserve the normalised beam emittance of injected electron beams. This requires that the proton-driven wakefield is correctly loaded to produce a quasi-uniform energy gain for all witness electrons, and that the injected electron beam is correctly matched to the plasma, balancing the focusing and defocusing forces it experiences. It has previously been shown that an electron bunch carrying 100-200 pC of charge within $\sigma_z = $ 40-60 µm would have a sufficient beam current (~ 0.5 kA) to load the proton-drive wakefield; for an electron beam energy ~ 200 MeV and the baseline plasma density for Run 2, $n_e = 7 \times 10^{14}$ cm^{-3}, matching requires a transverse beam size $\sigma_r =$ 5.25 µm [47]. Given that 5 m is available to the electron injector beamline [42], such bunch dimensions and final beam energies are challenging to meet with the current injector, neces-

sitating a new electron injector. One proposed solution is to use an LWFA [51], since they readily produce dense, high-energy, and low emittance electron beams in a compact arrangement. In this Chapter we investigate an LWFA scheme that can meet the requirements for the AWAKE Run 2 electron source, and discuss the transport considerations for such a beam to be injected into the accelerating plasma stage with optimal properties.

5.2 Shock-front Injected LWFAs

The injection mechanism used in an LWFA significantly impacts on the final energy distribution, total charge, and emittance of the accelerated electron bunch. Self-injection is the result of a close approach to the wavebreaking limit; a laser pulse intensity and plasma density are selected such that while some charge is injected the accelerating structure is not destroyed. As discussed in Chapter 2, this can lead to strongly peaked GeV-scale electron spectra using a relatively straightforward plasma source [100], however once wavebreaking is initiated control over the injection is lost. The threshold at which wavebreaking begins is sensitive to small nonuniformities in the laser driver that vary between shots, leading to significant fluctuations in the quantity and final energy distribution of injected electrons.

Beams of higher quality are produced when the injection mechanism is separated from the acceleration process. Shock-front injection [118] occurs at the transition between two consecutive regions of different plasma electron density where $n_{e_1} > n_{e_2}$. The laser intensity and plasma density in both regions are chosen such that nonlinear plasma waves are excited but no wavebreaking occurs, i.e. self-injection is inhibited for the given laser intensity. At the density transition, charge build up at the rear of the bubble during laser propagation in the region n_{e_1} is rephased as λ_p is longer in the lower density region, effectively injecting a quantity of charge into the accelerating field of the wakefield driven

in the region n_{e_2}. This means that injection only occurs at the density transition, and since the injection is initiated in a specific location electron beam properties are significantly more reproducible with respect to self-injection. Typically, shock-front injected electron beams have a stable absolute energy spread ΔE and small normalised emittance ε_n [119]. The density transition must be rapid, occurring over a length on the order of λ_p, and is created by the insertion of a razor blade into the flow of a supersonic gas jet which is locally distorted, creating a hydrodynamic shock. By altering the blade position and therefore the injection location in the plasma, different acceleration lengths will be available and the final peak beam energy may be varied. Quasi-monoenergetic electron beams with peak energies between 10-100 MeV and 1-100 pC of charge have been produced in experiment [119]. The quantity of injected charge can be varied with the peak value of the laser pulse's normalised vector potential a_0, given by equation (2.63), because a larger perturbation in plasma electron number density follows a stronger laser pulse, so that more electrons are available to be injected at the density transition.

More recent investigations have shown that the tilt of the shock is an important factor in control of beam quality [154] and a highly tunable peak energy is possible [155]. When used in combination with ionisation injection [105] the shot-to-shot stability of shock-front injection can be further enhanced. This is because electrons contributing to the charge build up before injection are only 'born' from their parent high-Z atoms after the laser pulse has passed and so are not influenced by nonuniformities in the laser pulse, which are a significant cause of shot-to-shot fluctuations. These characteristics make shock-front injection a scalable source of good quality and reproducible electron beams.

5.3 Beam Generation

5.3.1 Baseline Case

Shock-front injection was chosen to generate the electron beam in this study [153], and the idealised longitudinal plasma electron density profile that was used in the simulation is shown in figure 5.1. It was performed in the PIC code EPOCH [94] using two-dimensional slab geometry, with a window co-moving at the group velocity of the laser pulse. The simulation cell sizes were $\Delta y = 0.1\,\mu\mathrm{m}$ and $\Delta z = 0.02\,\mu\mathrm{m}$ or 600 and 3000 cells in the vertical and longitudinal directions respectively, with 5 macroparticles per cell. In the longitudinal direction there are therefore 40 cells per $0.8\,\mu\mathrm{m}$ laser wavelength. The complete simulation parameters for each study may be found in Appendix A, along with a description of convergence testing.
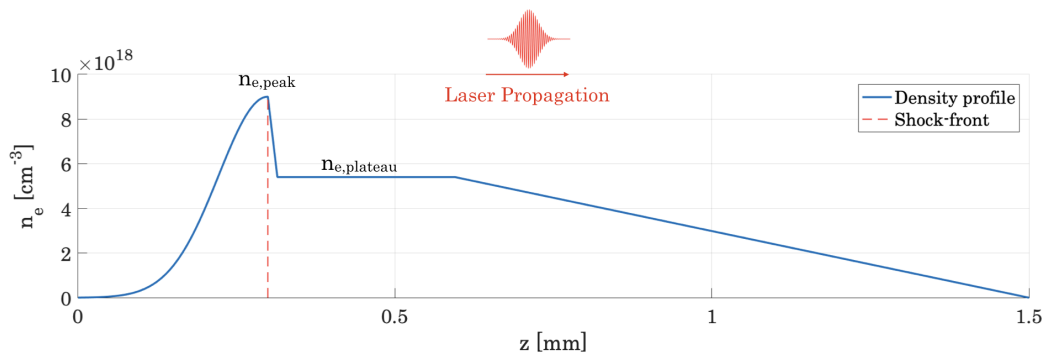
Figure 5.1: Plasma electron density profile used in the baseline simulation study.

The density regions n_{e_1} and n_{e_2} correspond to $n_{e,peak}$ and $n_{e,plateau}$ in table 5.1. The laser pulse propagates from left to right and its parameters are chosen to satisfy a strong blow-out regime as described in Chapter 2, without triggering self-injection. This density profile emulates a supersonic gas jet with a steep initial rise up to a density $n_{e,peak} = 9 \times 10^{18}\,\mathrm{cm}^{-3}$ at the hydrodynamic shock created by the razor blade, where an electron beam is injected. This is followed by a steep drop to a constant density $n_{e,plateau} = 5.4 \times 10^{18}\,\mathrm{cm}^{-3}$
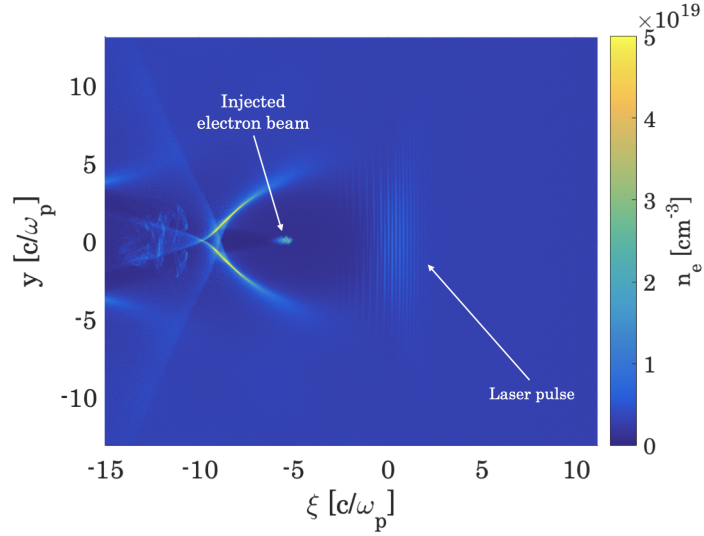
Figure 5.2: Simulated plasma density in the plateau region, downstream from the hydrodynamic shock.

that is maintained for some distance before the plasma density decreases towards vacuum. In this plateau region $c/\omega_p = 2.29\,\mu\text{m}$. A snapshot of the plasma electron density at the end of the plateau region is shown in figure 5.2, showing a strong nonlinear plasma wave and that the driving laser pulse is undergoing relativistic self-focusing. The colour scale is truncated at half its maximum value to clearly show all but the highest density features. At the end of the 1.5 mm gas jet the electron beam is found to have a charge of

(a) 0.75 mm propagation

(b) 1.5 mm propagation
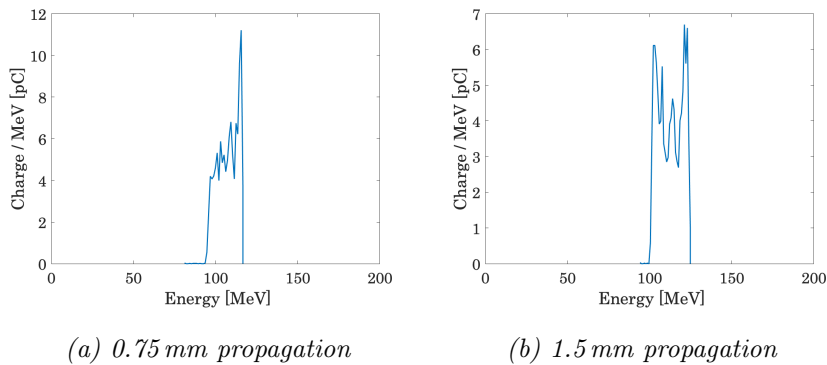
Figure 5.3: Energy spectrum of the simulated electron beam.

Table 5.1: Laser beam and plasma parameters for the LWFA electron injector.

Laser Pulse at Focus	
λ	$800\,\mathrm{nm}$
a_0	2.3
w	$11\,\mathrm{\mu m}$
τ	$22\,\mathrm{fs}$
P	$43\,\mathrm{TW}$
Plasma	
$n_{e,peak}$	$9 \times 10^{18}\,\mathrm{cm}^{-3}$
$n_{e,plateau}$	$5.4 \times 10^{18}\,\mathrm{cm}^{-3}$
Total length	$1.5\,\mathrm{mm}$

$115\,\mathrm{pC}$, a mean energy $\langle E \rangle = 112.7\,\mathrm{MeV}$ with relative energy spread $\delta E / \langle E \rangle = 20.4\,\%$, and a vertical normalised emittance $\varepsilon_{y,n} = 0.35\,\mathrm{mm\,mrad}$. The absolute energy spread is quoted as a width δE not as an r.m.s. value, since the electron bunch energy spectrum is non-Gaussian, as shown in figure 5.3 (b). The electron beam is Gaussian in the transverse vertical direction and has an r.m.s. size $\sigma_y = 0.56\,\mathrm{\mu m}$. Longitudinally the beam has a somewhat Maxwellian distribution since the injection is not terminated as abruptly as it begins. This results in a short duration of continual injection but a bunch length of no more than $2.0\,\mathrm{\mu m}$. This configuration of laser and plasma parameters can therefore meet the fundamental charge requirements of the AWAKE Run 2 electron injector [153], providing a potential source of electrons that could be immediately adjacent to the main proton beamline with the laser driver transported from elsewhere. The transverse size is well within the required matched radius, the normalised emittance is small, and while relatively large the energy spread in the beam is strongly peaked. However, the bunch length results in a beam current of at least $17\,\mathrm{kA}$ that greatly exceeds the

(a) 0.75 mm propagation   (b) 1.5 mm propagation
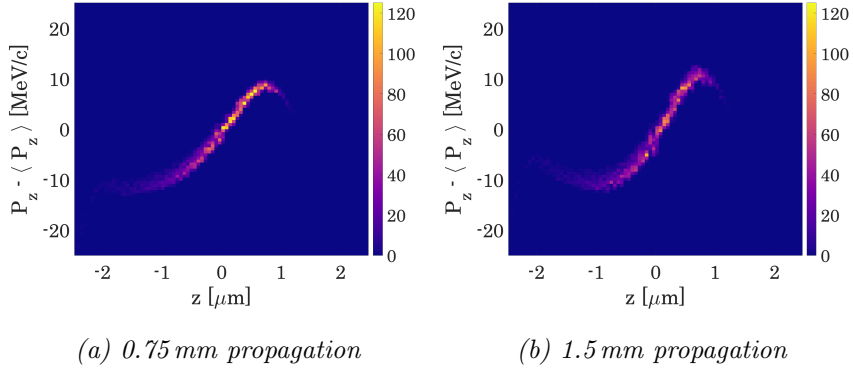
Figure 5.4: Longitudinal phase space of the simulated electron beam, with colourbar in units of macroelectrons.

(a) 0.75 mm propagation   (b) 1.5 mm propagation
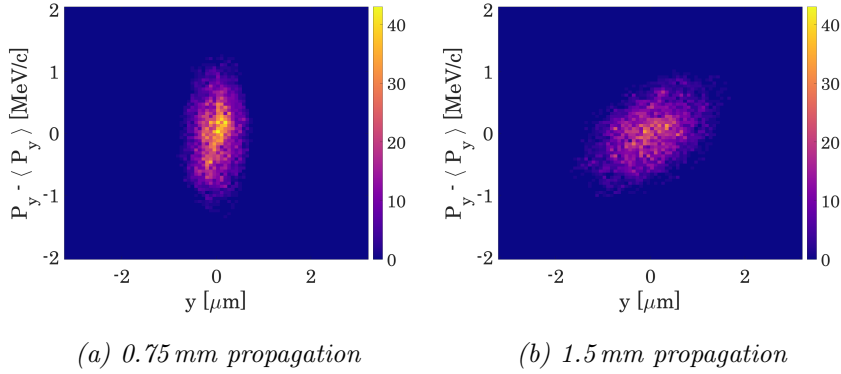
Figure 5.5: Vertical transverse phase space of the simulated electron beam, with colourbar in units of macroelectrons..

optimal value. Consequently such an electron beam will overload the proton-driven wakefield, and would require extension during transport. The majority of acceleration occurs in the highest density regions, while the downramp region provides a tapering focusing force until the plasma-vacuum interface. To demonstrate the electron beam dynamics in the downramp region the energy spectrum, longitudinal phase space, and transverse phase space are shown at both 0.75 mm and 1.5 mm propagation in figures 5.3, 5.4, and 5.5 respectively.

The longitudinal phase space shows that the beam has a strong energy chirp, set initially by the injection mechanism, which has a small contribution from

109

the variation of the accelerating field E_z along the beam. This results in a small increase in energy spread as the beam gains some energy in the downramp region. The effect of beam loading will be discussed in the next section. Transversely, the beam has reached a waist at $0.75\,\mathrm{mm}$ where its vertical size is at a minimum. The average betatron wavelength in the downramp region is $\langle\lambda_\beta\rangle = 0.57\,\mathrm{mm}$, and therefore the plasma density falls to zero slowly over multiple betatron periods and as such the focusing strength also changes slowly. This tapered extraction of an electron beam from an LWFA has been shown to re-orientate the phase space ellipse and preserve its normalised emittance [156]. As can be seen in figure 5.5 (b), at $1.5\,\mathrm{mm}$ propagation the beam is diverging and has a larger transverse size and smaller spread of momenta; the normalised beam emittance has been approximately conserved, where $\varepsilon_{y,n} = 0.25\,\mathrm{mm\,mrad}$ at $0.75\,\mathrm{mm}$ and $\varepsilon_{y,n} = 0.35\,\mathrm{mm\,mrad}$ at $1.5\,\mathrm{mm}$. We define the laser and gas jet density profile presented in this section, summarised in table 5.1, as the 'baseline' simulation. The simulation studies presented in following sections are parameter scans that vary from this baseline.

5.3.2   Laser vector potential

The laser strength parameter a_0 was varied in order to assess the effect of beamloading in the LWFA before extraction and injection into the proton-driven wakefield. The baseline simulation was repeated for laser strength values of $a_0 = 2.2$ and $a_0 = 2.5$. A larger quantity of charge is injected into the accelerating phase of the wakefield as a_0 increases, thereby lowering the accelerating field in the region of the bunch, as can be seen from the plasma density plots in figures 5.6 (a, c, e) with the corresponding accelerating field E_z overlaid in each case. The degree of continuity seen in the injection mechanism also varies with a_0, and as it decreases the injection is terminated more abruptly. This manifests as a shorter low-energy tail, seen in the beam longitudinal phase space of figure 5.6 (b) when compared with figure 5.6 (f). All plots in figure

110

(a) $a_0 = 2.2$

(b) $a_0 = 2.2$

(c) $a_0 = 2.3$

(d) $a_0 = 2.3$

(e) $a_0 = 2.5$

(f) $a_0 = 2.5$
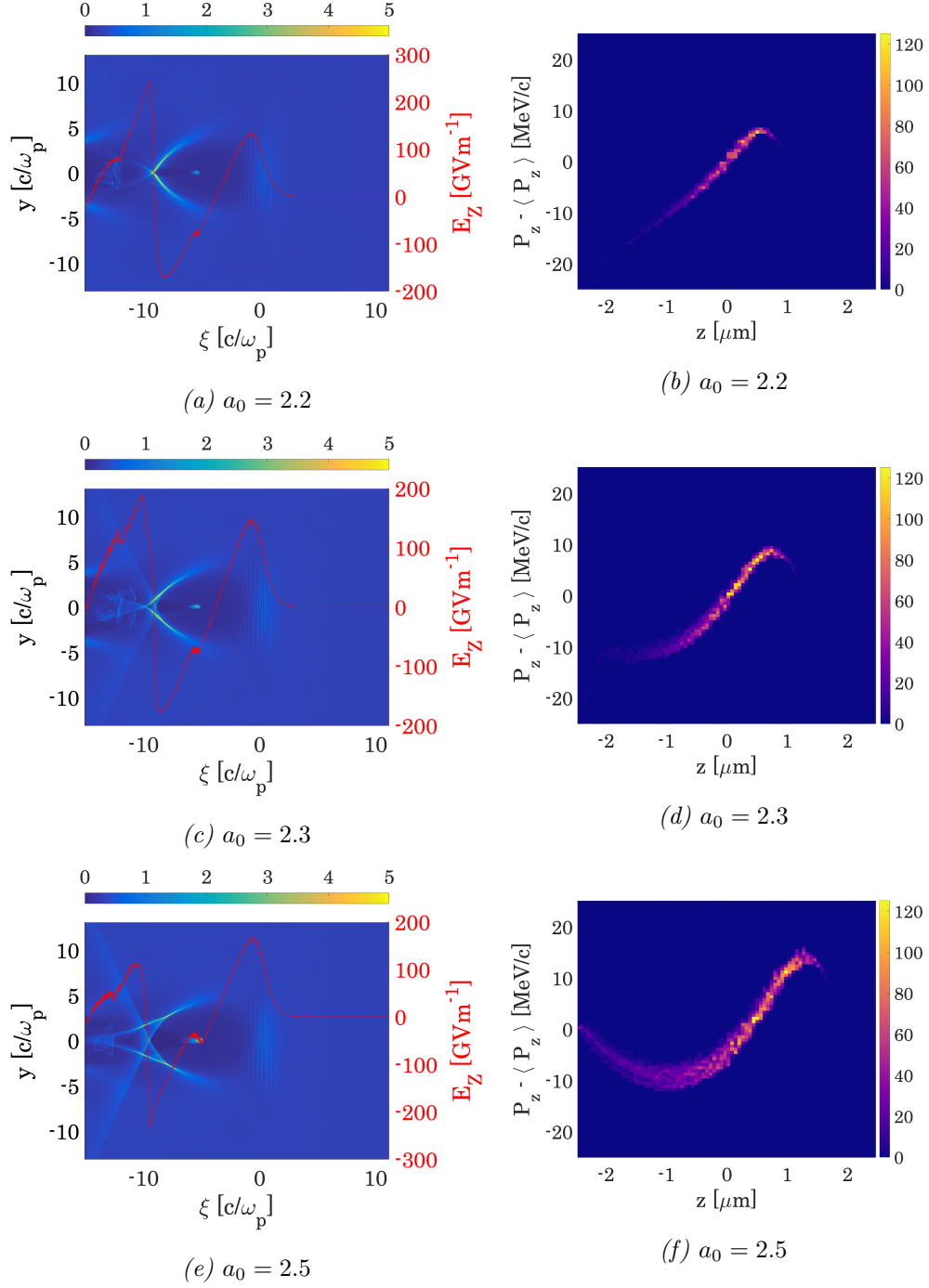
Figure 5.6: Simulated plasma density, with colourbar in units of $10^{19}\,cm^{-3}$, and longitudinal beam phase space, with colourbar in units of macroelectrons, at 0.75 mm.

5.6 are shown at 0.75 mm because at the full 1.5 mm propagation the plasma electron density has fallen by orders of magnitude and the wakefield structure
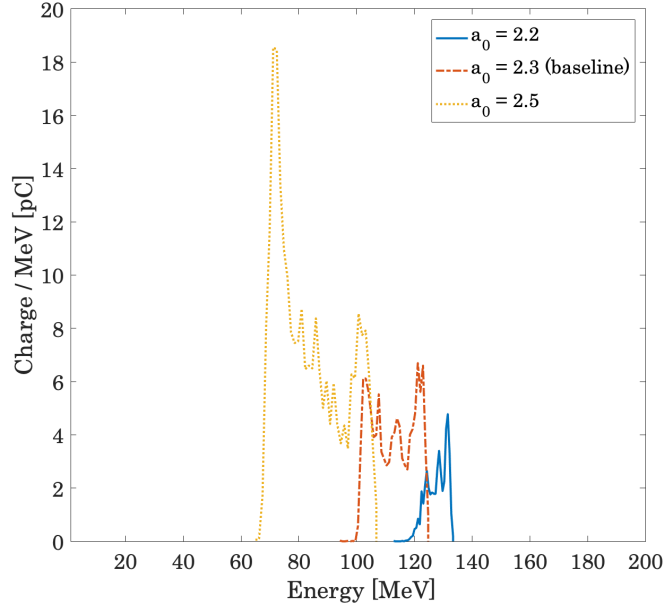
Figure 5.7: Electron energy spectra at the end of the gas jet (1.5 mm propagation) for different laser strengths.

is no longer visible. By the end of the gas jet, at the full 1.5 mm propagation distance, the electron beams injected for each laser strength $a_0 = 2.2$, $a_0 = 2.3$, and $a_0 = 2.5$ have a decreasing mean energy of $\langle E \rangle = 127.7\,\text{MeV}$, $\langle E \rangle = 112.7\,\text{MeV}$, and $\langle E \rangle = 83.7\,\text{MeV}$ respectively. Each contains an increasing quantity of charge, which is shown in the electron energy spectra of figure 5.7. The respective total beam charges are $63.8\,\text{pC}$, $115\,\text{pC}$, and $244\,\text{pC}$; the relative energy spread $\delta E / \langle E \rangle$ increases as $9.48\,\%$, $20.4\,\%$, and $46.6\,\%$.

Therefore the beam energy spread may be significantly improved by lowering the laser strength parameter and in turn optimising the beam loading, however the total quantity of injected charge, e.g. for $a_0 = 2.2$, does not meet the minimum requirement for the electron injector. As a result there is an offset between energy spread and charge, and the baseline case with $a_0 = 2.3$ provides such a balance. The extent to which beam loading impacts on the energy distribution is not entirely clear: a higher laser intensity may also be sufficient

to initiate wavebreaking and self-injection, a source of additional charge, and interaction between the shock-front and self-injection mechanisms could itself impact on the final energy spectrum when a_0 is increased. Nonetheless beam loading may be optimised to reduce δE [153].

5.3.3 Plateau length

The final beam energy may be increased by extending the accelerating region, for example up to the value of $\sim 200\,\text{MeV}$ used by Olsen et al. (2018) [47]. The baseline simulation with $a_0 = 2.3$ was repeated over a range of gas jet density profiles, summarised in table 5.2, configured such that the upramp and downramp regions had the same length while the plateau region was made longer.

Table 5.2: Simulated final electron beam energies for an increasing gas jet length.

Gas Jet Width [mm]	Plateau Length [mm]	$\langle E \rangle$ [MeV]
1.50	0.280	112.7
1.60	0.380	131.7
1.70	0.480	149.8
1.80	0.580	166.9
1.90	0.680	182.9
2.00	0.780	197.6

The energy gain has an approximate linear scaling with plateau length, although its slope is less than would be expected if all the acceleration took place in the plateau region. This indicates that electrons gain the majority of their longitudinal momentum soon after injection. The absolute energy spread δE across the simulated range of 6 plateau lengths had a mean value of $\langle \delta E \rangle = 23.77$ MeV, where all δE had a value within $\pm\,8.3\,\%$ of the mean. Because δE is stable for all simulations it is likely to originate with the injection mecha-
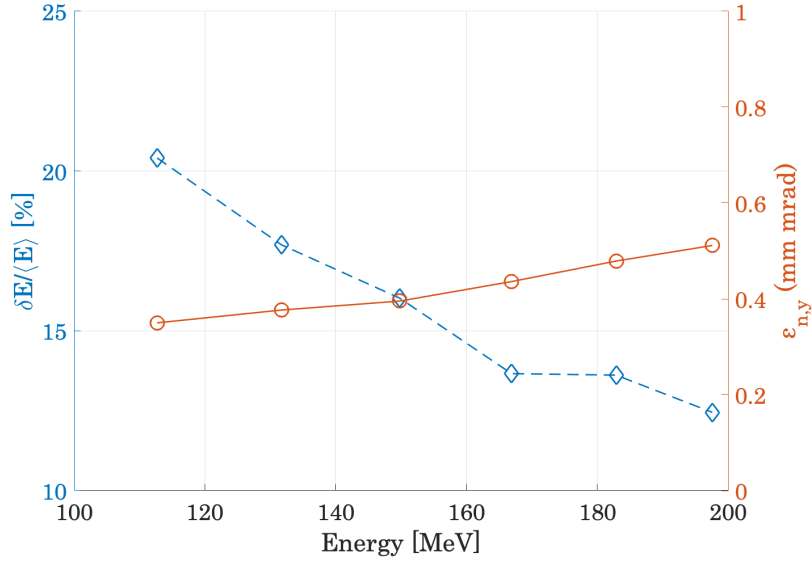
Figure 5.8: Simulated electron beam relative energy spread $\delta E/\langle E \rangle$ (dashed line) and normalised vertical emittance $\varepsilon_{y,n}$ (solid line) for a range of final mean beam energies.

nism, which is unchanged, and not the acceleration. A fixed δE results in a decreasing relative energy spread $\delta E/\langle E \rangle$ for larger final mean beam energies $\langle E \rangle$, a trend consistent with experimental observation of shock-front injected electron beams [119]. The normalised vertical emittance $\varepsilon_{y,n}$ remains low, below $0.6\,\mathrm{mm\,mrad}$ in the simulated range of plateau lengths, owing to the unchanged gradient in the downramp region. Both are shown in figure 5.8.

5.3.4 Limitations of two-dimensional geometry

Two-dimensional PIC simulations can reduce computational time by orders of magnitude, while providing a good approximation to the physics of laser-plasma interaction for systems that exhibit symmetry in at least one spatial dimension. However such a geometry does have limitations, and two in particular are relevant for the simulations presented in this chapter [153]. Firstly, the automatic weighting given to each macroparticle is not representative of the total number of electrons present in the laser-plasma interaction: because

the electron density is a three-dimensional variable an assumption must be made on the extent of the laser-plasma interaction in the non-simulated third dimension, when estimating the total number of electrons. In the presented simulations this is taken to be the FWHM diameter of the laser pulse when estimating the presented bunch charges. One consequence of this is that the charge density of a simulated electron beam will not be entirely representative of the real value, making it challenging to evaluate beam loading effects quantitatively. Secondly, relativistic self-focusing of the laser pulse is proportional to w_0 in two-dimensions and w_0^2 in three. Therefore self-focusing develops at a slower rate in a two-dimensional simulation, and the laser intensity required to produce a given regime of laser-plasma interaction may be overestimated. Three-dimensional PIC simulations are necessary to confirm the injected charge for a given laser intensity.

5.4   Beam Transport and Matching

Once extracted from the LWFA, the electron beam properties will evolve significantly if they are not controlled, and they require optimisation as the beam is transported to the point of injection into the proton-driven wakefield. The laser-driven wakefield provides strong focusing of the electron beam; on exiting the plasma this is lost and the beam diverges due to its finite emittance. An electron beam distribution from the baseline simulation, assumed to be radially symmetric such that $\sigma_x = \sigma_y$, is implemented in the space-charge tracking code ASTRA [157]. In ASTRA, the beam is distributed on a grid of longitudinal slices and radial concentric rings. Therefore, the number of particles per cell can vary strongly between cells at radial positions close to the beam axis and weakly far from it; consequently it can be the case that very few particles are present close to the axis, leading to abrupt statistical fluctuations and erroneous calculation of space-charge forces within the beam. To mitigate this

issue the width of concentric rings can be chosen to increase towards the beam axis, however it is still necessary to choose either a small number of grid cells or a very large number of particles to ensure that a reasonable sample of particles are present in every cell. In the presented simulations the former case is chosen, and the beam is represented by 500 particles and ten cells in both the longitudinal and radial directions. Figure 5.9 shows the field free propagation
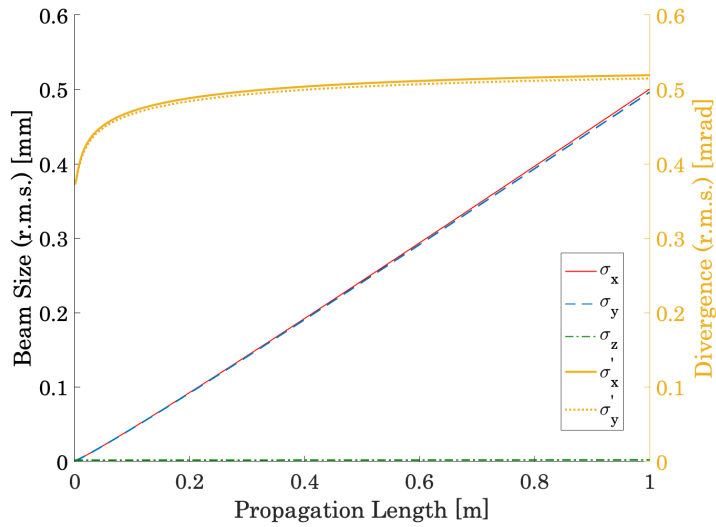
Figure 5.9: LWFA-accelerated electron beam dimensions and divergence as it propagates in vacuum.

of the beam in vacuum, tracked over 1 metre. Transverse beam sizes $\sigma_{x,y}$ grow significantly, and while the bunch length σ_z increases slightly it remains close to its value at generation. Tracking was performed both with and without space-charge forces, demonstrating $\varepsilon_{y,n}$ growth in both cases. Although some space-charge contribution exists, the intrinsic growth of ε_n during vacuum propagation is seen in electron beams with large energy spread and divergence [62]. As σ_z remains small the need for longitudinal phase space manipulation of the electron beam before injection into the proton-driven wakefield is apparent. Focusing optics are also needed to match the electron beam to the accelerating stage of the main beamline at AWAKE which as discussed requires

116

a transverse size of 5.25 μm if the initial normalised emittance is 2 mm mrad and $\gamma = 426$ [47]. In Run 2 the AWAKE plasma source may be replaced with two separate laser-ionised vapour vessels, one for pre-modulating the proton beam and one for acceleration. This presents an opportunity to inject the electron beam in the space between. Such a space is limited, to 1 m or less in order to avoid proton beam divergence between consecutive vapour vessels that would result in a sub-optimal accelerating wakefield. From the electron beam properties determined in the simulations, the requirements of the LWFA injector beamline must be to transport the electron beam to the proton-driven PWFA stage, lengthening the bunch size to reduce its intrinsic beam current, and to match its transverse size for normalised emittance preservation. If the LWFA electron beam is initially generated parallel to the proton beamline a magnetic dipole chicane can transport the electron beam horizontally towards it.

Given the dispersion of such a magnetic lattice, the resulting energy-path correlation may be exploited to decompress the electron beam longitudinally as it is transported. As seen in figure 5.4(b) the electron beam has a strong energy chirp and the magnetic decompression of such electron beams has been investigated previously [158] to simultaneously reduce their slice energy spread (the energy spread within a given longitudinal slice of the beam) and beam current in order for them to be used as free-electron laser (FEL) drivers, which was found to be possible with small magnetic chicanes with longitudinal dispersion $R_{56} = 10\text{-}500$ μm [158].

Owing to the high initial beam current, coherent synchrotron radiation (CSR) effects must also be taken into account [159]. To facilitate matching, a quadrupole triplet can be placed within the chicane and in this section we outline a triplet configuration to achieve this. The thin lens approximation is valid if the length l of a quadrupole is small compared to its focal length f,

and in this case the strength of a quadrupole is given by $k = 1/(fl) = (eg)/p$ where g is the magnetic gradient and e and p are the charge and momentum respectively of a particle within the magnetic field. Alternatively [65]:

$$k[\mathrm{m}^{-2}] = 0.2998 \frac{g[\mathrm{Tm}^{-1}]}{p[\mathrm{GeV}c^{-1}]}. \tag{5.1}$$

For an electromagnetic quadrupole with $g = 15\,\mathrm{Tm}^{-1}$ and $l = 20\,\mathrm{cm}$ the focal length for a $113\,\mathrm{MeV}$ electron beam, from the baseline simulation, is $12.6\,\mathrm{cm}$, and over a metre in a triplet configuration. The components of the beamline must therefore be compact for the injection to take place within $1\,\mathrm{m}$. Focal lengths could be decreased with larger magnets but again this would exceed the spatial restraints of an on-axis LWFA injector.

One possibility to achieve compact focusing is with permanent magnetic quadrupoles (PMQs), since they have magnetic gradients up to $560\,\mathrm{Tm}^{-1}$ [160] and cm-scale focal lengths. A simple magnetic lattice was added to the simulation in ASTRA consisting of three PMQ lenses of $236\,\mathrm{Tm}^{-1}$, $539\,\mathrm{Tm}^{-1}$, and $471\,\mathrm{Tm}^{-1}$, each $30\,\mathrm{mm}$ in length, placed at $0.03\,\mathrm{m}$, $0.07\,\mathrm{m}$, and $0.11\,\mathrm{m}$. Focused beam sizes and normalised emittance throughout such a PMQ triplet were tracked for a range of electron bunch energy spreads and are shown with $\delta E/\langle E \rangle = 5\,\%$ in figure 5.10, $\delta E/\langle E \rangle = 10\,\%$ in figure 5.11, and $\delta E/\langle E \rangle = 20.4\,\%$ in figure 5.12.

The energy dependence of quadrupole focusing can be seen in equation (5.1), and this chromatic behaviour results in a broad distribution of foci for large energy spreads. For $\delta E/\langle E \rangle = 5\,\%$ beam sizes are focused to $\sigma_{x,y} = 10.8\,\mu\mathrm{m}$ in $20\,\mathrm{cm}$ whereas for $\delta E/\langle E \rangle = 20.4\,\%$, found in the baseline simulation, focusing is no longer symmetric and beam waists are larger. Optimisation of individual magnet strength and positioning to reach the stipulated transverse beam size $\sigma_{x,y} = 5.25\,\mu\mathrm{m}$ may result in a longer footprint for the triplet, but ultimately

reducing the beam energy spread at generation is the best method to aid beam transport. One-dimensional emittance growth could be problematic, however the aim of AWAKE Run 2 is simply to preserve the normalised emittance throughout acceleration in the proton-driven wakefield at its injected value, which will vary given the initial beam size and energy.
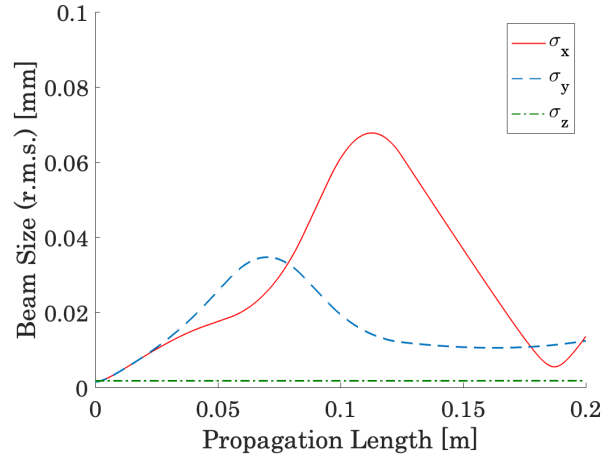
(a) Beam size
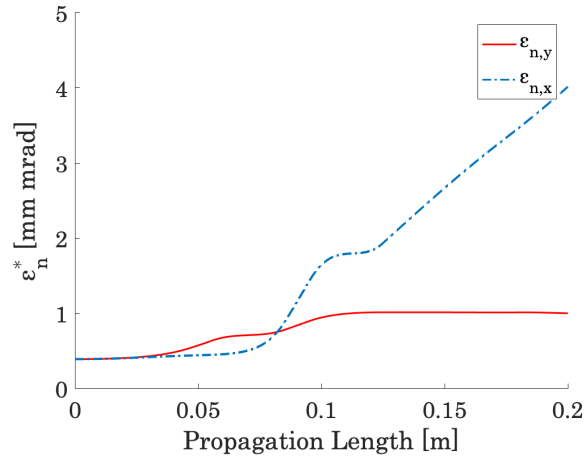
(b) Normalised emittance

Figure 5.10: LWFA beam dynamics in a PMQ triplet with $\delta E/\langle E \rangle = 5\,\%$.
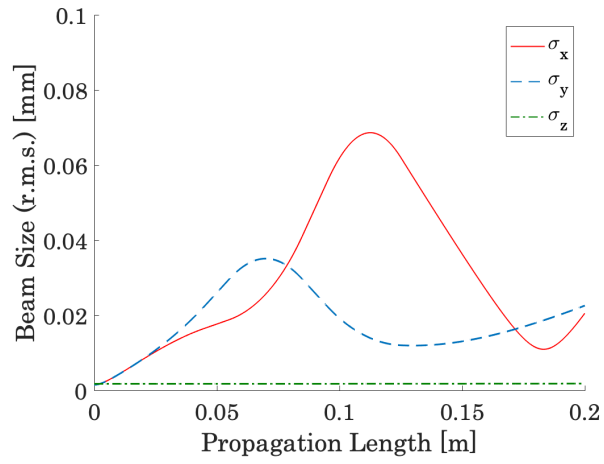
(a) Beam size
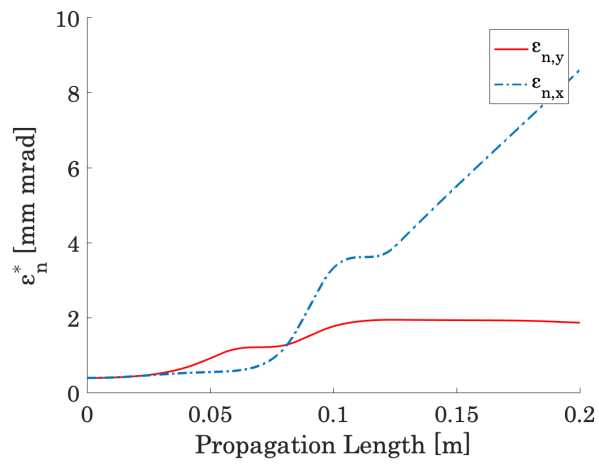
(b) Normalised emittance

Figure 5.11: LWFA beam dynamics in a PMQ triplet with $\delta E / \langle E \rangle = 10\,\%$.
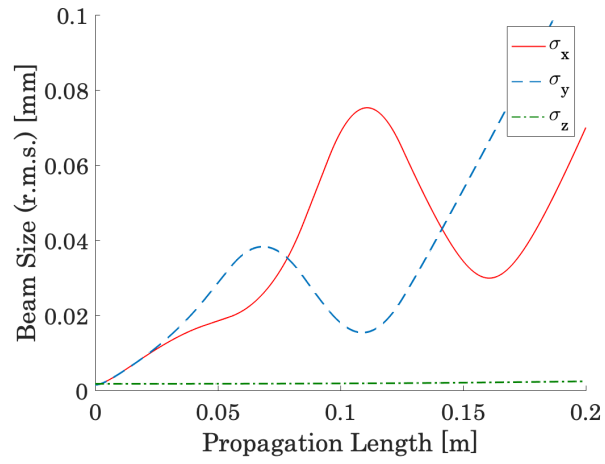
(a) Beam size
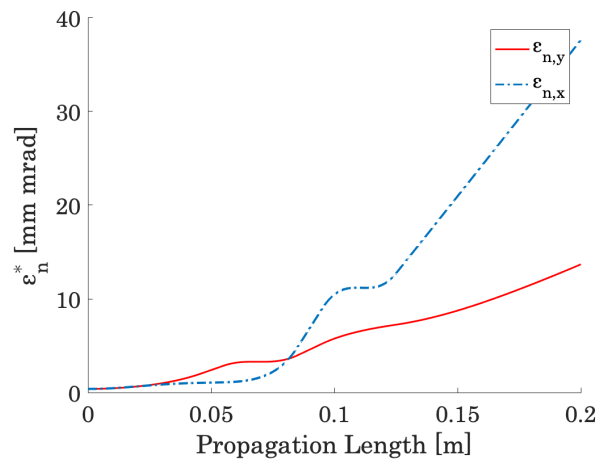
(b) Normalised emittance

Figure 5.12: LWFA beam dynamics in a PMQ triplet with $\delta E/\langle E \rangle = 20.4\,\%$.

5.5 Summary

A set of laser and plasma parameters have been investigated for an LWFA-based electron injector, which could be implemented in Run 2 of the AWAKE experiment. PIC simulations show charge requirements can be met with a laser of $a_0 = 2.3$, corresponding to a power of $43\,\mathrm{TW}$ for $\tau = 22\,\mathrm{fs}$ and $w_0 = 11\,\mathrm{\mu m}$. A shock-front injected LWFA is scalable in energy, via gas jet length, and charge, via laser strength. The beam quality is set largely by the injection mechanism and the LWFA performs with small variations in δE and ε_n so long as the accelerating field is not overloaded with excess beam charge, resulting in good quality electron beams with decreasing $\delta E/E$ for higher energies. The simulations also demonstrate emittance preservation within the LWFA owing to a tapered plasma density profile. Full three-dimensional PIC simulations are required to confirm the laser parameters.

After generation the electron bunch diverges strongly but retains its short duration. Beam loading is required to limit the growth of $\delta E/E$ during acceleration in the proton-driven wakefield, and the high-current LWFA beam must be extended longitudinally. Longitudinal bunch decompression is possible with a magnetic dipole chicane, which would also reduce the pre-injection slice energy spread of the bunch. Further detailed study of the transport line should take account of CSR effects with an appropriate beam dynamics code, e.g. Elegant [161]. A basic PMQ triplet has been investigated as a method of compact focusing prior to injection into the proton-driven wakefield. Matching the LWFA generated beam is possible with such a configuration, but an optimal working point must be set between beam energy, transverse size, and the target normalised emittance to be preserved during acceleration in the proton-driven wakefield.

Chapter 6

Betatron Radiation Diagnostics for AWAKE Run 2

This chapter is an adapted and extended version of the published paper entitled 'Betatron radiation diagnostics for AWAKE Run 2', Williamson et al., NIMA, **971**, 164076 (2020) [162].

6.1 Betatron Radiation Diagnostics in Plasma Accelerators

In Run 2 the AWAKE experiment aims to preserve the normalised emittance of an injected electron beam, a necessary step for the future application of proton-driven PWFA. As such, the beam emittance must be measured prior to injection and acceleration in the proton-driven wakefield, and following it. The pepper-pot method, the use of which is discussed for the electron injector in Chapter 1, is less suitable for measuring emittance after acceleration as it is intercepting and destructive. It therefore prevents a simultaneous measurement of the beam charge that has been captured and accelerated in the

wakefield. Captured charge is a key figure of merit for the study of injection dynamics into the proton-driven wakefield, and a single-shot measurement encompassing electron beam emittance, charge, and energy, even if it were from different diagnostic methods, would be preferred. However, if an independent measurement of emittance was acceptable a pepper-pot diagnostic could still be feasible; emittance measurements with a pepper-pot have been demonstrated for electron beam energies of $3\,\mathrm{GeV}$ [163], outside of the space-charge dominated regime for which they were originally conceived. Measurements of the electron beam emittance after the accelerating stage are also possible by scanning the existing electron spectrometer quadrupole magnet strengths.

Ultimately, a pepper-pot and quadrupole scans both measure beam emittance outside of the plasma wakefield. Such a measurement makes it more difficult to discern distinct influences on the beam phase space, which for example can be affected as it transits the plasma-vacuum interface [156]. Measurement and analysis of betatron radiation from accelerated electron beams has made for a useful diagnostic tool in LWFA experiments, partly because it may be used to reconstruct beam emittance inside the accelerating wakefield, by virtue of the radiation emitted during acceleration.

The critical frequency of the measured spectrum ω_c is either used to calculate an average betatron amplitude $\langle x_\beta \rangle$ via equation (3.17) and directly infer an equivalent r.m.s. beam size, i.e. $\langle x_\beta \rangle = \sigma_r$ [123], or is used in conjunction with x-ray source size measurements to determine σ_r [164, 165]. When paired with an independently measured divergence σ_r' outside of the plasma, the uncorrelated normalised emittance may then be calculated as $\varepsilon_n \simeq \gamma \sigma_r \sigma_r'$. Again this measurement suffers from emittance dilution at the plasma exit. The correlated emittance within the plasma may be reconstructed with betatron and electron energy spectra alone, by analysing a betatron spectrum as the result of a convolution of single-particle orbits [52]. This method could be

employed at AWAKE as a non-intercepting, intra-wakefield emittance diagnostic, and the following simulation study quantifies the expected number and spatial distribution of betatron photons in order to determine its feasibility.

6.2 Betatron Emission in AWAKE Run 2

6.2.1 Baseline case

In AWAKE Run 2, the two-dimensional normalised emittance ε_n^* will be preserved at its injected value by matching the electron beam to the plasma, while the final relative energy spread $\sigma_{\gamma_f}/\langle\gamma_f\rangle$ will be kept to the %-level by beamloading the proton-driven wakefield. To meet these conditions beam properties were previously determined by Olsen et al. (2018) [47]. As discussed in Chapter 3 matching requires an initial equilibrium transverse beam size that, for a fixed beam energy, will result in a non-evolving beam size as it propagates in the plasma [166]. With acceleration, adiabatic damping reduces the beam size and geometric emittance, while the normalised emittance is invariant.

The study in this Chapter reproduces the model of Olsen et al. [47] in the quasi-static PIC code QV3D, which has the added consideration of synchrotron emission, allowing the estimation of the expected betatron radiation properties for AWAKE Run 2 under a range of experimental conditions. To avoid simulation of the full proton beam a single short bunch, with transverse size $\sigma_{x,y} = 200\,\mu\text{m}$, $\sigma_z = 40\,\mu\text{m}$ that contains 1.46×10^{10} protons ($n_{pb} = 0.83\,n_e$), is used to produce the accelerating field E_z. The proton beam energy was set with $\gamma_{pb} = 426$, the typical value on extraction from the CERN SPS. In the simulation the proton mass is increased by a factor of 10^6 in order to suppress the transverse evolution of the proton beam, and therefore eliminate any betatron radiation it might produce. The witness electron beam has $\gamma_{eb} = 426$, $\sigma_{x,y} = 5.25\,\mu\text{m}$, $\sigma_z = 60\,\mu\text{m}$ and contains $100\,\text{pC}$ (6.25×10^8 electrons). With
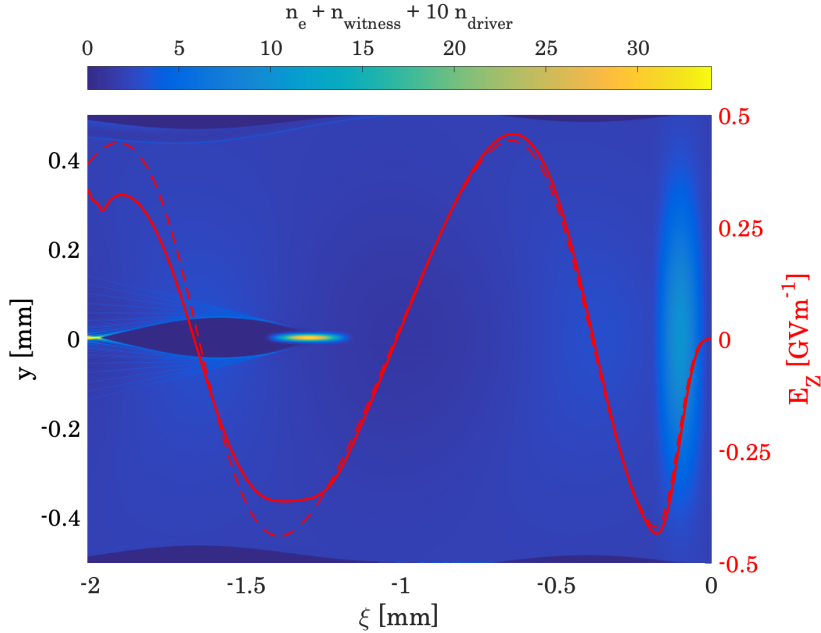
Figure 6.1: Combined witness electron, proton driver and bulk plasma densities, where $\xi = z - tc$ is the co-moving coordinate. The accelerating field E_z is shown both in the case it is loaded with an electron beam (solid line), and where it is unloaded (dashed line). The driver and witness beams propagate to the right.

$n_{eb} = 34.3 \, n_e$ the electron beam is well within the blow-out regime. The initial normalised emittance in both transverse directions ε_n^* and energy spread $\sigma_{\gamma_i}/\langle\gamma_i\rangle$ are $2 \, \mathrm{mm \, mrad}$ and 0.1% respectively. These set of simulated beam and plasma parameters represent the baseline case, which is expanded on in the following sections (6.2.2, 6.2.3) by varying beam and plasma properties. Simulations in QV3D were performed with cell sizes of $\Delta x = \Delta y = 0.01 \, c/\omega_p$ ($2 \, \mu\mathrm{m}$) and $\Delta z = 0.1 \, c/\omega_p$ ($20 \, \mu\mathrm{m}$) in the transverse and longitudinal directions respectively. Four particles per cell were used for the bulk plasma, which had an electron number density $n_e = 7 \times 10^{14} \, \mathrm{cm}^{-3}$. The simulation domain had dimensions of $5 \times 5 \times 10 \, c/\omega_p$. The complete simulation parameters for each study may be found in Appendix A, along with a description of convergence testing. Figure 6.1 shows the loaded accelerating field E_z, approximately constant along the length of the electron beam. The density scale is in units of n_e;
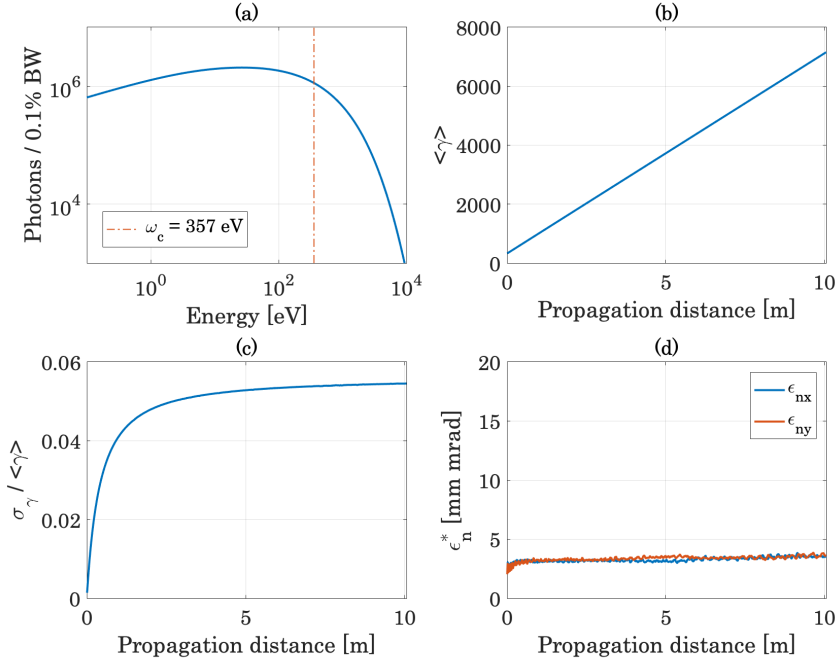
Figure 6.2: The angle-integrated betatron spectrum $N(\hbar\omega)$ (a) and electron beam γ, $\sigma_\gamma/\langle\gamma\rangle$, and ε_n^* over 10 metres (b-d) for the baseline case with $\sigma_{x,y} = 5.25\,\mu m$.

the density of the proton beam n_{pb} is artificially increased by a factor of 10 so that it is visible. The electron beam drives its own local ion focusing channel to facilitate matching. The transverse dynamics of the electron beam are then somewhat independent from the quasi-linear wakefield driven by the proton beam, whose principle role is to provide longitudinal acceleration, although the proton-driven wakefield does contribute some transverse focusing.

In Figure 6.2 (a) the simulated emission integrated over all angles is shown with $\hbar\omega_c = 357\,\text{eV}$, containing a total of $N_e = 9.83 \times 10^8$ photons. The spectrum gives the number of photons in 0.1% bandwidth ($\Delta\hbar\omega = 10^{-3}\hbar\omega$) per photon energy $\hbar\omega$. Given the plasma and beam properties in AWAKE Run 2, the strength of transverse electron motion at any given time along the accelerator is $\alpha_\beta \sim 1$, however since the energy is continuously changing over many betatron periods the final emission will be broadband. As such, assuming a

127

(a) Horizontal direction　　　　　　*(b) Vertical direction*
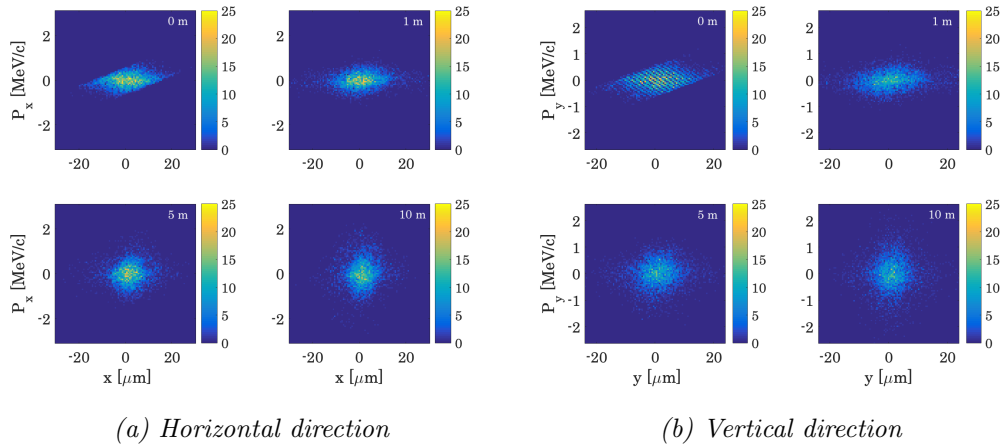
Figure 6.3: The transverse phase space portraits of the simulated electron beam at 0 m, 1 m, 5 m, and 10 m propagation. Colourbar indicates macroelectron number.

spectral shape given by equation (3.16) is a reasonable approximation. Figures 6.2 (b-d) show the evolving beam parameters: energy spread saturates at less than 6%, while the normalised emittance remains close to the matched value; some emittance growth is seen, due largely to the erosion of the bunch head by interaction with the plasma.

Figure 6.3 shows that the two-dimensional phase space portrait of the beam rotates as it propagates along the 10 m-long plasma column, while the area it occupies in phase space does not change significantly. The direction into which photons are emitted is saved in the simulation, allowing for the spatial distribution of the betatron emission to be reconstructed. The orbits of electrons in ion cavities directly map to the observed spatial distribution of betatron radiation [167]; in LWFA, the direction of transverse oscillation of electrons in the wake of the driving laser pulse is often shown in experiment to be anisotropic, with a preference to follow the polarisation direction of the laser [167, 168]. In PWFA, with a relativistic particle beam driver, no such direct driver-witness interaction occurs and only the plasma-mediated wakefield influences the witness beam dynamics. Therefore, so long as the emitting

witness beam is matched, militating its own envelope oscillations, and is in the centre of the ion channel where focusing forces are symmetric, the distribution of radiation is likely be isotropic. The betatron radiation previously measured from a PWFA was seen to have a round spot [169].
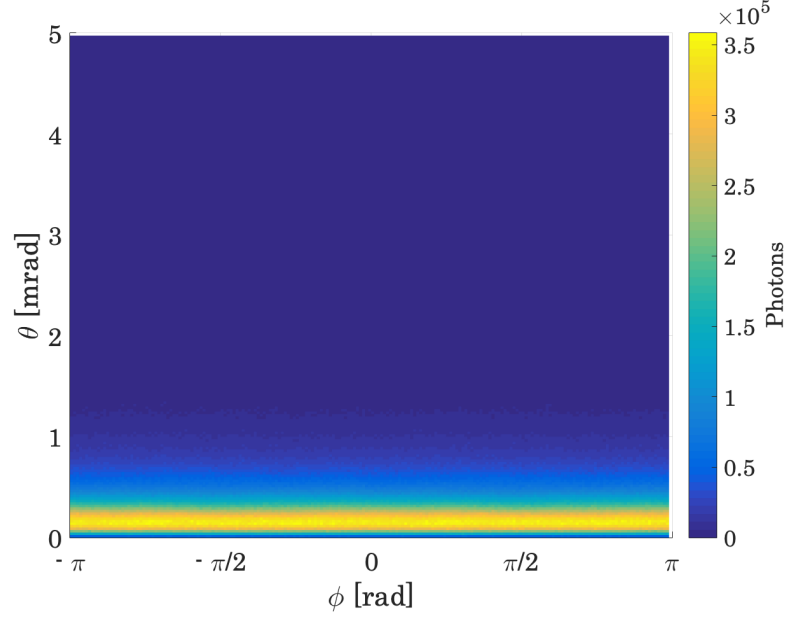
Figure 6.4: The simulated spatial distribution of radiation in the baseline case, distributed in θ and ϕ with respect to the acceleration axis.

The simulated spatial distribution of radiation for the baseline case is seen in figure 6.4, distributed in polar angle θ and azimuthal angle ϕ with respect to the acceleration axis, each within 200 bins. The distribution is isotropic in ϕ, indicating a well matched beam, with a local minima on axis where $\theta = 0$. This is because the highest photon flux from an individual electron is emitted into a cone with $\theta \sim \alpha_\beta/\gamma$ about the maximum excursion of its orbit, and since in the baseline AWAKE Run 2 case $\alpha_\beta \sim 1$ the cones of emission from opposing sides of the electron orbit do not overlap. The Hosing Instability [40] results from a coupling of the transverse wakefield to the transverse position of the driving beam that excites it, which can cause initially small transverse offsets to become exponentially amplified during the acceleration process. Such

motion would have a clearly discernible impact on the spatial distribution of betatron radiation. Beam hosing may be mitigated by varying the wakefield along the beam [170] or suppressed with plasma ion motion [171] in a manner analogous to BNS damping, discussed in section 2.1.2. Betatron radiation may be used to infer the transverse dynamics of an electron beam accelerated in a plasma wakefield, and therefore diagnose the onset of the hosing instability [172].
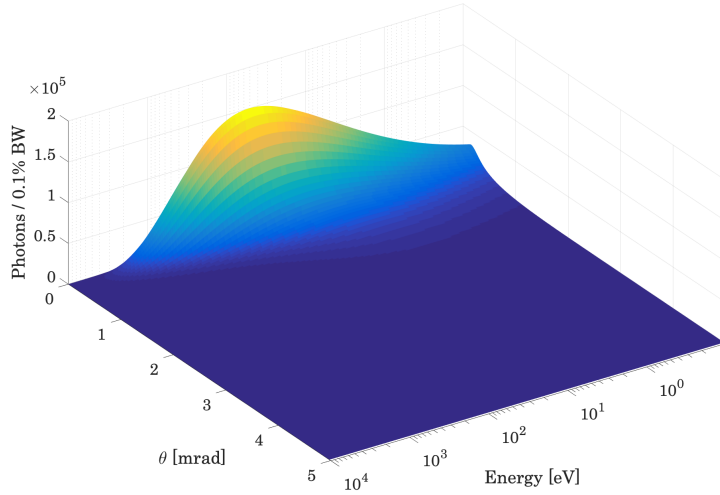
Figure 6.5: The angular spectrum $N(\hbar\omega, \theta)$ for the baseline Run 2 case with $\sigma_{x,y} = 5.25\,\mu m$.

The angular betatron spectrum $N(\hbar\omega, \theta)$ with respect to the acceleration axis z is shown in figure 6.5. This angular spectrum gives the number of photons in 0.1% bandwidth ($\Delta\hbar\omega = 10^{-3}\hbar\omega$) per photon energy $\hbar\omega$ per polar observation angle θ, which is distributed in 200 bins. In this baseline AWAKE Run 2 case, with $\sigma_{x,y} = 5.25\,\mu m$, most emitted photons (96.9 %) are confined to small angles less than 1 mrad and have energies in the range 1-1000 eV. As shown in figure 6.6, a number of photons (3.1 %) remain above 1 mrad which, although a small fraction of the total, still provide a reasonable number of photons per 0.1% BW in absolute terms. These photons have lower energies

in the range 1-100 eV. The energy binning is the same as in figure 6.5. We define the beam and plasma parameters presented in this section as the 'baseline' simulation for Chapter 6. The simulation studies presented in following sections are parameter scans that vary from this baseline.
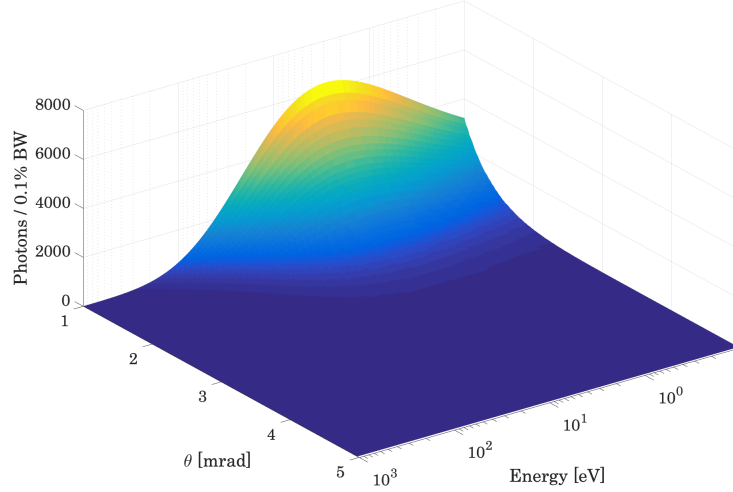
Figure 6.6: The angular spectrum $N(\hbar\omega, \theta)$ ($\theta > 1\,\mathrm{mrad}$) for the baseline Run 2 case with $\sigma_{x,y} = 5.25\,\mu m$.

6.2.2 Radiating beam size

To determine the effect of larger beam radii on the emitted betatron spectrum, the baseline simulation was repeated for a set of larger beam sizes $\sigma_{x,y} = 10\,\mu\mathrm{m}$, $\sigma_{x,y} = 20\,\mu\mathrm{m}$, and $\sigma_{x,y} = 40\,\mu\mathrm{m}$, while keeping all other simulation parameters constant with respect to the baseline case. The resulting angle-integrated spectra are shown in figure 6.7. According to equation (3.17), ω_c should scale linearly with r_β and equivalently with $\sigma_{x,y}$. However, the simulated spectra show only small changes in the critical energy $\hbar\omega_c$ over the simulated range of beam size. Two mechanisms are responsible for this weaker than expected scaling and both limit the energy of emitted photons to produce the simulated spectra: firstly, due to adiabatic damping of $\sigma_{x,y}$ discussed in Chapter 3, the
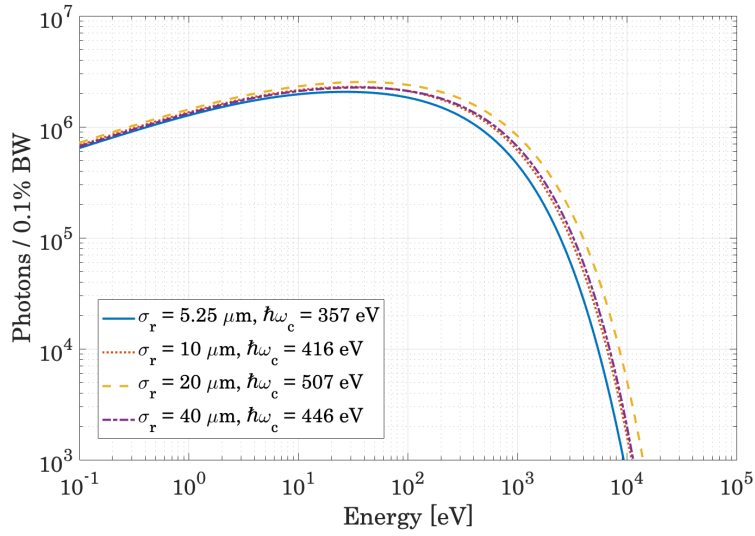
Figure 6.7: The angle-integrated spectra $N(\hbar\omega)$ for the AWAKE Run 2 baseline case scanned over beam size, from $\sigma_{x,y} = 5.25\,\mu m$ to $\sigma_{x,y} = 40\,\mu m$. Each spectrum gives the number of photons in 0.1% bandwidth ($\Delta\hbar\omega = 10^{-3}\hbar\omega$) per photon energy $\hbar\omega$.
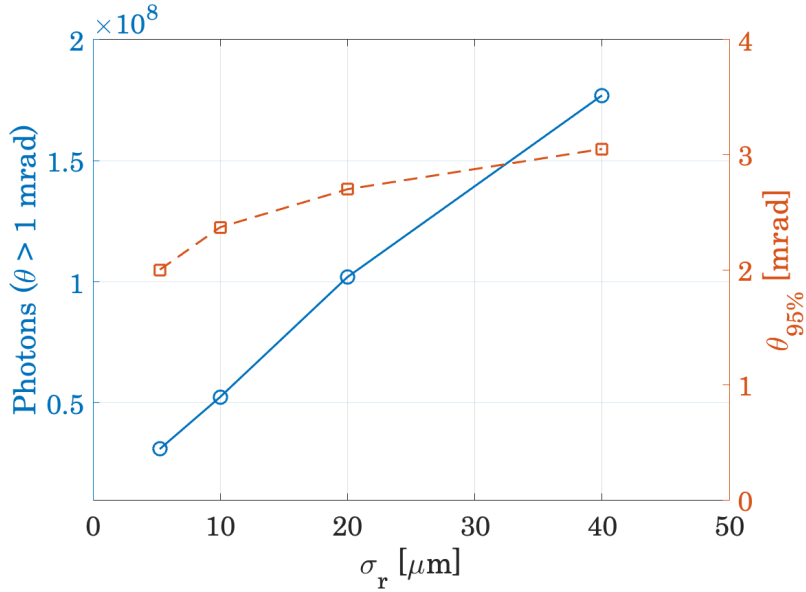
Figure 6.8: The number of photons emitted for $\theta > 1\,mrad$ (solid line) and the radiation divergence $\theta_{95\%}$ as a function of beam size $\sigma_{x,y}$ (dashed line).

beam sizes fall to less than $5\,\mu m$ in all cases. Secondly, an increasing electron beam size results in a falling beam density n_{eb} and ratio n_{eb}/n_e which, since the

132

electron beam blows out its own ion channel, results in an increasingly linear wakefield with weaker transverse forces to drive the betatron motion. With $\sigma_{x,y} = 40\,\mu\text{m}$ the ratio falls to $n_{eb}/n_e = 0.59$, and $\hbar\omega_c$ is lower than the emission from the smaller $\sigma_{x,y} = 20\,\mu\text{m}$ beam. Figure 6.8 shows that neither the number nor divergence of photons emitted into angles $\theta > 1\,\text{mrad}$ have a strong scaling with transverse beam size, although they do increase. The divergence $\theta_{95\%}$ is defined as the angle that contains 95% of the photons remaining above 1 mrad.
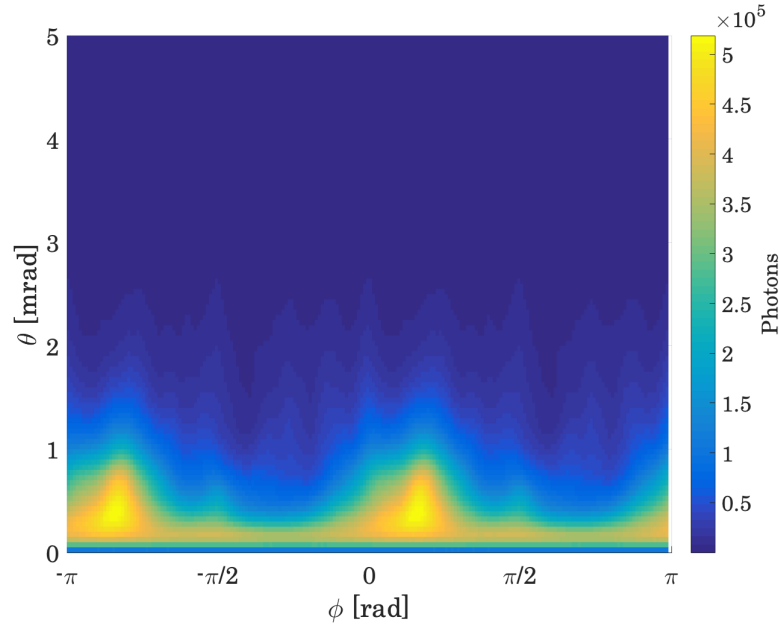
Figure 6.9: The simulated spatial distribution of radiation for the $\sigma_{x,y} = 40\,\mu\text{m}$ beam

The simulated betatron radiation distributed in θ and ϕ is shown in figure 6.9 in the case of the $\sigma_{x,y} = 40\,\mu\text{m}$ beam. Now mismatched, strong envelope oscillations result in the emission of betatron photons in preferential azimuthal directions, in contrast to the matched case seen in figure 6.4.

6.2.3 Plasma density

In Run 1 the AWAKE experiment was operated at plasma densities below the baseline to study the resulting accelerated beam properties, and $n_e = 2 \times 10^{14}\,\mathrm{cm}^{-3}$ was a common working point [27]. The baseline simulation was repeated for plasma densities between $n_e = 2 \times 10^{14}\,\mathrm{cm}^{-3}$ and $n_e = 7 \times 10^{14}\,\mathrm{cm}^{-3}$ in order to estimate the consequent scaling of betatron radiation properties. In order for the beam to remain matched and preserve the beam density the beam dimensions must scale accordingly, with transverse size $\sigma_r \propto \sqrt[4]{n_e}$ via equation (3.13) and length $\sigma_z \propto \sqrt{n_e}$ via λ_p.

Table 6.1: Matched beam dimensions for the simulated set of plasma densities, and the final electron beam size and mean Lorentz factor after 10 m propagation.

$n_e\ [10^{14}\ \mathrm{cm}^{-3}]$	$\sigma_{r_i}\ [\mu\mathrm{m}]$	$\sigma_z\ [\mu\mathrm{m}]$	$\sigma_{r_f}\ [\mu\mathrm{m}]$	$\langle \gamma_f \rangle$
2	7.18	112	4.5	4176
3	6.49	91.1	3.67	4951
4	6.04	79.4	3.28	5576
5	5.71	71.0	3.11	6117
6	5.46	64.8	2.90	6594
7	5.25	60.0	2.85	6988

Table 6.1 lists the new beam dimensions for each density. Also shown are the final beam size σ_{r_f}, having undergone adiabatic damping, and the final mean beam Lorentz factor $\langle \gamma_f \rangle$, where $E_z \propto n_e^{1/2}$. The simulations have the same parameters as the baseline case except the plasma density and beam dimensions shown in table 6.1. Figure 6.10 shows that the total number and critical energy of photons decreases with plasma density, as would be expected. The relative scaling of $\hbar\omega_c$ with n_e from the baseline value of $\hbar\omega_c = 357\,\mathrm{eV}$ is shown in figure 6.11, calculated in simulation.

The simulated critical energies show reasonable agreement with the expected
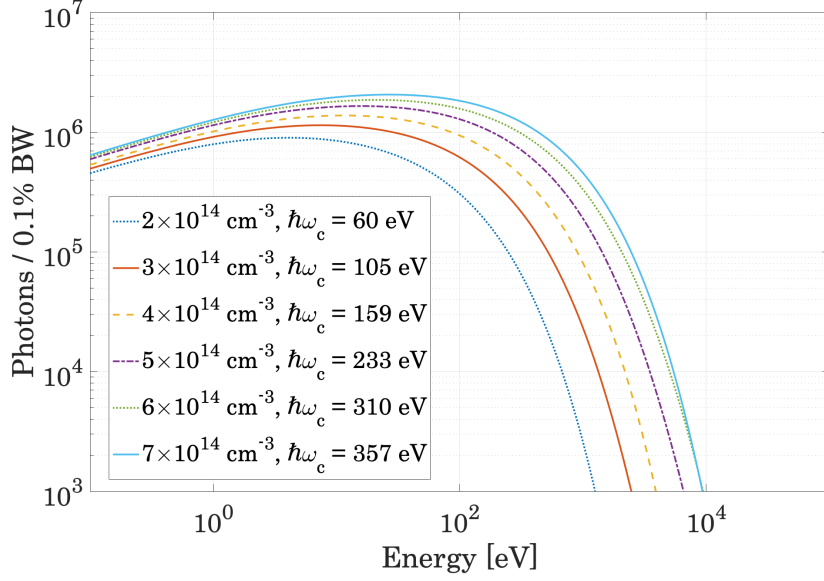
Figure 6.10: Betatron spectra $N(\hbar\omega)$ for a range of plasma densities n_e.

analytical scaling due to the fact that the changing beam dimensions keep the beam density constant with respect to the bulk plasma density ($n_{eb} \sim 34\, n_e$), thereby maintaining a strong blow-out regime. Figure 6.12 shows the angular spectra $N(\hbar\omega, \theta)$ distributed in small angles close to the acceleration axis ($\theta < 1\,\text{mrad}$) for every plasma density. All plots indicate the baseline critical energy and a retreating critical energy that corresponds to each plasma density.

Again the total number of photons can be seen to decrease, whereas their divergence ($\theta \sim \alpha_\beta/\gamma$) only decreases moderately with plasma density; while the strength of transverse motion α_β is weaker, it is offset by the fact that the final beam energy and therefore γ is also smaller for a less dense plasma. The angular photon number integrated over all energies and distributed in θ is shown in figure 6.13, which indicates that the difference in angular photon number between different densities is more obvious at higher angles. On-axis there are $50\,\%$ fewer photons generated by a $n_e = 2 \times 10^{14}\,\text{cm}^{-3}$ plasma compared to the baseline; at $2\,\text{mrad}$ there are $90\,\%$ fewer.

135
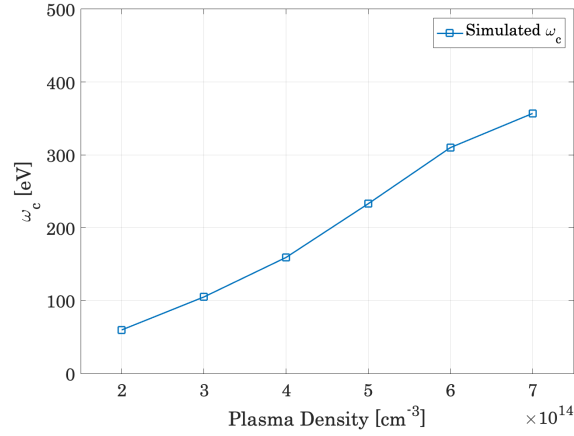
Figure 6.11: Critical energies calculated in simulation.
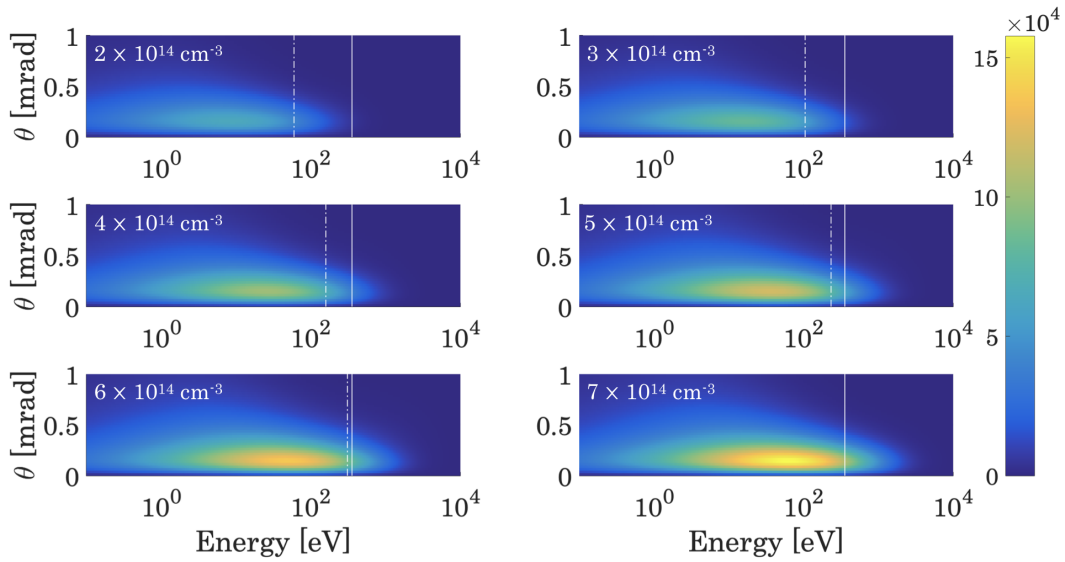
Figure 6.12: Simulated angular spectra $N(\hbar\omega, \theta)$ ($\theta < 1\,mrad$) for a range of plasma densities showing the baseline $\hbar\omega_c$ (solid line) and $\hbar\omega_c$ corresponding to each plasma density (dash-dotted line).
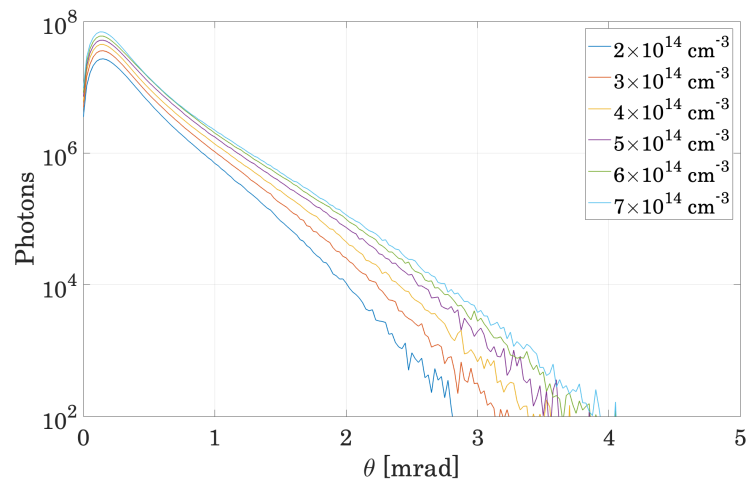
Figure 6.13: Angular photon number $N(\theta)$ for a range of plasma densities.

6.3   Detectable Photons

Betatron emission from LWFAs has been measured with a number of techniques; often directly after the emitting beam has been removed from the accelerating axis by a dipole magnet [123], although it can also be extracted and measured indirectly via a highly oriented pyrolytic graphite (HOPG) crystal [173]. The spectrum can be reconstructed with an x-ray charge-coupled device (CCD) in single-photon counting mode, or with a set of Ross filters. Betatron radiation from a PWFA has also been measured previously [169], although it is significantly less well characterised than the emission from LWFAs.

The AWAKE experiment is a challenging environment for measuring betatron radiation as a substantial x-ray background exists from upstream interaction of SPS protons with the beamline, and because the relativistic proton beam itself is rigid and cannot be transversely kicked to isolate the betatron radiation. Core and defocused protons have a maximum divergence of 1 mrad on exiting the plasma [35] and their presence inhibits a direct, on-axis measurement. However, as shown in figure 6.6, a significant remnant of the emission falls outside 1 mrad. A measurement station 5 m downstream from the accelerating plasma stage with a hole radius corresponding to such an angle, e.g. 5 mm radius at 5 m, would allow the proton beam to pass and enable a partial measurement of the emission, i.e. those photons having energies between 1-100 eV and falling in angles above 1 mrad. A conceptual layout is show in figure 6.14. A combination of conventional Al and multilayered mirrors are readily available to measure the emitted photons with energies in the 1-100 eV range. Multilayered optics could be used to select certain photon energies or, if rotated according to Bragg's law, be used to build a spectrum. Ultraviolet (UV) photons with energies ≥ 3.1 eV cannot propagate in air and require vacuum, further complicating the measurement. The measurement would profit from being split into two phases. First a UV measurement between 200-400 nm
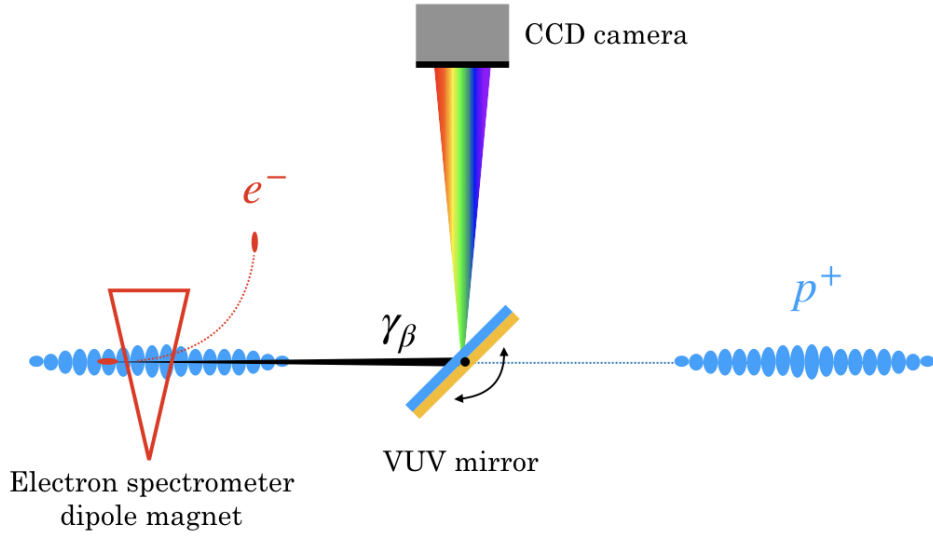
Figure 6.14: Layout for a potential betatron radiation diagnostic for AWAKE Run 2. Electrons e^- are kicked by the energy spectrometer dipole, leaving protons p^+ and betatron radiation γ_β to propagate. An array of on-axis UV-coated Al or multilayered mirrors may be used to pick off betatron photons in the 1-100 eV range, to be detected by a UV-VUV CCD camera.

wavelengths (< 3.1 eV) can be used to extrapolate a spectrum and estimate the beam size σ_r, and would confirm the observation of a significant quantity of betatron radiation. Second, a vacuum UV (VUV) measurement (3.1-100 eV) that provides spectroscopy in a larger range, improving the precision of the fitted spectrum and enabling correlated emittance reconstruction.

A local background of transition radiation from strongly defocused protons (> 1 mrad) striking the UV/VUV optics would reduce the signal to noise ratio on each shot. However this could be addressed by characterising the signal in the absence of accelerated electrons. Finally, due to the x-ray background in the beamline, sensitive cameras should be positioned at some minimum distance from it, which could further reduce the number of detectable photons. Using the photon emission from the baseline simulation ($\sigma_{x,y} = 5.25$ µm, $n_e = 7 \times 10^{14}$ cm^{-3}) in section 6.2.1, it is possible to estimate the number of

detectable photons per unit area of sensor N_d from the total emitted, N_e:

$$N_d = gR_m\delta_\theta N_e, \tag{6.1}$$

where $\delta_\theta = 0.031$ is the fraction of photons falling above 1 mrad, determined in section 6.2.1, and R_m is the fraction reflected by the mirror, assumed to be 0.6. The geometrical factor $g = \delta\Omega/4\pi$ accounts for the loss of photons over a distance r between the mirror surface and the CCD sensor plane. The sensor with area A occupies a solid angle $\delta\Omega = A/r^2$. A VUV CCD camera such as an Andor Newton SO has a sensor area of $178.89\,\mathrm{mm}^2$, and a $26\,\mu\mathrm{m} \times 26\,\mu\mathrm{m}$ pixel size. From the baseline simulation $N_e = 9.83 \times 10^8$ photons, this camera positioned 200 mm from the reflecting mirror should be subject to 6.62×10^3 photons mm^{-2}. With the native pixel area of $6.76 \times 10^{-4}\,\mathrm{mm}^2$ this may be too few photons to register above the noise floor of the CCD sensor. However, with 8×8 pixel binning, the pixel area may be increased to $4.33 \times 10^{-2}\,\mathrm{mm}^2$ and the photons per pixel increased from $\sim$5 to $\sim$286. Finally, assuming the CCD QE ~ 0.6 one could expect $\sim$172 detected photons per binned pixel in the range 1-100 eV. Pixel binning would result in a poorer sensor resolution of $\sim$200 µm, although at 5 m downstream from the accelerator, the radiation divergence of $\theta =$2 mrad for the baseline case, shown in figure 6.8, would produce a relatively large 10 mm spot radius. Only 28 % of the total detectable photons have an energy < 3.1 eV in the baseline case, so a larger sensor may be required for the intial lower energy measurement.

Repeating the calculation for the number of detectable photons for each simulated plasma density reveals how they compare to the noise threshold of the CCD. Figure 6.15 shows the total number of photons emitted N_e, the number of photons emitted above 1 mrad N_θ, the number of detectable photons per square millimeter at the CCD plane given by equation (6.1) N_d, the number of photons per binned pixel (8×8 binning) N_{bp}, and the number of counts per
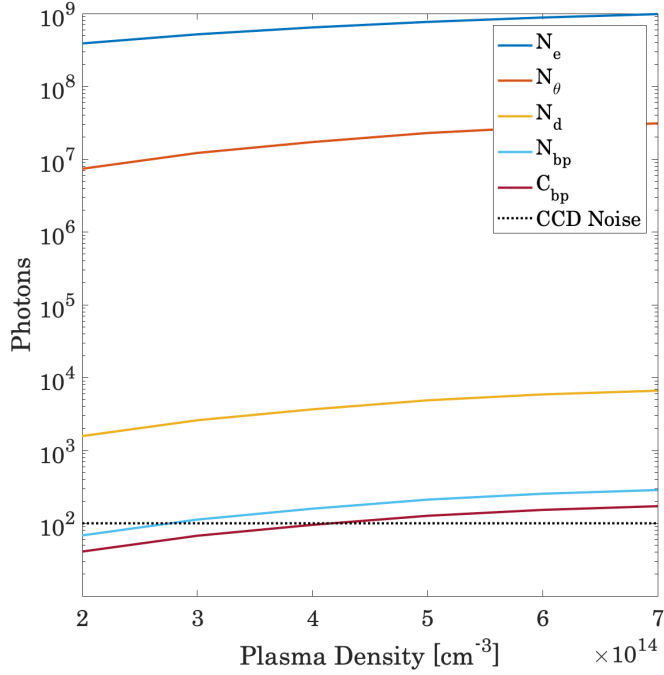
Figure 6.15: Accounting of detectable photons, simulated with respect to plasma density. The dotted line shows the noise floor of the CCD sensor.

binned pixel C_{bp}, given the quantum efficiency of the sensor. For the lowest plasma densities C_{bp} may fall below the noise threshold of the CCD sensor, and higher-order pixel binning would be required.

6.4 Emittance Reconstruction

Using equations (3.16), (3.17), and (3.22) a simple radiation model can be created, with which the proposed emittance reconstruction technique may be demonstrated. We start with a plasma of density $n_e = 1 \times 10^{18}\,\mathrm{cm}^{-3}$, within which a radially symmetric Gaussian electron beam of $\sigma_r = 1.325\,\mu\mathrm{m}$ propagates for one betatron oscillation in a fully blown-out ion channel. The radiating beam has $\gamma = 2000$ and contains $1\,\mathrm{pC}$ of charge (6.25×10^6 electrons). We assume zero energy spread $\sigma_\gamma = 0$, that $\sigma_r \simeq r_{\beta,rms}$, the r.m.s. betatron amplitude, and $\alpha_\beta >> 1$ for most $r_{\beta,i}$. The ion channel is generated by a

separate drive beam, itself with a density n_d such that $n_d/n_e >> 1$. With equation (3.16) a series of synchrotron spectra $S(\omega_j/\omega_{c,i})$ are generated, covering a range of frequencies ω_j and betatron amplitudes $r_{\beta,i}$, which each have a corresponding critical frequency $\omega_{c,i}$ given by equation (3.17).
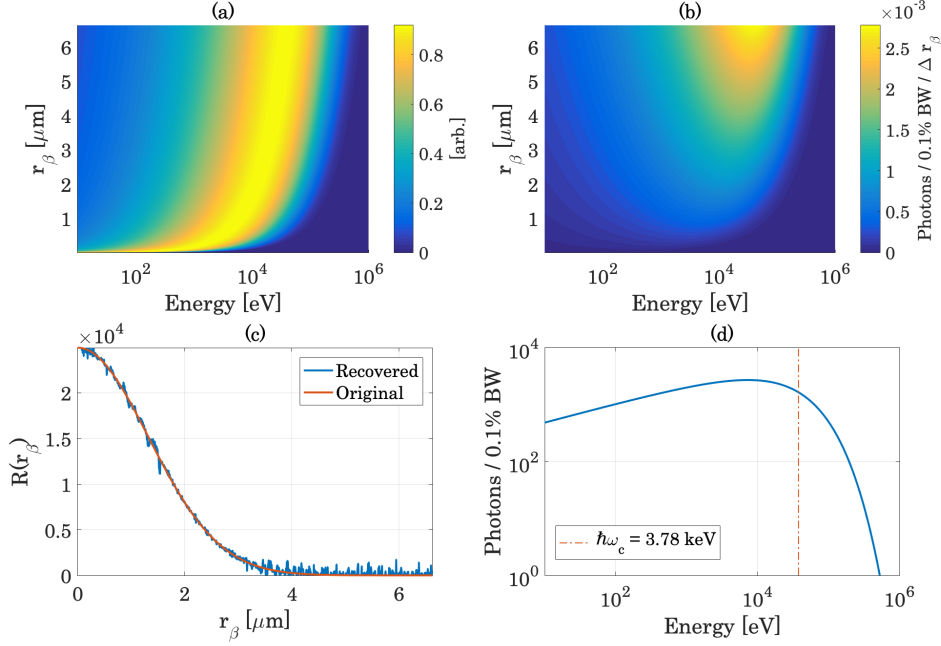
Figure 6.16: (a) The spectral distribution $S(\omega_j/\omega_{c,i})$; (b) the spectral distribution emitted per electron $W_{i,j}$, where $\Delta\hbar\omega = 10^{-3}\hbar\omega$ and $\Delta r_\beta = 10^{-3}r_\beta$; (c) the original and recovered Gaussian beam distribution $R(r_{\beta,i})$; and (d) the total spectrum W_j, the result of populating $W_{i,j}$ and summing over all betatron amplitudes, which has a critical energy $\hbar\omega_c = 3.78\,keV$ (dash-dotted line).

The resulting spectral distribution is shown in figure 6.16(a). Each spectrum $S(\omega/\omega_{c,i})$ is then assigned a number photons, according to its critical energy $\omega_{c,i}$, using equation (3.17), as shown in figure 6.16(b). This spectral distribution $W_{i,j}$ represents the number of photons emitted per electron, in one betatron oscillation, over a range of i betatron amplitudes, and j photon energies ($\hbar\omega_j$). A Gaussian distribution of betatron amplitudes $R(r_{\beta,i})$ with $r_{\beta,rms} = 1.325\,\mu m$ is used to populate $W_{i,j}$ and is shown in figure 6.16(c). Fi-

nally, when summed over all betatron amplitudes $r_{\beta,i}$, a total spectrum W_j is found according to equation (6.2), as seen in figure 6.16(d):

$$W_j = \sum_i R(r_{\beta,i})W_{i,j}. \tag{6.2}$$

The critical energy of W_j is $\hbar\omega_c = \hbar\langle\omega\rangle/(8/15\sqrt{3}) = 3.78\,\text{keV}$, and the spectrum gives the number of photons in 0.1% bandwidth ($\Delta\hbar\omega = 10^{-3}\hbar\omega$) per photon energy $\hbar\omega$. The recovery of a beam profile R from an independently measured betatron spectrum Σ_j and electron energy spectrum Γ (not required for this model with $\sigma_\gamma = 0$) was demonstrated by Curcio et al. (2017) [52], by imposing that the total theoretical spectrum W_j is equal to Σ_j. Inverting equation (6.2) as

$$R(r_{\beta,i}) = \sum_j \Sigma_j W_{i,j}^{-1}, \tag{6.3}$$

enables the reconstruction of a beam profile R from a measured spectrum Σ_j, given an inverse matrix $W_{i,j}^{-1}$, where $W_{i,j}^{-1}$ is the Moore-Penrose pseudoinversion of the radiation model $W_{i,j}$. By considering the modified Lorentz factor due to the relativistic transverse motion, it is possible to approximate the divergence θ due to the betatron motion itself [52]:

$$\theta = \sqrt{\frac{\sqrt{1 + \frac{1}{2}\gamma^2 r_\beta^2 k_\beta^2}}{4\gamma}}r_\beta k_p. \tag{6.4}$$

With a series of weighted positions $x_i = R(r_{\beta,i})$, and corresponding angles $x_i' = \theta(r_{\beta,i})$, the correlated geometric r.m.s. emittance may be calculated via equation (2.3). Testing this procedure by setting $\Sigma_j = W_j$ recovers a beam with a transverse profile (also shown in figure 6.16(c)) which, if it had emitted the spectrum shown in 6.16(d), would have a geometric emittance $\varepsilon_{r.m.s.} =$

2.37×10^{-3} mm mrad and normalised emittance $\varepsilon_n \simeq \gamma\varepsilon_{r.m.s.} = 4.74$ mm mrad. Such a model could be used to reconstruct the transverse normalised emittance of any independently measured betatron spectrum Σ_j so long as the assumptions of the model are fulfilled, i.e. electrons emit in wiggler motion over one betatron period. For the AWAKE case where the emission is integrated over many betatron periods at many different energies an iterated model is required. Furthermore, many electrons in the 1σ beam core have $\alpha_\beta < 1$ and so a model that takes into account single electron motion for the full range of α_β values would provide a greater accuracy.

6.5   Summary

In the next phase of the AWAKE experiment, the accelerated witness beam will emit a significant quantity betatron radiation in the VUV to soft x-ray region, with a critical energy of $\hbar\omega_c = 357$ eV. The radiation will be highly collimated, with the majority of emitted photons falling within 1 mrad from the acceleration axis, a region that cannot be probed as it is occupied by the highly energetic core and defocused protons of the wakefield driver. Betatron radiation from the driver was eliminated to isolate the betatron radiation spectrum from the electron beam. Auxiliary simulations of a lone proton beam that do not artificially increase the proton rest mass, as in the baseline case, show that the betatron radiation it produces is in any case negligible, which is due largely to its much greater mass and similar γ with respect to the electron beam, i.e. with $m_p = 938$ MeVc^{-2} and $\gamma = 426$. However, this simple model is not fully representative of the real microbunched proton beam that undergoes self-modulation and further study under these conditions would be required to be confident in the exclusion of any betatron radiation originating from the proton beam. The small divergence of radiation from the accelerated electron beam is due to the fact that constituent electrons will have weak transverse

144

motion, i.e. $\alpha_\beta \sim 1$.

Despite this, the presented simulation study shows that $3\,\%$ of the total number of emitted photons remain above $1\,\text{mrad}$, providing a detectable quantity of VUV photons with energies between $1\text{-}100\,\text{eV}$. Because larger witness beam sizes are offset by the increasingly linear wakefield they drive, the properties of the radiation do not change appreciably with r.m.s. electron beam size up until $\sigma_{x,y} = 40\,\mu\text{m}$, at which point the number and energy of emitted photons begin to decline.

In the range of operational plasma densities and corresponding matched beam sizes explored in this simulation study, the critical energy and photon number of the resulting betatron emission scale with well-known analytical expressions. For each density the number of photons remain generally sufficient to be detected although lower densities may require specific considerations. A one-dimensional normalised emittance may be reconstructed from a measured betatron and electron energy spectrum alone, and simulations show that it is possible to measure the former in AWAKE Run 2.

Chapter 7

Radiation Reaction and Long-term Acceleration

7.1   Radiative damping in Ion Channels

As discussed in Chapter 3, electrons in ion channels emit synchrotron radiation as a result of their transverse motion, and the force of friction that the emission exerts can affect the energy gain and transverse dynamics of the electron. The radiation reaction force $\vec{F}_R$ felt by an electron as it emits a photon modifies the equations of motion (3.1) and (3.7):

$$\frac{dp_z}{dt} = eE_z + F_{R,z}, \tag{7.1}$$

$$\frac{dp_x}{dt} = -eE_x + F_{R,x}, \tag{7.2}$$

where the components of $\vec{F}_R$

$$F_{R,z} \simeq -m_e c^3 \tau_R \gamma^2 K^4 x^2, \tag{7.3}$$

$$F_{R,x} \simeq -c^2 \tau_R K^2 p_x (1 + K^2 \gamma x^2), \tag{7.4}$$

146

are found by treating the classical radiation reaction force as a perturbation [174], which is delivered in a duration $\tau_R = 2r_e/3c$ corresponding to the classical electron radius r_e. The force constant $K = k_p/\sqrt{2}$ for a pure ion column. The equations of motion (3.3) and (3.9) are then modified as [175]

$$\frac{d\gamma}{dt} = \omega_p \frac{E_z}{E_0} - c^2 \tau_R \gamma^2 K^4 x^2, \tag{7.5}$$

$$\frac{d^2x}{dt^2} + \left(\frac{\omega_p}{\gamma} \frac{E_z}{E_0} + c^2 \tau_R K^2 \right) \frac{dx}{dt} + \frac{\omega_p^2}{2\gamma} x = 0, \tag{7.6}$$

for an ultra-relativistic electron with $v_z \sim c$. The radiation reaction force can therefore significantly modify the evolving properties of a radiating beam of electrons: equation (7.5) shows that the energy loss is a strong function of transverse position x and electrons distributed throughout a bunch will consequently develop an energy spread, while the additional damping term $c^2 \tau_R K^2$ in equation (7.6) means that the beam size will damp faster than in the pure adiabatic case. By considering only the radiation loss term from equation (7.5), the electron Lorentz factor will decrease from an initial value γ_0 as [174]

$$\gamma(t) = \frac{\gamma_0}{1 + \nu_\gamma t} \tag{7.7}$$

where $\nu_\gamma = c^2 \tau_R K^4 x_{\beta_0}^2 \gamma_0/2$ is the radiative loss rate, with the transverse position x averaged over a betatron period as $\langle x \rangle = x_{\beta_0}/\sqrt{2}$. The effects of radiative damping on electron motion may be neglected so long as the interaction time, i.e. the time spent by an electron in an ion channel $\tau \ll \nu_\gamma^{-1}$. This is an equivalent figure of merit to the average energy loss per unit distance, shown in equation (3.20).

7.2 Radiative beam cooling

Because the radiation reaction force enhances damping of the transverse electron motion it leads to the ratio of transverse and longitudinal electron momentum to fall, thereby reducing the two-dimensional transverse normalised emittance ε_n^*, and 'cooling' the beam. It has been shown that the synchrotron radiation loss rate will saturate at a fraction of $2/3$ of the accelerating gradient, irrespective of initial conditions or plasma wakefield properties [175, 176].

Due to this synchrotron emission, the transverse normalised emittance of a particle beam accelerated in a plasma wakefield will decrease as $\varepsilon_n^* \propto \gamma^{-3/2}$, once the electron beam has achieved the very highest beam energies between 1 TeV to 1 PeV, and ε_n^* will continue to decrease until the Coulomb scattering limit [175]. This means that if a sufficient beam energy is reached, sub-micron transverse normalised emittance ε_n^* could be achievable at the end of acceleration, greatly enhancing the luminosity $\mathcal{L}$ at the interaction point of a plasma-based collider which, from equation (1.1), scales as $\mathcal{L} \propto (\sigma_x \sigma_y)^{-1} \propto (\beta^* \varepsilon_n^*)^{-1}$. Because of the single-stage energy gains possible with proton-driven PWFA, the radiative cooling regime may be accessible for an AWAKE-like accelerator. In this chapter a simulation study is used to characterise the threshold energy at which beam cooling is initiated, both for an electron-driven PWFA and a proton-drive PWFA; the radiative cooling of positron beams is also studied.

7.2.1 Electron-driven PWFA

A three-dimensional simulation in the PIC code QV3D was used to study the effects of radiative damping in a fully nonlinear electron-driven PWFA. A drive beam of density n_{db} propagates in a plasma with electron number density $n_e = 1 \times 10^{18}\,\mathrm{cm}^{-3}$, where $n_{db}/n_e = 30$. The driver is a spherical Gaussian beam with dimensions of $\sigma_x = \sigma_y = \sigma_z = 1\,\mathrm{\mu m}$, and initially $\gamma_i = 2 \times 10^4$. A witness beam, initialised with a much lower density $n_{wb} = 0.21 n_e$ so as to only
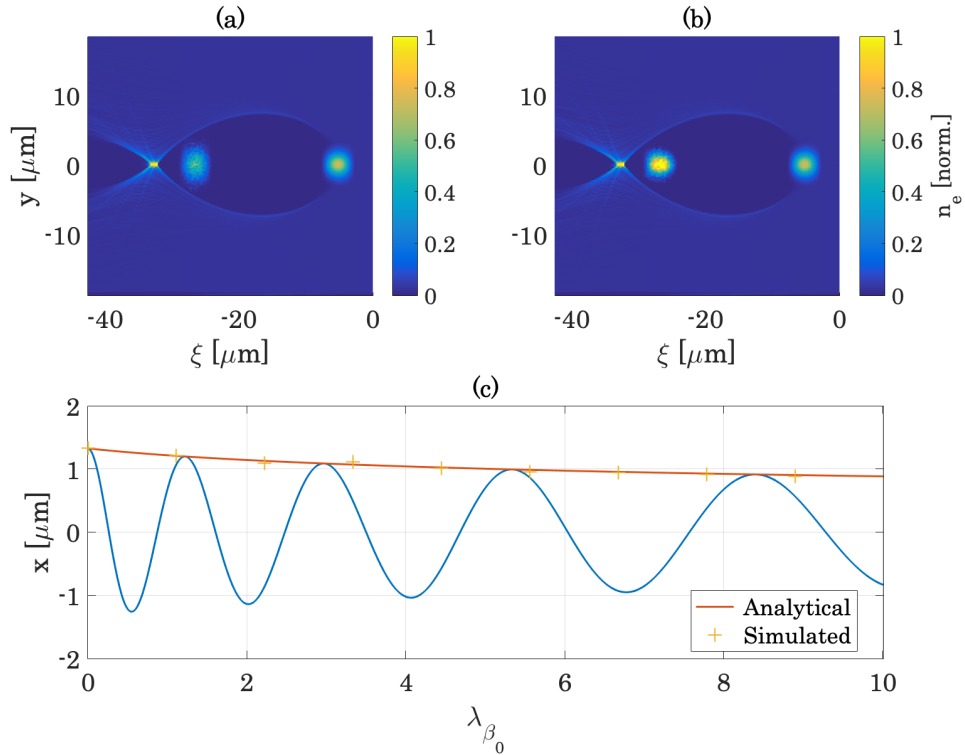
Figure 7.1: *Simulated electron density plots at 0 (a) and 10 $\lambda_{\beta_0} = 4.73\,mm$ (b), with both analytical and simulated electron oscillation amplitude $x_\beta = \sigma_x$ (c). $\xi = z - ct$ is the co-moving coordinate. Witness beam density has been increased by a factor of 100 so that it is visible.*

sample the wakefield and not load it, has dimensions $\sigma_z = 1\,\mu m$ and $\sigma_x = \sigma_y = 1.325\,\mu m$. Initially it has $\sigma_\gamma/\langle\gamma\rangle = 0$, matched emittance $\varepsilon_n^* = 2.33\,mm\,mrad$ and an energy set with $\gamma_i = 100$. Simulations in QV3D were performed with cell sizes of $\Delta x = \Delta y = 0.04\ c/\omega_p$ and $\Delta z = 0.04\ c/\omega_p$ in the transverse and longitudinal directions respectively. Four particles per cell were used for the bulk plasma, which had an electron number density $n_e = 1 \times 10^{18}\,cm^{-3}$. A high density is chosen in order to produce radiation in a strong wiggler regime with $\alpha_\beta >> 1$. This does however necessitate an electron beam with smaller dimensions than would typically be available for electron-driven PWFA experiments. The simulation domain had dimensions of $7 \times 7 \times 8\ c/\omega_p$. The

complete simulation parameters for each study may be found in Appendix A, along with a description of convergence testing.
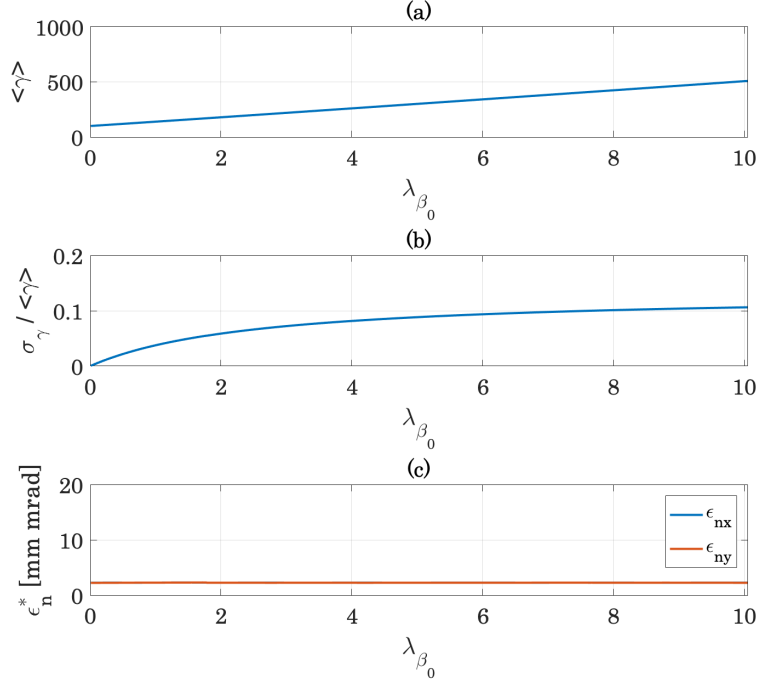
Figure 7.2: Mean beam Lorentz factor (a), relative energy spread (b) and normalised emittance (c) of the $\gamma_i = 100$ (51 MeV) electron beam.

As discussed in Chapter 4, synchrotron radiation calculations are performed analytically in QV3D, and may be turned on or off to study the effects of radiation reaction. Initially simulated with synchrotron radiation turned off, the beam size undergoes normal adiabatic damping over a length corresponding to 10 betatron periods at the starting energy, $\lambda_{\beta_0} = 0.473\,\text{mm}$, and closely follows the $\sigma_x \propto \gamma^{-1/4}$ scaling from analytics as shown in figure 7.1 (c). The electron density plots in figures 7.1(b,c) show the change in witness beam density due to adiabatic damping, and are normalised to 1. The beam dynamics, summarised in figure 7.2, show that the witness electron beam is well matched but does not load the electron-driven wakefield, resulting in a large energy spread

150

that begins to saturate as energy gain sets in.
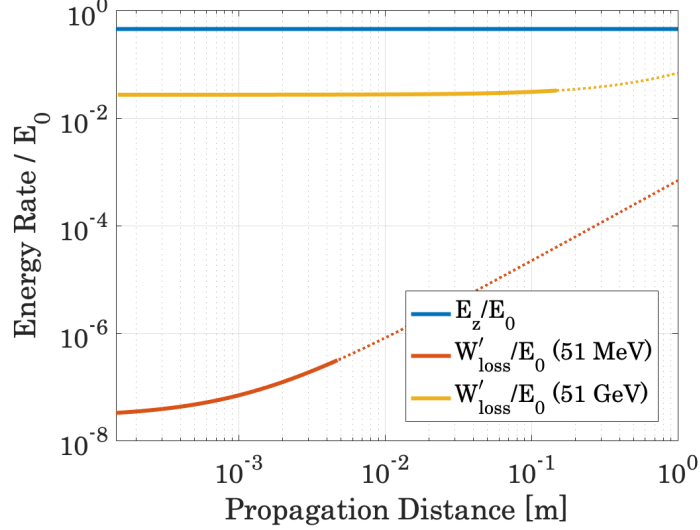
Figure 7.3: Average energy loss rate W'_{loss}, with respect to the propagation distance and compared to accelerating gradient E_z for both the 51 MeV and 51 GeV electron beams. The distance simulated is shown with a solid line, and the distance analytically projected is shown with a dotted line.

The simulation was repeated in QV3D with the synchrotron radiation module turned on, to include radiation reaction, and showed no difference in the evolving beam properties. This is because the beam energy is initially only 51 MeV, and the average energy lost to synchrotron radiation over the acceleration distance W_{loss}, given by equation (3.21), is many orders of magnitude less than the accelerating gradient E_z. Figure 7.3 shows the normalised accelerating gradient E_z/E_0 with the normalised radiated energy loss per unit distance W'_{loss}/E_0 in this case. The solid line indicates the distance simulated, and the dotted line is the analytically projected energy loss over the remaining distance. Analytical calculations for W'_{loss} used the adiabatically damped radiating beam size only. This will transition to the radiatively damped case above a certain energy, determined by Deng et al. (2012) [175], further limiting the energy loss such that W'_{loss} does not continue to grow beyond E_z. At the end

of the simulated acceleration to $\sim 250\,\text{MeV}$, W'_{loss}/E_0 is still insignificant, and this remains the case for a full metre. Consequently the beam dynamics are unchanged between simulations both with radiation reaction and without it, for a 51 MeV beam. Also shown in figure 7.3 is W'_{loss}/E_0 for an electron beam with an initial Lorentz factor $\gamma_i = 1 \times 10^5$ (51 GeV), which results in a radiated energy loss that is a significant fraction of the accelerating gradient. A second simulation was conducted where the witness beam energy was increased to this higher energy, and the beam dynamics in this case are shown in figure 7.4, both where radiation reaction was included in the simulation (RR1) and where it was not (RR0).

(a) Mean Lorentz factor

(b) Relative energy spread

(c) Transverse normalised emittance
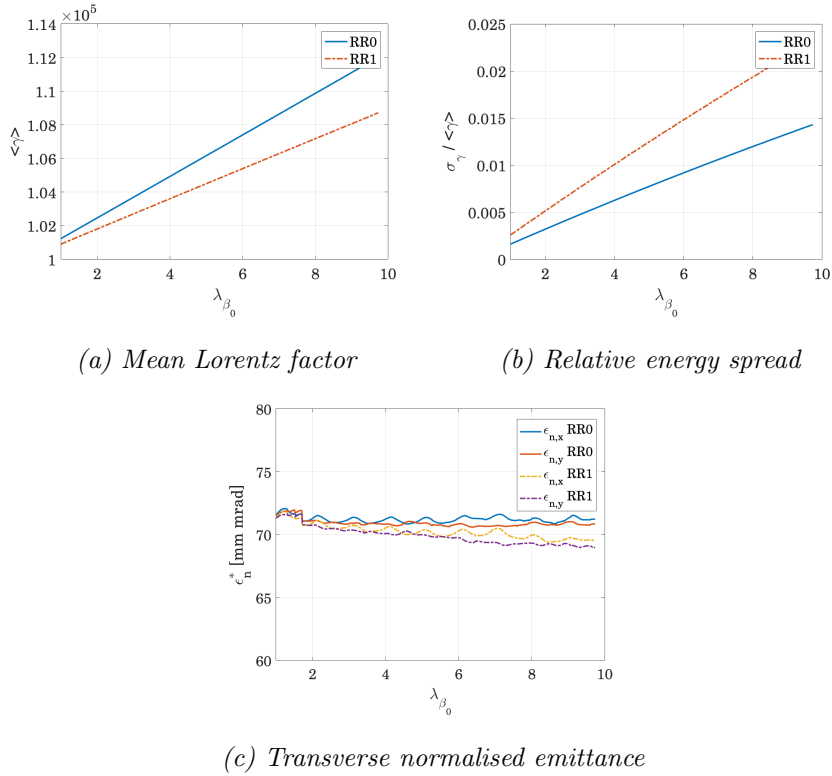
Figure 7.4: Simulated dynamics of a 51 GeV electron beam with (RR1) and without (RR0) radiation reaction.

At this higher beam energy the betatron period $\lambda_\beta = 2\pi\sqrt{2\gamma}c/\omega_p$ is longer and now $\lambda_{\beta_0} = 1.5\,\text{cm}$. The simulation was propagated over a longer distance

so that again we see the beam dynamics over $10\,\lambda_{\beta_0}$. Immediately the effects of the strong emission, where $W'_{loss} \to E_z$, are clear: $\langle\gamma\rangle$ is lower, corresponding to the lost energy, and the relative energy spread $\sigma_\gamma/\langle\gamma\rangle$ has increased faster over the same distance. This, as can be seen in equation (3.19), is because electrons at higher transverse positions will lose more energy than those in the beam core. The additional energy spread is equivalent to W_{loss}, the average total energy lost to radiation during the acceleration. Figure 7.4 (c) shows that the normalised emittance has fallen due to radiative damping, effectively cooling the beam. In this case $\chi \simeq 1 \times 10^{-3}$, and is still within the limit of classical radiation.

7.2.2   Proton-driven PWFA

To study the equivalent situation for the dynamics of an electron beam in a proton-driven plasma wakefield, a simulation reproducing the original model for proton-driven plasma wakefield acceleration used by Caldwell et al. (2009) [28] was conducted. The plasma density is set to the AWAKE baseline value of $n_e = 7 \times 10^{14}\,\mathrm{cm}^{-3}$ and in this scenario a $10\,\mathrm{GeV}$ electron beam is injected into a wakefield driven by a Gaussian proton beam with dimensions $\sigma_z = 40\,\mathrm{\mu m}$ and $\sigma_x = \sigma_y = 200\,\mathrm{\mu m}$, with a density $n_{pb} = 5n_e$. Proton-driven PWFA necessitates low-density plasma because the scale of the driving beam must be similar to that of plasma wavelength in order to drive high-amplitude plasma waves, and short proton beams for high density plasma are challenging to generate with current longitudinal bunch compression methods. As discussed in section 1.2, it is for this reason that the SSM mechanism is used to modulate the proton driver at the AWAKE experiment. A short proton beam is chosen regardless in order to study the dynamics of the electron beam in this particular case. The witness electron beam dimensions are $\sigma_z = 60\,\mathrm{\mu m}$ and $\sigma_x = \sigma_y = 52.5\,\mathrm{\mu m}$. A large transverse beam size was chosen to enhance the radiated energy loss rate. Initially it has $\sigma_\gamma/\langle\gamma\rangle = 0.1\,\%$, matched emittance $\varepsilon_n^* =$

153
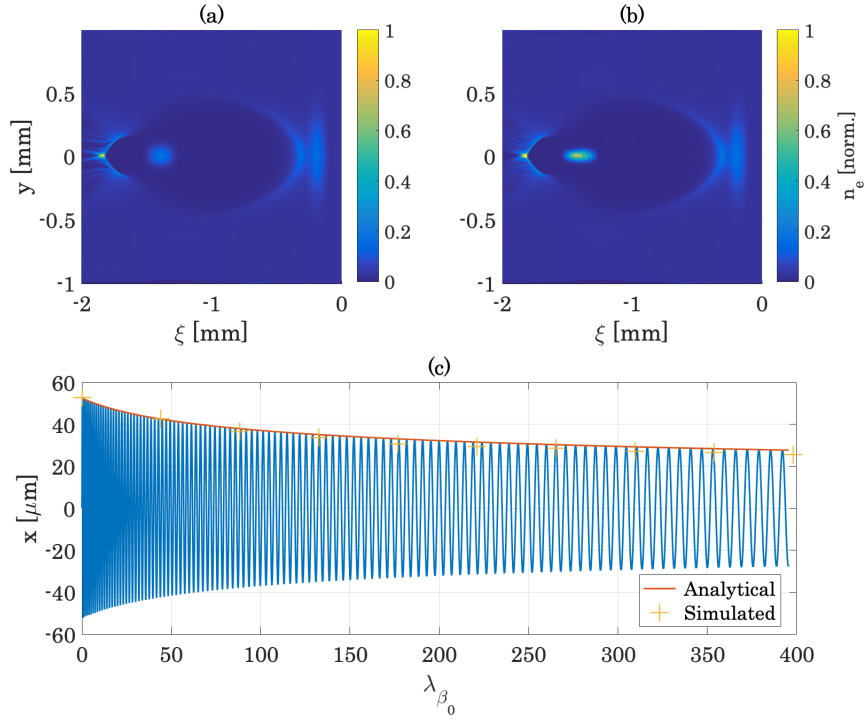
Figure 7.5: Simulated electron density plots at 0 (a) and 400 λ_{β_0} = 100 m (b), with both analytical and simulated electron oscillation amplitude $x_\beta = \sigma_x$ (c). $\xi = z - ct$ is the co-moving coordinate.

1000 mm mrad and an energy set with $\gamma_i = 2 \times 10^4$. Simulations in QV3D were performed with cell sizes of $\Delta x = \Delta y = 0.05 \, c/\omega_p$ and $\Delta z = 0.05 \, c/\omega_p$ in the transverse and longitudinal directions respectively. Four particles per cell were used for the bulk plasma and the simulation domain had dimensions of $10 \times 10 \times 10 \, c/\omega_p$. The simulation was tracked over 400 λ_{β_0}, corresponding to 100 m. Figure 7.5 shows that the simulated transverse beam size generally agrees with the expected analytical scaling over the propagation distance but begins to diverge, with a 7 % difference in the final beam size. The difference is likely due to the fact that the accelerator is not in the full blow-out regime, with $n_{pb}/n_e = 5$. Despite the high witness beam energy and large beam size, the relatively low plasma density means that radiation reaction effects have no discernible impact on the electron beam dynamics, which are summarised in

154

(a) Mean Lorentz factor

(b) Relative energy spread

(c) Transverse normalised emittance
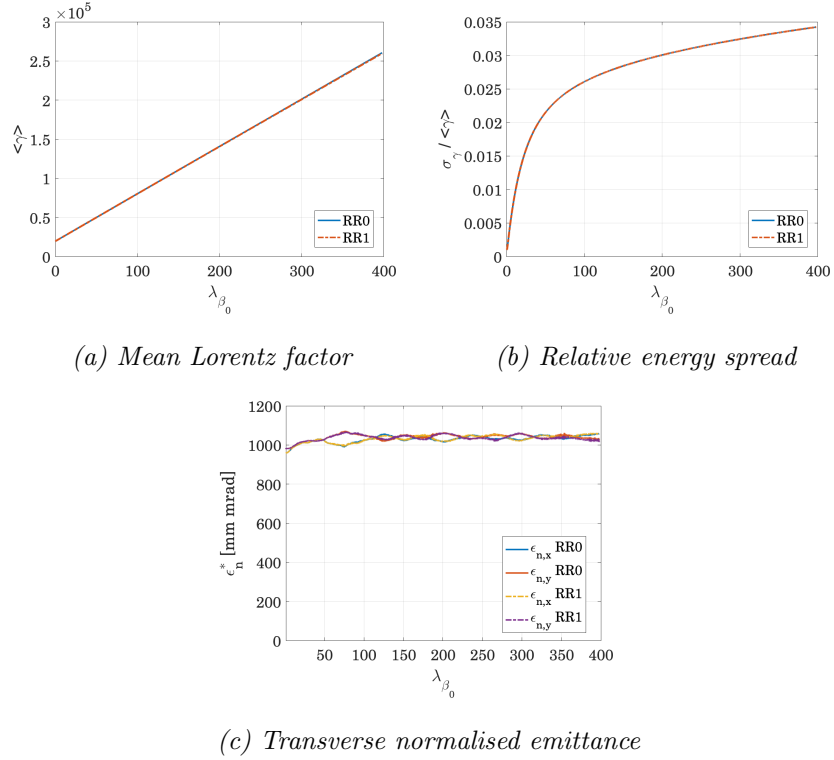
Figure 7.6: Simulated dynamics of a 10 GeV electron beam with (RR1) and without (RR0) radiation reaction.

figure 7.6; in the RR1 case the beam retains $99.7\,\%$ of the energy it has in the case without radiation reaction, RR0. For the parameters of this simulation, the transition from adiabatic damping to radiative damping occurs at a beam energy $\sim 0.848\,\text{TeV}$ ($\gamma = 1.66 \times 10^6$) according to the scaling derived by Deng et al. (2012) [175], which for the above case would require an acceleration length of $696\,\text{m}$. Therefore, radiative beam cooling could certainly impact the evolving beam dynamics of a future proton-driven PWFA accelerator that delivers frontier energy TeV beams, although the distance for radiative cooling to become significant would be greater for electron beams that had a lower initial normalised emittance.

7.2.3 Radiative Positron Beam Cooling

Any future electron–positron e^-e^+ collider using plasma wakefield accelerator technology must also be able to provide a source of high energy and high quality positrons. This presents a challenge because there are limitations for the acceleration of positron beams in both linear and nonlinear plasma wakefields. In the linear case the accelerating and focusing region of the wakefield for a positron is simply a phase change of π with respect to the accelerating and focusing region for an electron, due to its opposite charge.

However, matching a beam to such a wakefield with a sufficiently small emittance acceptable for colliders requires a small beam size, and therefore a high density beam. This would overload the linear wakefield, reducing the efficiency of the acceleration. In the second nonlinear case the plasma wakefield has a totally asymmetric response to positrons as plasma electrons are drawn in strongly towards positively charged positrons. This means that for an electron-driven PWFA in the nonlinear blow-out regime there is only a small region of simultaneous focusing and acceleration for a witness positron beam. Furthermore, within this region the focusing is nonlinear and varies with transverse position – in contrast to the ideal emittance preserving characteristic of the nonlinear blow-out regime for electrons.

As discussed in Chapter 2, efficient energy gain of positrons was demonstrated for a positron-driven PWFA where some parts of the driving beam tail were accelerated [138], and hollow plasma channels have been shown to remove the deleterious transverse forces altogether [139]. In this section we study the compensating effect of radiative emittance cooling on the nonlinear focusing force experienced by a positron witness beam in a nonlinear electron-driven PWFA. The simulation used in section 7.2.1 was repeated with the witness electron beam replaced by an identical positron beam, and propagated over twice the distance (30 cm). As can be seen in figure 7.7(a) the witness beam
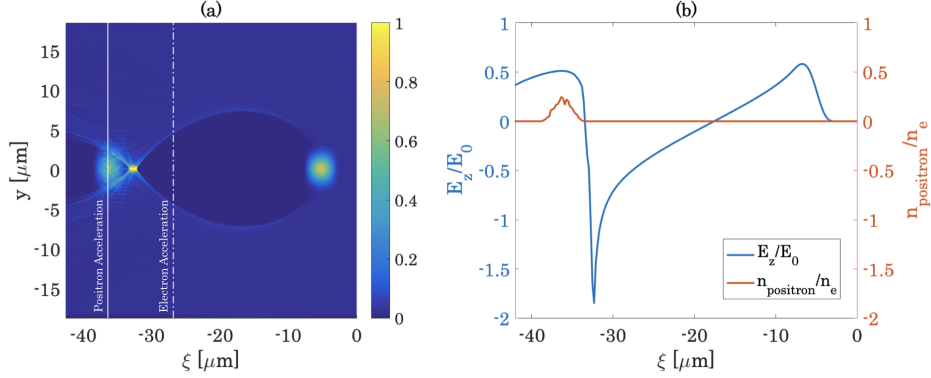
Figure 7.7: Simulated density plot of an electron-driven nonlinear PWFA with a positron witness beam (a), showing the positron (solid line) and electron (dash-dotted line) accelerating locations. The longitudinal accelerating field E_z and beam density are shown in (b). $\xi = z - ct$ is the co-moving coordinate.

was initialised in a new longitudinal position $\xi_0 = -36\,\mu\text{m}$ behind the drive beam that corresponds to acceleration for positrons, also shown is the position used for electron acceleration in section 7.2.1, which lies at $\xi_0 = -26.5\,\mu\text{m}$. Figure 7.7(b) shows the beam position with respect to the accelerating field E_z. The radial focusing field at these two locations is significantly different: figure 7.8 plots E_r at both locations in the transverse vertical direction y, indicating that electrons experience a linear uniform transverse field within the ion channel while positrons are subject to a nonlinear field which varies in radial direction outside of the channel, which dilutes the positron beam emittance. Additionally, the linear uniform field extends over a range of transverse positions within the ion channel, such that all electrons within a witness beam experience the same focusing force.

The positron beam is strongly modulated in the transverse direction as it is accelerated over 30 cm, producing a focused beam core and a defocused halo shown in figure 7.9. The simulated positron beam dynamics are summarised in figure 7.10 both where radiation reaction was included in the simulation (RR1) and where it was not (RR0). The radiating beam loses a significant amount of
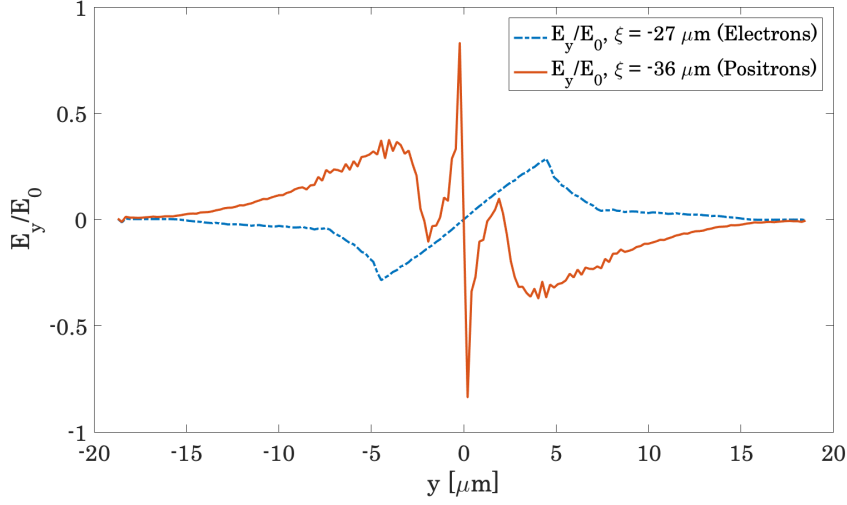
Figure 7.8: Vertical focusing field E_y at the positron (solid line) and electron (dash-dotted line) accelerating position.

energy and gains a larger energy spread with respect to the non-radiating beam. Both show a large initial growth in two-dimensional transverse emittance ε_n^* due to nonlinear focusing but, as the emittance increases for the RR0 beam, its growth is suppressed for the RR1 case. Beam loading may be improved to further suppress the growth relative energy spread $\sigma_\gamma/\langle\gamma\rangle$, although as the beam is accelerated to higher energies the relative energy spread will decrease naturally; figure 7.10(b) shows that the growth rate is slowing, even in the RR1 case.
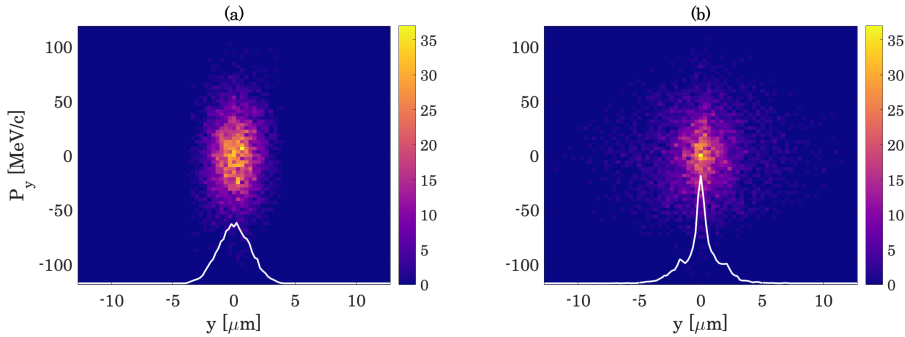
Figure 7.9: Simulated positron beam phase space initially (a) and after 30 cm propagation (b). Beam transverse projections in the vertical y direction are overlaid.

(a) Mean Lorentz factor

(b) Relative energy spread

(c) Transverse normalised emittance
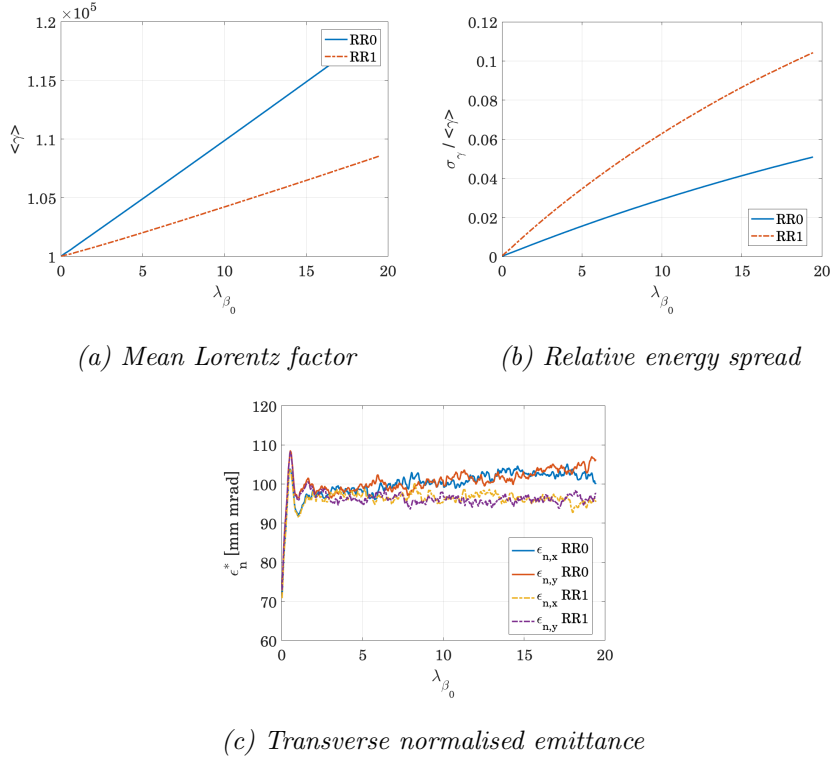
Figure 7.10: Simulated dynamics of a 51 GeV positron beam with (RR1) and without (RR0) radiation reaction.

7.3 Summary

Radiation reaction enhances the inherent adiabatic transverse damping of particle beams as they are accelerated in a plasma wakefield, and is a source of energy loss. Because the radiated power is a strong function of transverse position, radiation reaction can induce a large energy spread for a beam with finite transverse size. As the beam energy increases during acceleration, a transition point is reached where radiation damping becomes dominant over adiabatic damping, which results in a reducing beam emittance that is limited only by Coulomb scattering with plasma species; the maximum radiated energy loss is less than the energy gained in acceleration [176, 175]. Such a radiation damping regime is accessible to a proton-driven PWFA, however, due to the low plasma density necessitated by the proton-driven scheme, it requires TeV

beam energies and a multi–km–long acceleration length for the effects of radiation damping to become apparent. Potentially, an electron-positron collider could profit from radiative emittance cooling to the sub–mm mrad level at the interaction point.

In this chapter radiative emittance cooling of positrons in a nonlinear PWFA has been shown to suppress the emittance growth due to nonlinear defocusing forces, in simulation. This scheme could provide a way to obtain high quality positron beams using a PWFA design without special considerations for electrons or positrons other than a change in driver and witness spacing, albeit with reduced energy gain for accelerated positrons. Emittance reduction was not necessarily shown in the presented simulations, but it could be possible given a sufficiently long acceleration length. Radiative positron beam cooling was shown for an electron-driven PWFA, but it could also be possible for a proton-driven accelerator, given sufficient energy gain. Although radiation reaction negatively effects the energy spread and gain of a positron beam, such challenges could to an extent be mitigated over long-term acceleration and with a correctly beam loaded wakefield.

Chapter 8

Conclusions and Discussion

Plasma wakefield accelerators offer valuable new capabilities for high energy particle accelerators, which could either reduce the footprint of existing facilities when replacing conventional accelerator technology, or produce particle beams with entirely novel properties [115].

High gradient acceleration will reduce the cost of reaching the energy frontier in high energy particle colliders, enabling the study of new physics and aid in the search for new particles such as dark matter candidates. Particle energy is however far from the only important consideration and a number of limitations must be overcome before plasma wakefield accelerators are able to supplant metallic cavity accelerators.

Beam emittance and energy spread must be kept to a low level to aid transport throughout the accelerator and to maximise the luminosity at the interaction point. While initial costs of a plasma wakefield accelerator may be lower by virtue of its smaller size, without an improvement of wall-plug-to-beam energy efficiency their operating costs could exceed that for a conventional RF accelerator. The adoption of fibre lasers [177] in high average power systems could improve the efficiency of plasma-based accelerators, as could novel LWFA

schemes using multiple laser pulses to excite wakefields [178]. The beam repetition rate must also reach parity with conventional accelerators to increase the integrated luminosity, increasing the chance to observe rare processes.

A collider relying on laser or electron-driven plasma wakefield acceleration would require multiple stages in order to address the energy gain limit set by driver depletion [16]. In contrast, a proton driver could avoid these challenges since it carries significantly more energy and can drive wakefields over much greater distances, potentially accelerating electron beams to the tera-electronvolt-scale in a single stage [28]. This greatly reduces the complexity of a plasma-based collider. The acceleration of electrons in a proton-driven plasma wakefield has been achieved [27], marking the first step in demonstrating this technology. The next stage is to demonstrate that the beam quality of injected electrons can be preserved throughout the acceleration process. This thesis has evaluated methods to generate and diagnose electron beams with properties that enable beam quality preserving acceleration in a proton-driven plasma wakefield, and has shown the impact of radiation reaction on the long term evolution of electron beam dynamics in such a wakefield.

A shock–front injected laser–driven plasma wakefield accelerator produces stable and tunable electron beams in a compact arrangement [118]. Two-dimensional simulations in the PIC code EPOCH presented in this thesis show that with a 43 TW laser system the required electron beam energy and charge at injection can be met and provided reproducibly by an LWFA electron source. The high charge and short duration will however result in a beam current that overloads the proton-driven wakefield. The beam does not undergo significant longitudinal decompression as it propagates in vacuum and will require longitudinal stretching. A compact permanent magnetic quadrupole triplet was designed to match the electron beam to the proton-driven plasma wakefield, which, given the relatively large LWFA-generated energy spread, is unable

to focus the beam size to less than 10 μm. However, electron beam parameters from an LWFA injector would be flexible enough to meet the goals of the AWAKE experiment in Run 2. Longitudinal stretching may be accomplished simultaneously as the beam is transported horizontally to the main proton beamline with a magnetic dipole chicane, however CSR effects must be addressed for such a short duration electron beam.

Betatron radiation spectroscopy may be used to measure the emittance of electron beams accelerated in a plasma wakefield, using only the measured betatron spectrum and electron energy spectrum [52]. In this thesis the feasibility of such a measurement for a proton-driven PWFA was explored. Three-dimensional quasi-static simulations in the PIC code QV3D show that the expected betatron radiation emission from an electron accelerated in a proton-driven PWFA is found to be comprised of a significant and measureable quantity of VUV to soft x-ray photons, which would enable a non-intercepting emittance measurement. The properties of the emission are relatively insensitive to electron beam size as a less dense beam excites a weaker local wakefield, which offsets the expected gain in the quantity and energy of photons emitted by a wider beam that contains electrons with larger betatron amplitudes. The betatron radiation properties vary as expected with plasma density. Across all likely operational plasma densities for a 10-metre-long proton-driven PWFA, the majority of photons have energies within the range 1-100 eV, and spectroscopy using multilayered VUV mirrors in this range could therefore facilitate the reconstruction of transverse beam emittance. Camera positioning to optimise signal to noise ratio is a central technical challenge to be addressed.

Radiative damping can lead to emittance cooling of electron beams accelerated in plasma wakefield accelerators [174, 176, 175]. In this thesis three-dimensional quasi-static simulations with the PIC code QV3D have been used to show that there are no significant advantages or disadvantages from radia-

tive damping for a proton-driven PWFA up to at least beam energies on the 100 GeV-scale. The radiative damping regime required for beam cooling will only occur for the low plasma densities used for a proton-driven PWFA after a witness beam energy of 848 GeV, corresponding to $\sim$700 m. This distance may be reduced by using a higher plasma density, although this requires a proton beam of smaller dimension, which is technically challenging to realise. Additionally, radiative damping of positrons in a nonlinear electron-driven PWFA has been demonstrated in simulation. Plasma-based electron-positron colliders must be able to generate high energy and high quality positron beams but, due to the asymmetric response of a positron beam to a nonlinear plasma wakefield, there is no simultaneously emittance preserving and accelerating phase within it. In this thesis radiative damping has been shown to modify the emittance of a positron beam accelerated in a nonlinear electron-driven plasma wakefield, specifically by suppressing emittance growth. For a sufficiently long acceleration length the emittance growth may be reversed, but this was not shown in the presented simulations. A plasma-based collider that relies on a radiatively cooled positron beam could potentially use the same acceleration scheme for both electrons and positrons by repositioning the witness positron beam with respect to the accelerating wakefield, greatly simplifying the design of a plasma based electron–positron collider. Such a positron beam would however gain less energy and develop a greater energy spread than its electron beam counterpart.

Appendices

Appendix A

Simulation Parameters

In the following set of tables the simulation parameters, used in each of the studies presented in Chapters 5–7, are summarised. They are not exhaustive, but demonstrate the resolution of the simulations and quantity of macroparticles they involve. Parameters of interest, i.e. those parameters specifically varied to study the relationship between them and the resulting accelerated beam or synchrotron radiation properties, are also included.

Table A.1 summarises the simulations for Chapter 5 and lists the driving laser central wavelength λ_l, plasma density in the plateau region n_e, size and number of cells in the transverse and longitudinal directions Δy, Δz, Y, Z, and number of macroparticles in the bulk plasma N. Also shown are the normalised laser vector potential and plateau length used in the parameter scans. The longitudinal resolution yielded 40 cells per laser wavelength, the smallest feature to resolve in a laser-plasma accelerator. Convergence testing in the EPOCH simulation was carried out by increasing the number of cells in the transverse y direction up to a factor of 2.5 with respect to the number used in the baseline simulation, i.e. from 600 to 1500 cells. The electron beam in this highest resolution simulation had an average energy $\langle E \rangle =$

110.1 MeV, and contained 111.6 pC of charge, while as previously stated the electron beam from the baseline simulation had $\langle E \rangle = 112.7$ MeV and contained 115 pC. Therefore the resolution used for the baseline simulation, also used for the parameter scans that followed in sections 5.3.2 and 5.3.3, is considered high enough to capture sufficient physical detail as there is little difference in the resulting electron beam parameters. At the same time, a simulation executed with the baseline resolution does not have an excessive computational demand and completes within a reasonable time. Particle–in–cell simulations generally must strike a balance between physical accuracy and the volume of computational work they require.

Table A.2 summarises the simulations for Chapter 6 and lists the transverse beam size of the radiating witness beam σ_r, plasma density n_e, size and number of cells in the transverse and longitudinal directions Δx, Δy, Δz, X, Y, Z, and number of macroparticles in the bulk plasma N. Also shown are the radiating witness beam sizes and plasma densities used in the parameter scans. In simulation of a beam–plasma accelerator the smallest features to resolve are the plasma wavelength and the size of the beams themselves. The presented simulations in Chapter 6 had a transverse cell size of 2 μm, which provided 2.625 cells per beam sigma for the smallest beam considered with r.m.s. size $\sigma_x = 5.25$ μm. Convergence testing was carried out with up to ten times more cells in the simulation, which were distributed in the longitudinal direction, i.e. the longitudinal cell size was decreased to $\Delta z = 0.01 \ c/\omega_p$ with respect to the Chapter 6 baseline simulation. This high–resolution variant produced an accelerating field with a peak value of 362 MVm^{-1}, compared to 355 MVm^{-1} generated by the baseline simulation. The baseline simulation retained 98.5 % of the witness electron beam charge found in the high–resolution variant. Consequently, the baseline simulation parameters are considered to provide sufficient accuracy. Convergence testing in the temporal dimension was also carried out in order to find the maximum permissible timestep, thereby allowing the

simulation to progress more quickly while still resolving the betatron motion of beam electrons oscillating the plasma wakefield.

Tables A.3–A.5 show the parameters for the simulations presented in Chapter 7 and include the longitudinal positions of the witness electron and positron beams in the simulated electron-driven wakefield. Convergence testing in this case was carried out in a similar manner to Chapter 6.

Table A.1: Chapter 5 simulation parameters

	λ_l [µm]	n_e [cm^{-3}]	λ_p [µm]	Δy [µm]	Δz [µm]	Y	Z	N
5.3.1 Baseline Case	0.8	5.4×10^{18}	14.4	0.1	0.02	600	3000	9×10^6

	a_0^{min}	a_0^{max}	Points
5.3.2 Laser Vector Potential	2.2	2.5	3

	L_p^{min} [µm]	L_p^{max} [µm]	Points
5.3.3 Plateau Length	280	780	6

Table A.2: Chapter 6 simulation parameters

	σ_r [µm]	n_e [cm^{-3}]	λ_p [mm]	Δx [c/ω_p]	Δy [c/ω_p]	Δz [c/ω_p]
6.2.1 Baseline Case	5.25	7×10^{14}	1.26	0.01	0.01	0.1
	X	Y	Z	N	c/ω_p [µm]	
6.2.1 Baseline Case	500	500	100	1×10^{8}	201	
	σ_r^{min} [µm]	σ_r^{max} [µm]	Points			
6.2.2 Radiating Beam Size	5.25	40	4			
	n_e^{min} [cm^{-3}]	n_e^{max} [cm^{-3}]	Points			
6.2.3 Plasma Density	2×10^{14}	7×10^{14}	6			

Table A.3: Chapter 7 simulation parameters

7.2.1	σ_r [μm]	n_e [cm^{-3}]	λ_p [μm]	Δx [c/ω_p]	Δy [c/ω_p]	Δz [c/ω_p]
Electron-driven PWFA	1.325	1×10^{18}	33.4	0.04	0.04	0.04

7.2.1	X	Y	Z	N	ξ_0 [μm]	c/ω_p [μm]
Electron-driven PWFA	175	175	200	2.45×10^7	-26.5	5.32

Table A.4: Chapter 7 simulation parameters continued

7.2.2	σ_r [μm]	n_e [cm^{-3}]	λ_p [mm]	Δx [c/ω_p]	Δy [c/ω_p]	Δz [c/ω_p]
Proton-driven PWFA	52.5	7×10^{14}	1.26	0.05	0.05	0.05

7.2.2	X	Y	Z	N	c/ω_p [μm]
Proton-driven PWFA	200	200	200	3.2×10^7	201

Table A.5: Chapter 7 simulation parameters continued

7.2.3	σ_r [μm]	n_e [cm^{-3}]	λ_p [μm]	Δx [c/ω_p]	Δy [c/ω_p]	Δz [c/ω_p]
PWFA Positron Witness	1.325	1×10^{18}	33.4	0.04	0.04	0.04

7.2.3	X	Y	Z	N	ξ_0 [μm]	c/ω_p [μm]
PWFA Positron Witness	175	175	200	2.45×10^7	-36	5.32

Bibliography

[1] The ATLAS Collaboration. Observation of a new particle in the search for the Standard Model Higgs boson with the ATLAS detector at the LHC. *Physics Letters B* **4** (2012).

[2] Bertrand, L. *et al.* Cultural heritage and archaeology materials studied by synchrotron spectroscopy and imaging. *Appl. Phys. A Mater. Sci. Process.* **106**, 377–396 (2012).

[3] Levin, W., Kooy, H., Loeffler, J. & DeLaney, T. Proton beam therapy. *British journal of Cancer* **93**, 849–854 (2005).

[4] CERN. LEP Design Report - Volume II: The LEP Main Ring (1984).

[5] Talman, R. Scaling Behaviour of Circular Colliders Dominated by Synchrotron Radiation. *International Journal of Modern Physics A* **30** (2015).

[6] CLIC Collaboration. *CLIC Conceptual Design Report* (CERN, Geneva, 2012).

[7] Wang, J. W. & Loew, G. A. Field emission and rf breakdown in high gradient room temperature linac structures. Tech. Rep., Stanford Univ., Stanford Linear Accelerator Center, CA (US) (1997).

[8] Benedikt, M. *et al.* Future Circular Collider. Tech. Rep. CERN-ACC-2018-0057, CERN, Geneva (2018). Published in Eur. Phys. J. ST.

174

[9] Veksler, V. I. Coherent principle of acceleration of charged particles. In *CERN Symposium on High Energy Accelerators and the Physics of Mesons* (CERN, 1956).

[10] Tajima, T. & Dawson, J. M. Laser electron accelerator. *Phys. Rev. Lett.* **43**, 267–270 (1979).

[11] Bazylev, V. A. & Tulupov, A. V. Acceleration of electrons by the interaction of a bunched electron beam with a metal surface. *Phys. Lett. A* **158**, 135–138 (1991).

[12] Blumenfeld, I. *et al.* Energy doubling of 42 GeV electrons in a metre scale plasma wakefield accelerator. *Nature* **445**, 741–744 (2007).

[13] Vafaei-Najafabadi, N. *et al.* Limitation on the accelerating gradient of a wakefield excited by an ultrarelativistic electron beam in rubidium plasma. *Phys. Rev. Spec. Top. - Accel. Beams* **19**, 1–15 (2016).

[14] Gordon, D. *et al.* Observation of Electron Energies Beyond the Linear Dephasing Limit from a Laser-Excited Relativistic Plasma Wave. *Phys. Rev. Lett.* **80**, 2133–2136 (1998).

[15] Strickland, D. & Mourou, G. Compression of amplified chirped optical pulses. *Opt. Commun.* **56**, 219–221 (1985).

[16] Leemans, W. & Esarey, E. Laser-driven plasma-wave electron accelerators. *Phys. Today* (2009).

[17] Adli, E. Plasma wakefield linear colliders—opportunities and challenges. *Philosophical Transactions of the Royal Society A* **377**, 20180419 (2019).

[18] Herr, W. & Muratori, B. Concept of luminosity. *CERN report* (2006).

[19] Rechatin, C. *et al.* Controlling the phase-space volume of injected electrons in a laser-plasma accelerator. *Phys. Rev. Lett.* **102**, 164801 (2009).

[20] Hogan, M. J. *et al.* Plasma wakefield acceleration experiments at FACET. *New Journal of Physics* **12**, 055030 (2010).

[21] Salehi, F. *et al.* Mev electron acceleration at khz with mj laser pulses. *Opt. Lett.* **42**, 215–218 (2017).

[22] Caldwell, A. & Wing, M. Vheep: a very high energy electron–proton collider. *The European Physical Journal C* **76**, 463 (2016).

[23] Litos, M. *et al.* High-efficiency acceleration of an electron beam in a plasma wakefield accelerator. *Nature* **515**, 92–95 (2014).

[24] Gschwendtner, E. *et al.* Awake, the advanced proton driven plasma wakefield acceleration experiment at cern. *Nuclear Instruments and Methods in Physics Research Section A: Accelerators, Spectrometers, Detectors and Associated Equipment* **829**, 76 – 82 (2016).

[25] Muggli, P. *et al.* AWAKE readiness for the study of the seeded self-modulation of a 400 GeV proton bunch. *Plasma Physics and Controlled Fusion* **60**, 014046 (2017).

[26] Gschwendtner, E. *et al.* Proton-driven plasma wakefield acceleration in awake. *Philosophical Transactions of the Royal Society A: Mathematical, Physical and Engineering Sciences* **377**, 20180418 (2019).

[27] Adli, E. *et al.* Acceleration of electrons in the plasma wakefield of a proton bunch. *Nature* **561**, 363–367 (2018).

[28] Caldwell, A., Lotov, K., Pukhov, A. & Simon, F. Proton-driven plasma-wakefield acceleration. *Nature Physics* **5**, 363–367 (2009).

[29] Batsch, F. *et al.* Interferometer-based high-accuracy white light measurement of neutral rubidium density and gradient at awake. *Nuclear Instruments and Methods in Physics Research Section A: Accelerators, Spectrometers, Detectors and Associated Equipment* **909**, 359 – 363 (2018).

[30] Öz, E., Muggli, P. & Batsch, F. A novel laser ionized rb plasma source for plasma wakefield accelerators. In *Proc. 5th International Particle Accelerator Conference (IPAC14), Dresden, Germany* (2014).

[31] Krall, J. & Joyce, G. Transverse equilibrium and stability of the primary beam in the plasma wakefield accelerator. *Physics of Plasmas* **2**, 1326–1331 (1995).

[32] Kumar, N., Pukhov, A. & Lotov, K. Self-Modulation Instability of a Long Proton Bunch in Plasmas. *Phys. Rev. Lett.* **104**, 255003 (2010).

[33] Lotov, K. V. Physics of beam self-modulation in plasma wakefield accelerators. *Physics of Plasmas* **22**, 103110 (2015).

[34] Fedosseev, V. *et al.* Integration of a Terawatt Laser at the CERN SPS Beam for the AWAKE Experiment on Proton-Driven Plasma Wake Acceleration. In *Proc. 7th International Particle Accelerator Conference (IPAC16), Busan, Korea*, CERN-ACC-2016-209, WEPMY020. 4 p (2016).

[35] Turner, M. *First Observation of the Seeded Proton Bunch Self-Modulation in Plasma* (Thesis, 2017).

[36] Turner, M. *et al.* Experimental observation of plasma wakefield growth driven by the seeded self-modulation of a proton bunch. *Phys. Rev. Lett.* **122**, 054801 (2019).

[37] Adli, E. *et al.* Experimental observation of proton bunch modulation in a plasma at varying plasma densities. *Phys. Rev. Lett.* **122**, 054802 (2019).

[38] Rieger, K., Caldwell, A., Reimann, O., Tarkeshian, R. & Muggli, P. Ghz modulation detection using a streak camera: Suitability of streak

cameras in the awake experiment. *Review of Scientific Instruments* **88**, 025110 (2017).

[39] Lotov, K. V., Minakov, V. A. & Sosedkin, A. P. Parameter sensitivity of plasma wakefields driven by self-modulating proton beams. *Physics of Plasmas* **21**, 083107 (2014).

[40] Whittum, D. H., Sharp, W. M., Yu, S. S., Lampe, M. & Joyce, G. Electron-hose instability in the ion-focused regime. *Phys. Rev. Lett.* **67**, 991–994 (1991).

[41] Hüther, M. & Muggli, P. Seeding of the self-modulation in a long proton bunch by charge cancellation with a short electron bunch. *Nuclear Instruments and Methods in Physics Research Section A: Accelerators, Spectrometers, Detectors and Associated Equipment* **909**, 67 – 70 (2018).

[42] Pepitone, K. *et al.* The electron accelerators for the awake experiment at cern - baseline and future developments. *Nuclear Instruments and Methods in Physics Research Section A: Accelerators, Spectrometers, Detectors and Associated Equipment* **909**, 102 – 106 (2018).

[43] Kim, S.-Y. *et al.* Commissioning of the electron injector for the awake experiment. *Nuclear Instruments and Methods in Physics Research Section A: Accelerators, Spectrometers, Detectors and Associated Equipment* **953**, 163194 (2020).

[44] Mete, O. *et al.* Modeling of an electron injector for the awake project. In *Proc. 6th International Particle Accelerator Conference (IPAC15), Richmond, VA, USA* (2015).

[45] Mete Apsimon, O., Doebert, S., Welsch, C. & Xia, G. Review of Emittance Diagnostics for Space Charge Dominated Beams for AWAKE electron Injector. In *Proc. 7th International Particle Accelerator Conference (IPAC16), Busan, Korea* (2016).

[46] Keeble, F. *et al.* The AWAKE Electron Spectrometer. In *Proc. 9th International Particle Accelerator Conference (IPAC18), Vancouver, BC, Canada*, 4947–4950 (2018).

[47] Olsen, V. K. B., Adli, E. & Muggli, P. Emittance preservation of an electron beam in a loaded quasilinear plasma wakefield. *Phys. Rev. Accel. Beams* **21**, 011301 (2018).

[48] Pepitone, K., Doebert, S. & Burt et al, G. The electron accelerator for the AWAKE experiment at CERN. *Nucl. Instruments Methods Phys. Res. Sect. A Accel. Spectrometers, Detect. Assoc. Equip.* **829**, 73–75 (2016).

[49] Adli, E. Towards Awake Applications: Electron Beam Acceleration in a Proton Driven Plasma Wake. In *Proc. 7th International Particle Accelerator Conference (IPAC16), Busan, Korea* (2016).

[50] Kim, S.-Y., Chung, M., Dayyani, M. & Doebert, S. Study of the electron beam transfer line for the awake run ii experiment at cern. In *29th International Linear Accelerator Conference, Beijing, China* (2018).

[51] Muggli, P., Amorim, L., Karsch, N., Stefan and & Vieira, J. Injection of a LWFA Electron Bunch in a PWFA Driven bya Self-modulated-proton-bunch. In *Proc. 5th International Particle Accelerator Conference (IPAC14), Dresden, Germany* (2014).

[52] Curcio, A. *et al.* Trace - space reconstruction of low-emittance electron beams through betatron radiation in laser-plasma accelerators. *Phys. Rev. Accel. Beams* **20**, 012801 (2017).

[53] Serafini, L. & Rosenzweig, J. B. Envelope analysis of intense relativistic quasilaminar beams in rf photoinjectors: A theory of emittance compensation. *Phys. Rev. E* **55**, 7565–7590 (1997).

[54] Zhang, M. Emittance Formula for Slits and Pepper-pot Measurement. Tech. Rep., Fermi National Accelerator Laboratory (1996).

[55] Apsimon, O., Williamson, B. & Xia, G. A numerical approach to designing a versatile pepper-pot mask for emittance measurement. *Nuclear Instruments and Methods in Physics Research Section A: Accelerators, Spectrometers, Detectors and Associated Equipment* **943**, 162485 (2019).

[56] Lindstrøm, C. A. *et al.* Emittance preservation in an aberration-free active plasma lens. *Phys. Rev. Lett.* **121**, 194801 (2018).

[57] Wu, H.-C., Tajima, T., Habs, D., Chao, A. W. & Meyer-ter Vehn, J. Collective deceleration: Toward a compact beam dump. *Phys. Rev. ST Accel. Beams* **13**, 101303 (2010).

[58] Hanahoe, K. *et al.* Simulation study of a passive plasma beam dump using varying plasma density. *Phys. Plasmas* **24**, 1–13 (2017).

[59] Jakobsson, O. *et al.* Tailored plasma-density profiles for enhanced energy extraction in passive plasma beam dumps. *Plasma Physics and Controlled Fusion* **61**, 124002 (2019).

[60] Dann, S. J. D. *et al.* Laser wakefield acceleration with active feedback at 5 hz. *Phys. Rev. Accel. Beams* **22**, 041303 (2019).

[61] Wolski, A. *Beam dynamics in high energy particle accelerators* (London, Imperial College Press, 2014).

[62] Migliorati, M., Bacci, A. & Benedetti et al, C. Intrinsic normalized emittance growth in laser-driven electron accelerators. *Phys. Rev. Spec. Top. - Accel. Beams* **16**, 1–5 (2013).

[63] Chao, A. W. *Physics of collective beam instabilities in high-energy accelerators* (New York, USA: Wiley (1993), 1993).

[64] Grant, I. S. & Phillips, W. R. *Electromagnetism* (London, New York, Wiley, 1990), 2nd edn.

[65] Wiedemann, H. *Particle accelerator physics* (Springer International Publishing, 2015), 3rd edn.

[66] Panofsky, W. K. H. & Wenzel, W. A. Some considerations concerning the transverse deflection of charged particles in radio-frequency fields. *Rev. Sci. Instrum.* **27**, 967 (1956).

[67] Wilson, P. B. & Griffin, J. . E. High energy electron linacs: application to storage ring RF systems and linear colliders. *AIP Conf. Proc. / SLAC-PUB-2884* **87**, 450–555 (1982).

[68] Panofsky, W. K. H. & Neal, R. Electrons accelerated in the 10-to 20-GeV range. *Science (80-.).* **152** (1966).

[69] Balakin, V., Novokhatsky, A. & Smirnov, V. VLEPP: Transverse Beam Dynamics. *Proc. 12th Int. Conf. Part. Accel.* (1983).

[70] Boyd, T. J. M. & Sanderson, J. J. *The Physics of Plasmas* (Cambridge University Press, 2003).

[71] Malka, V. CERN Accelerator School: Plasma Wake Acceleration. *CERN Yellow Reports* (2014).

[72] Pukhov, A. Particle-in-Cell Codes for plasma-based particle acceleration. *Cern Yellow Reports* **1**, 181–206 (2016).

[73] Mori, W. B. & Katsouleas, T. Wavebreaking of longitudinal plasma oscillations. *Phys. Scr.* **3**, 696–133 (1990).

[74] Esarey, E., Schroeder, C. B. & Leemans, W. P. Physics of laser-driven plasma-based electron accelerators. *Rev. Mod. Phys.* **81**, 1229–1285 (2009).

[75] Sprangle, P., Tang, C. M. & Esarey, E. Relativistic self-focusing of short-pulse radiation beams in plasmas. *IEEE Trans. Plasma Sci.* **15**, 145–153 (1987).

[76] Lu, W. *et al.* Generating multi-gev electron bunches using single stage laser wakefield acceleration in a 3d nonlinear regime. *Phys. Rev. ST Accel. Beams* **10**, 061301 (2007).

[77] Couperus, J. *et al.* Tomographic characterisation of gas-jet targets for laser wakefield acceleration. *Nuclear Instruments and Methods in Physics Research Section A: Accelerators, Spectrometers, Detectors and Associated Equipment* **830**, 504 – 509 (2016).

[78] Durfee III, C. & Milchberg, H. Light pipe for high intensity laser pulses. *Physical review letters* **71**, 2409 (1993).

[79] Ehrlich, Y. *et al.* Guiding of high intensity laser pulses in straight and curved plasma channel experiments. *Physical review letters* **77**, 4186 (1996).

[80] Butler, A., Spence, D. J. & Hooker, S. M. Guiding of high-intensity laser pulses with a hydrogen-filled capillary discharge waveguide. *Phys. Rev. Lett.* **89**, 185003 (2002).

[81] Shalloo, R. *et al.* Low-density hydrodynamic optical-field-ionized plasma channels generated with an axicon lens. *Physical Review Accelerators and Beams* **22**, 041302 (2019).

[82] Hooker, S. M. Developments in laser-driven plasma accelerators. *Nat. Photonics* **7**, 775–782 (2013).

[83] Rosenbluth, M. N. & Liu, C. S. Excitation of plasma waves by two laser beams. *Phys. Rev. Lett.* **29**, 701–705 (1972).

[84] Clayton, C. E., Joshi, C., Darrow, C. & Umstadter, D. Relativistic plasma-wave excitation by collinear optical mixing. *Phys. Rev. Lett.* **54**, 2343–2346 (1985).

[85] Clayton, C. E. *et al.* Ultrahigh-Gradient Acceleration of Injected Electrons by Laser- Excited Relativistic Electron-Plasma Waves. *Phys. Rev. Lett.* **70**, 37–40 (1993).

[86] Andreev, N. E. Resonant excitation of wakefields by a laser pulse in a plasma. *JETP Lett.* **55**, 571 (1992).

[87] Modena, A. *et al.* Electron acceleration from the breaking of relativistic plasma waves. *Nature* **377**, 606–608 (1995).

[88] Nakajima, K. *et al.* Observation of Ultrahigh Gradient Electron Acceleration by a Self-Modulated Intense Short Laser Pulse. *Phys. Rev. Lett.* **74**, 4428–4431 (1995).

[89] Wagner, R., Chen, S.-Y., Maksimchuk, A. & Umstadter, D. Electron Acceleration by a Laser Wakefield in a Relativistically Self-Guided Channel. *Phys. Rev. Lett.* **78**, 3125–3128 (1997).

[90] Moore, C. *et al.* Electron Trapping in Self-Modulated Laser Wakefields by Raman Backscatter. *Phys. Rev. Lett.* **79**, 3909–3912 (1997).

[91] Bharadwaj, V., Bane, K., Clendenin, J., Emma, P. & Sheppard, J. Linac Design for the LCLS Project At SLAC. *Slac Pub 7555* (1997).

[92] Pukhov, A. & Meyer-ter Vehn, J. Laser wake field acceleration: The highly non-linear broken-wave regime. *Appl. Phys. B Lasers Opt.* **74**, 355–361 (2002).

[93] Katsouleas, T. C., Su, J., Wilks, S., Dawson, J. & Chen, P. Beam loading in plasma accelerators. *Part. Accel.* **22**, 81–99 (1987).

[94] Arber, T. D. *et al.* Contemporary particle-in-cell approach to laser-plasma modelling. *Plasma Physics and Controlled Fusion* **57**, 113001 (2015).

[95] Mangles, S. P. D., Murphy, C. D. & Najmudin et al, Z. Monoenergetic beams of relativistic electrons from intense laser-plasma interactions. *Nature* **431**, 535–538 (2004).

[96] Faure, J. *et al.* A laser-plasma accelerator producing monoenergetic electron beams. *Nature* **431**, 541–544 (2004).

[97] Geddes, C. G. R. *et al.* High-quality electron beams from a laser wakefield accelerator using plasma-channel guiding. *Nature* **431**, 538–541 (2004).

[98] Mangles, S. P. D. *et al.* Self-injection threshold in self-guided laser wakefield accelerators. *Phys. Rev. Spec. Top. - Accel. Beams* **15** (2012).

[99] Kneip, S. *et al.* Near-GeV acceleration of electrons by a nonlinear plasma wave driven by a self-guided laser pulse. *Phys. Rev. Lett.* **103** (2009).

[100] Wang, X., Zgadzaj, R. & Fazel et al, N. Quasi-monoenergetic laser-plasma acceleration of electrons to 2 GeV. *Nat. Commun.* **4**, 1988 (2013).

[101] Shiner, D., Gilligan, J. M., Cook, B. M. & Lichten, W. H2, D2, and HD ionization potentials by accurate calibration of several iodine lines. *Phys. Rev. A* **47**, 4042–4045 (1993).

[102] Chen, M., Sheng, Z. M., Ma, Y. Y. & Zhang, J. Electron injection and trapping in a laser wakefield by field ionization to high-charge states of gases. *J. Appl. Phys.* **99** (2006).

[103] Chen, M. *et al.* Theory of ionization-induced trapping in laser-plasma accelerators Implementation of moiré-schlieren deflectometry on a small scale fast capillary plasma discharge Theory of ionization-induced trap-

ping in laser-plasma accelerators. *Phys. Plasmas J. Appl. Phys. J. Chem. Phys. Plasmas J. Homepage* **19**, 33101–174201 (2012).

[104] McGuffey, C. *et al.* Ionization induced trapping in a laser wakefield accelerator. *Phys. Rev. Lett.* **104** (2010).

[105] Thaury, C., Guillaume, E. & Lifschitz et al, A. Shock assisted ionization injection in laser-plasma accelerators. *Sci. Rep.* **5**, 16310 (2015).

[106] Li, F. *et al.* Low-energy-spread laser wakefield acceleration using ionization injection with a tightly focused laser in a mismatched plasma channel. *Plasma Phys. Control. Fusion* **58**, 034004 (2016).

[107] Zeng, M., Chen, M., Sheng, Z.-M., Mori, W. B. & Zhang, J. Self-truncated ionization injection and consequent monoenergetic electron bunches in laser wakefield acceleration. *Physics of Plasmas* **21**, 030701 (2014).

[108] Mirzaie, M. *et al.* Demonstration of self-truncated ionization injection for gev electron beams. *Scientific Reports* **5**, 14659 (2015).

[109] Umstadter, D., Kim, J. & Dodd, E. Laser Injection of Ultrashort Electron Pulses into Wakefield Plasma Waves. *Phys. Rev. Lett.* **76**, 2073–2076 (1996).

[110] Esarey, E., Hubbard, R., Leemans, W., Ting, A. & Sprangle, P. Electron Injection into Plasma Wakefields by Colliding Laser Pulses. *Phys. Rev. Lett.* **79**, 2682–2685 (1997).

[111] Schroeder, C. B., Lee, P. B., Wurtele, J. S., Esarey, E. & Leemans, W. P. Generation of ultrashort electron bunches by colliding laser pulses. *Phys. Rev. E. Stat. Phys. Plasmas. Fluids. Relat. Interdiscip. Topics* **59**, 6037–47 (1999).

[112] Kotaki, H., Masuda, S., Kando, M., Koga, J. K. & Nakajima, K. Head-on injection of a high quality electron beam by the interaction of two laser pulses. *Phys. Plasmas* **11**, 4539 (2004).

[113] Faure, J., Rechatin, C. & Norlin et al, A. Controlled injection and acceleration of electrons in plasma wakefields by colliding laser pulses. *Nature* **444**, 737–739 (2006).

[114] Hidding, B. *et al.* Ultracold electron bunch generation via plasma photocathode emission and acceleration in a beam-driven plasma blowout. *Phys. Rev. Lett.* **108**, 035001 (2012).

[115] Deng, A. *et al.* Generation and acceleration of electron bunches from a plasma photocathode. *Nature Physics* **15**, 1156–1160 (2019).

[116] Bulanov, S., Naumova, N., Pegoraro, F. & Sakai, J. Particle injection into the wave acceleration phase due to nonlinear wake wave breaking. *Phys. Rev. E* **58**, R5257–R5260 (1998).

[117] Geddes, C. G. R. *et al.* Plasma-density-gradient injection of low absolute-momentum-spread electron bunches. *Phys. Rev. Lett.* **100** (2008).

[118] Schmid, K., Buck, A. & Sears et al, C. M. S. Density-transition based electron injector for laser driven wakefield accelerators. *Phys. Rev. Spec. Top. - Accel. Beams* **13** (2010).

[119] Buck, A., Wenz, J. & Xu et al, J. Shock-front injector for high-quality laser-plasma acceleration. *Phys. Rev. Lett.* **110**, 185006 (2013).

[120] Downer, M. C., Zgadzaj, R., Debus, A., Schramm, U. & Kaluza, M. C. Diagnostics for plasma-based electron accelerators. *Rev. Mod. Phys.* **90**, 035002 (2018).

[121] Couperus, J. P. *et al.* Demonstration of a beam loaded nanocoulomb-class laser wakefield accelerator. *Nature Communications* **8**, 487 (2017).

[122] Gonsalves, A. J. *et al.* Petawatt laser guiding and electron beam acceleration to 8 gev in a laser-heated capillary discharge waveguide. *Phys. Rev. Lett.* **122**, 084801 (2019).

[123] Plateau, G. R. *et al.* Low-emittance electron bunches from a laser-plasma accelerator measured using single-shot x-ray spectroscopy. *Phys. Rev. Lett.* **109**, 064802 (2012).

[124] Lundh, O. *et al.* Few femtosecond, few kiloampere electron bunch produced by a laser–plasma accelerator. *Nature Physics* **7**, 219–222 (2011).

[125] Rosenzweig, J. B. *et al.* Experimental observation of plasma wake-field acceleration. *Phys. Rev. Lett.* **61**, 98–101 (1988).

[126] Seeman, J. T. Collective Electron Driven LINAC for High Energy Physics. *IEEE Trans. Nucl. Sci.* **NS-30**, 3180–3182 (1983).

[127] Bane, K., Chen, P. & Wilson, P. B. On Collinear Wakfield Acceleration. *IEEE Trans. Nucl. Sci.* **NS-32**, 3524–3526 (1985).

[128] Muggli, P. & Hogan, M. J. Review of high-energy plasma wakefield experiments. *Comptes Rendus Physique* **10**, 116–129 (2009).

[129] Lu, W., Huang, C., Zhou, M., Mori, W. B. & Katsouleas, T. Nonlinear theory for relativistic plasma wakefields in the blowout regime. *Phys. Rev. Lett.* **96** (2006).

[130] Rosenzweig, J. B. *et al.* Experimental measurement of nonlinear plasma wake fields. *Phys. Rev. A* **39**, 1586–1589 (1989).

[131] Rosenzweig, J. B., Breizman, B., Katsouleas, T. & Su, J. J. Acceleration and focusing of electrons in two-dimensional nonlinear plasma wake fields. *Phys. Rev. A* **44** (1991).

[132] Barov, N. & Rosenzweig, J. B. Propagation of short electron pulses in underdense plasmas. *Phys. Rev. E* **49**, 4407–4416 (1994).

[133] N. Barov, M. E. Conde, W. Gai, and J. B. Rosenzweig. Propagation of Short Electron Pulses in a Plasma Channel. *Phys. Rev. Lett.* **80** (1998).

[134] Assmann, R. *et al.* Proposal for a one GeV plasma wakefield acceleration experiment at SLAC. *Nucl. Instruments Methods Phys. Res. A* **410**, 396–406 (1998).

[135] Hogan, M. J. *et al.* E-157: A 1.4-m-long plasma wake field acceleration experiment using a 30 GeV electron beam from the Stanford Linear Accelerator Center Linac. *Cit. Phys. Plasmas* **7** (2000).

[136] Barnes, C. D. *et al.* Improvements for the third generation plasma wakefield experiment e-164 at slac. In *Proceedings of the 2003 Particle Accelerator Conference*, vol. 3, 1530–1532 vol.3 (2003).

[137] Hogan, M. J. *et al.* Multi-GeV energy gain in a plasma-wakefield accelerator. *Phys. Rev. Lett.* **95** (2005).

[138] Corde, S. *et al.* Multi-gigaelectronvolt acceleration of positrons in a self-loaded plasma wakefield. *Nature* **524**, 442–445 (2015).

[139] Gessner, S. *et al.* Demonstration of a positron beam-driven hollow channel plasma wakefield accelerator. *Nat. Commun.* **7**, 11785 (2016).

[140] Kostyukov, I., Pukhov, A. & Kiselev, S. Phenomenological theory of laser-plasma interaction in "bubble" regime. *Physics of Plasmas* **11**, 5256–5264 (2004).

[141] Kostyukov, I., Kiselev, S. & Pukhov, A. X-ray generation in an ion channel. *Physics of Plasmas* **10**, 4818–4828 (2003).

[142] Swanekamp, S. B., Holloway, J. P., Kammash, T. & Gilgenbach, R. M. The theory and simulation of relativistic electron beam transport in the ion-focused regime. *Physics of Fluids B: Plasma Physics* **4**, 1332–1348 (1992).

[143] Esarey, E., Shadwick, B., Catravas, P. & Leemans, W. Synchrotron radiation from electron beams in plasma-focusing channels. *Physical Review E* **65**, 056505 (2002).

[144] Jackson, J. D. *Classical electrodynamics* (John Wiley & Sons, 2007).

[145] Corde, S. *et al.* Femtosecond x rays from laser-plasma accelerators. *Reviews of Modern Physics* **85**, 1 (2013).

[146] Di Piazza, A., Müller, C., Hatsagortsyan, K. & Keitel, C. H. Extremely high-intensity laser interactions with fundamental quantum systems. *Reviews of Modern Physics* **84**, 1177 (2012).

[147] Cole, J. M. *et al.* Experimental evidence of radiation reaction in the collision of a high-intensity laser pulse with a laser-wakefield accelerated electron beam. *Phys. Rev. X* **8**, 011020 (2018).

[148] Mckenna, P. & Bingham, R. *Laser-Plasma Interactions and Applications* (Springer, 2013).

[149] Bertrand, P. *et al.* A nonperiodic euler–vlasov code for the numerical simulation of laser–plasma beat wave acceleration and raman scattering. *Physics of Fluids B: Plasma Physics* **2**, 1028–1037 (1990).

[150] Courant, R., Friedrichs, K. & Lewy, H. On the partial difference equations of mathematical physics. *IBM journal of Research and Development* **11**, 215–234 (1967).

[151] Godfrey, B. B. Numerical cherenkov instabilities in electromagnetic particle codes. *Journal of Computational Physics* **15**, 504 – 521 (1974).

[152] Pukhov, A. Three-dimensional electromagnetic relativistic particle-in-cell code vlpl (virtual laser plasma lab). *Journal of Plasma Physics* **61**, 425–433 (1999).

[153] Williamson, B., Xia, G., Döbert, S., Karsch, S. & Muggli, P. Simulation study of an lwfa-based electron injector for awake run 2. *Nuclear Instruments and Methods in Physics Research Section A: Accelerators, Spectrometers, Detectors and Associated Equipment* **909**, 126 – 129 (2018).

[154] Swanson, K. K. *et al.* Control of tunable, monoenergetic laser-plasma-accelerated electron beams using a shock-induced density downramp injector. *Phys. Rev. Accel. Beams* **20**, 051301 (2017).

[155] Tsai, H.-E. *et al.* Control of quasi-monoenergetic electron beams from laser-plasma accelerators with adjustable shock density profile. *Physics of Plasmas* **25**, 043107 (2018).

[156] Sears, C. M. S. *et al.* Emittance and divergence of laser wakefield accelerated electrons. *Phys. Rev. ST Accel. Beams* **13**, 092803 (2010).

[157] Floettmann, K. ASTRA: a space charge tracking algorithm, Version 3.2, DESY, available for download from http://www.desy.de/∼mpyflo/ (accessed 01/02/2020).

[158] Maier, A. R. *et al.* Demonstration scheme for a laser-plasma-driven free-electron laser. *Phys. Rev. X* **2**, 031019 (2012).

[159] Saldin, E., Schneidmiller, E. & Yurkov, M. On the coherent radiation of an electron bunch moving in an arc of a circle. *Nuclear Instruments and Methods in Physics Research Section A: Accelerators, Spectrometers, Detectors and Associated Equipment* **398**, 373 – 394 (1997).

[160] Lim, J. K., Frigola, P. & Travish et al, G. Adjustable, short focal length permanent-magnet quadrupole based electron beam final focus system. *Phys. Rev. Spec. Top. - Accel. Beams* **8**, 1–17 (2005).

[161] Borland, M. Elegant: A flexible sdds-compliant code for accelerator simulation. Tech. Rep., Argonne National Lab., IL (US) (2000).

190

[162] Williamson, B. *et al.* Betatron radiation diagnostics for awake run 2. *Nuclear Instruments and Methods in Physics Research Section A: Accelerators, Spectrometers, Detectors and Associated Equipment* **971**, 164076 (2020).

[163] Thomas, C., Delerue, N. & Bartolini, R. Single shot 3 gev electron transverse emittance with a pepper-pot. *Nuclear Instruments and Methods in Physics Research Section A: Accelerators, Spectrometers, Detectors and Associated Equipment* **729**, 554–556 (2013).

[164] Schnell, M., Sävert, A., Landgraf, B. & et al. Deducing the electron-beam diameter in a laser-plasma accelerator using x-ray betatron radiation. *Phys. Rev. Lett.* **108**, 075001(5) (2012).

[165] Köhler, A. *et al.* Single-shot betatron source size measurement from a laser-wakefield accelerator. *Nuclear Instruments and Methods in Physics Research Section A: Accelerators, Spectrometers, Detectors and Associated Equipment* **829**, 265 – 269 (2016).

[166] Esarey, E., Sprangle, P., Krall, J. & Ting, A. Overview of plasma-based accelerator concepts. *IEEE Transactions on Plasma Science* **24**, 252–288 (1996).

[167] Phuoc, K. T. *et al.* Imaging Electron Trajectories in a Laser-Wakefield Cavity Using Betatron X-Ray Radiation. *Phys. Rev. Lett.* **97**, 225002(4) (2006).

[168] Albert, F. *et al.* Angular dependence of betatron X-ray spectra from a laser-wakefield accelerator. *Phys. Rev. Lett.* **111**, 235004(5) (2013).

[169] Wang, S., Clayton, C. E., Blue, B. E. & et al. X-Ray Emission from Betatron Motion in a Plasma Wiggler. *Phys. Rev. Lett.* **88**, 135004(4) (2002).

[170] Mehrling, T. J., Fonseca, R. A., Martinez de la Ossa, A. & Vieira, J. Mitigation of the hose instability in plasma-wakefield accelerators. *Phys. Rev. Lett.* **118**, 174801 (2017).

[171] Mehrling, T. J., Benedetti, C., Schroeder, C. B., Esarey, E. & Leemans, W. P. Suppression of beam hosing in plasma accelerators with ion motion. *Phys. Rev. Lett.* **121**, 264802 (2018).

[172] San Miguel Claveria, P. *et al.* Betatron radiation and emittance growth in plasma wakefield accelerators. *Philosophical Transactions of the Royal Society A: Mathematical, Physical and Engineering Sciences* **377**, 20180173 (2019).

[173] Šmíd, M. *et al.* Highly efficient angularly resolving x-ray spectrometer optimized for absorption measurements with collimated sources. *Rev. Sci. Instrum.* **88**, 063102(8) (2017).

[174] Michel, P., Schroeder, C., Shadwick, B., Esarey, E. & Leemans, W. Radiative damping and electron beam dynamics in plasma-based accelerators. *Physical Review E* **74**, 026501 (2006).

[175] Deng, A. *et al.* Electron beam dynamics and self-cooling up to pev level due to betatron radiation in plasma-based accelerators. *Physical Review Special Topics-Accelerators and Beams* **15**, 081303 (2012).

[176] Kostyukov, I. Y., Nerush, E. N. & Litvak, A. G. Radiative damping in plasma-based accelerators. *Phys. Rev. ST Accel. Beams* **15**, 111001 (2012).

[177] Jauregui, C., Limpert, J. & Tünnermann, A. High-power fibre lasers. *Nat. Photonics* **7**, 861–867 (2013).

[178] Hooker, S. M. *et al.* Multi-pulse laser wakefield acceleration: a new route to efficient, high-repetition-rate plasma accelerators and high flux

radiation sources. *Journal of Physics B: Atomic, Molecular and Optical Physics* **47**, 234003 (2014).